DEPARTAMENTO DE MATEMÁTICAS
FACULTAD DE CIENCIAS
UNIVERSIDAD AUTÓNOMA DE MADRID

INSTITUTO DE
CIENCIAS MATEMÁTICAS
CSIC - UAM - UC3M - UCM

NONAUTONOMOUS DYNAMICAL SYSTEMS: FROM THEORY TO APPLICATIONS

Francisco Balibrea Iniesta

Memoria de Tesis Doctoral dirigida por

Ana María Mancho Sánchez (CSIC)
Stephen Wiggins (University of Bristol)

Madrid, 2018

This Ph.D. thesis has been partially supported by MINECO under grant MTM2014-56392-R, MINECO: ICMAT Severo Ochoa project SEV-2011-0087 and ONR grant N00014-17-1-3003. The research stays along this Ph.D. programme have been financed by MINECO programme: Subprograma Estatal de Movilidad (announcements in 2015, 2016 and 2017), ONR Grant No. N00014-01-1-0769 and ESSEM COST Action ES1402. I am very greteful to the computing team at ICMAT, specially to Alfredo Caso, for his key contribution on the good performance of Lovelace cluster, where many of the simulations conforming the present work were done.

Agradecimientos

Concluída ya prácticamente esta etapa de tesis doctoral, se impone hacer un balance justo del recorrido realizado en estos últimos cuatro años. Son muchas las personas y experiencias que directa o indirectamente han influído en mi desarrollo personal de la tesis, aunque no es menos cierto que esta etapa ha coincidido con los mejores años de mi vida, en los que mi personalidad ha evoluciado de forma determinante y ha moldeado en el tiempo a una persona de la que me siento orgulloso. Es por ello que no puedo obviar la estrecha interrelación entre el plano laboral y el personal. Al igual que ocurre a la mayoría, este mi primer trabajo ha marcado una diferencia notable entre mi vida anterior y la actual, en la que uno aprende a llevar las riendas de su propia vida con todos los riesgos y dificultades que conlleva. Mi impresión no puede ser más positiva y gratificante.

En función de mi experiencia personal, y fiel a mi tradición de dar sentido político a todos los actos que acometemos en nuestras vidas cotidianas, estoy cada vez más convencido de la necesidad de garantizar el trabajo al conjunto de la sociedad. A su vez el cumplimiento de los Derechos Humanos se torna inevitable para procurar una vida digna, para dotar de las herramientas básicas para que las personas desarrollen una vida plena en el sentido que deseen, tal y como yo sigo disfrutando. Afortunado pues en la vida, mi compromiso político es cada vez mayor e intuyo que ha llegado a un punto de no retorno. Todo lo aprendido durante estos últimos años, incluída una fuerte conciencia colectiva, ha configurado mi forma de ser, siempre leal a los valores de aquellos que me precedieron.

Asímismo este humilde trabajo pretende ser un homenaje a mi madre y a mi padre, a Miguela y a Paco, las dos personas que siempre me prestaron todo su apoyo incondicionalmente. Todo para que esta persona que les habla haya podido desarrollar una vida personal y profesional satisfactorias. Más allá de sus facetas como matemáticos, siempre sobresaldrá la creencia insistente en su hijo, en su capacidad para crecer a pesar de las dificultades, además de la trasmisión de valores muy humanos y nobles que perduran hasta el día de hoy. Sin ellos me siento incapaz de entender mi presente, menos aún de entender mis éxitos pasados. Ellos han sido expectadores de excepción en el desarrollo de esta tesis, siempre apoyándome cada vez que surgían complicaciones, atentos en cada ocasión que viajaba al extranjero. Siempre orgullosos de mi labor, de mi compromiso. A más que nadie esta tesis va dedicada a mis queridos padres.

Sin ánimo de comparar a nadie, no es menos cierto que mis directores Ana y Steve han influído en el correcto desarrollo de la tesis, al igual que el resto

de integrantes de nuestro grupo: Carlos, Víctor, Jezabel y Carolina. Ambos Ana y Steve han destacado por su profesionalidad, su dedicación y su capacidad para identificar problemas de gran interés científico. En especial agradezco a Steve su compromiso de dirigir mi tesis a pesar de la distancia, de las muchas dificultades que tuvo que sobrellevar. No es menos cierto que las estancias en Bristol (hasta cinco ocasiones) han significado un avance determinante en la tesis, un empuje de trabajo y motivación muy necesario. Y como consecuencia, Bristol se quedará siempre en mi recuerdo como el sitio entrañable al que siempre querré volver.

Y entre mis recuerdos también quedará para siempre Carlos, con quien tuve la inmensa fortuna de compartir tres largas e intensas estancias en Bristol. Nuestro apoyo mutuo y trabajo en equipo, con una excelente relación personal mediante, hizo que Carlos se convirtiera en el mejor compañero de tesis doctoral. Ya fuera en Bristol o en nuestro despacho en el ICMAT, la creatividad borboteaba al igual que nuestros cafés mañaneros. Quien también quedará en el recuerdo es nuestro querido y hermoso Imanol, compañero mío del Chaminade y anfitrión inesperado en nuestros viajes a Bristol. Nuestras quedadas fueron memorables e hicieron más divertidas las semanas en el extranjero.

De vuelta a Madrid, no dejo pasar la oportunidad de destacar a Miguel, compañero de despacho y de lucha. Su manera de entender la realidad influyó inevitablemente en mi pensamiento, a través de nuestros innumerables debates. Juntos compartimos la ilusión durante la etapa más esperanzadora de la política española, desde el intensísimo año 2014 y las manifestaciones, pasando por el frustado intento por "asaltar los cielos" hasta el día de hoy. La creencia en la colectividad y nuestro espíritu integrador nos llevó a organizar, junto con muchos otros colegas matemáticos y físicos del CFTMAT, el ya desaparecido café autogestionado bajo estándares sostenibles. Reflejo de lo que aspiramos en nuestro centro de trabajo, al margen de cuestiones formales o científicas.

Por último no quiero olvidarme de otros amigos que influyeron positivamente en mi carrera. Mucho antes de descubrir el ICMAT tuve la oportunidad de iniciarme en la investigación junto con el grupo liderado por Víctor Pérez, en la Escuela de Industriales de la Universidad de Castilla-La Mancha. Allí coincidí con David, ingeniero transformado en matemático, y primer compañero en mi aventura científica. Él me inspiró las actitudes básicas del doctorando, su buen hacer cotidiano, sin prisa pero sin pausa. Y por último quiero mencionar a Jose Ginés, matemático cartagenero y buen campechano (con permiso de nuestro Rey Emérito). Aparte de compartir muchas inquietudes y gran parte de su tiempo en Madrid, siempre me sorprendió su humildad

sincera. La cual demuestra que el ser buen científico no está reñido con la empatía ni con otras nobles virtudes.

A todas las personas que he mencionado, todas muy buenas personas sin excepción, a la vez que amigos y compañeros de trabajo a lo largo de estos años, os quiero trasmitir mi más sincera gratitud.

Esto es sólo el comienzo.

Dos murcianicos perdidos en Inglaterra: Carlos y un servidor desde el puente colgante de Clifton, en la parte alta de Bristol, disfrutando de un paseo mañanero entre días de intensa creatividad matemática y degustación gastronómica. Buenísimos recuerdos de aquella nuestra primera estancia en la que aún éramos unos novicios en la investigación ... y unos jovenzuelos. Noviembre de 2014.

Abstract

The first part of this thesis is a more in-depth study of the notion of chaos in nonautonomous dynamical systems which is a tool for describing transport and mixing in a geophysical set. The formal proof of chaos is approached through nonautonomous maps. The main goal in this part is to provide an extension of the Conley-Moser conditions to the nonautonomous setting. These conditions compose a set of assumptions which guarantee the existence of a chaotic invariant set where chaos is defined as "sensitivity dependence", and which are finally verified in a benchmark example of a sequence of maps referred to as the nonautonomous Hénon map. This example provides a geometrical construction of a chaotic set over a planar region, and is one the few instances found in the literature in which it is proven for an aperiodic system.

Furthermore, in the study of nonautonomous dynamical systems, this thesis focuses on the dynamics generated by stochastic differential equations with a random time dependence. This analysis is performed by extending the method of Lagrangian descriptors to the stochastic framework, a technique which has been applied to deterministic dynamical systems in order to display relevant phase space structures. The application of this technique to several stochastic models reveals a high concordance between the Lagrangian structures displayed by the Lagrangian descriptors and the paths of the particles tracked by such model systems. A discussion is also provided on the notion of hyperbolic stationary orbit in the stochastic setting and its similarities with a hyperbolic stationary point of an autonomous system.

The final part of the thesis deals with Arctic Ocean circulation patterns from a Lagrangian perspective. To this end, the methodology of Lagrangian descriptors is again applied, in this case to the velocity field dataset provided by the Copernicus Marine Environment Monitoring Service. The focus consists of an analysis on the Arctic region in the halocline (top 30 meters depth), over a time period ranging from March 2013 to March 2015. The advantage of the method of Lagrangian descriptors is that it highlights large-scale persistent dynamical structures related to invariant manifolds, which are mathematical objects that determine fluid transport and mixing processes. These geometrical flow structures play a crucial role in the evolution of the freshwater content and also in the evolution of potential contaminants in the Arctic region. In concrete, such structures in the Beaufort Sea are identified, and it is shown how they mediate transport processes according to a clockwise circulating pattern, related to the Beaufort Gyre (BG). Additionally this approach highlights the Transpolar Drift Stream (TDS) as a transport barrier which maintains the salinity gradient between the Canada Basin and the Atlantic waters.

Resumen

La primera parte de la tesis estudia aspectos relativos a la noción de caos en sistemas dinámicos no autónomos. El caos es un concepto matemático útil para explicar los procesos de mezcla en fluidos geofisicos, al igual que los procesos de transporte en este ámbito. La demostración formal de la presencia de caos en este contexto se realiza mediante mapas no autónomos; es decir, mediante sucesiones de funciones. En esta parte el objetivo principal consiste en extender las condiciones de Conley-Moser al ámbito de los mapas no autónomos. Dichas condiciones conforman un conjunto de tres proposiciones que de cumplirse garantizan la existencia de un conjunto invariante caótico, donde el caos se concibe como una "dependencia sensible de las condiciones iniciales". Estas condiciones son verificadas en el mapa de Hénon no autonomo, que constituye una sucesión de funciones muy representativa. Este ejemplo nos proporciona una construcción geométrica de un conjunto invariante caótico en el plano; y además se trata de uno de los pocos ejemplos de sistemas aperiódicos de la literatura para los que formalmente se ha demostrado la existencia de caos.

Continuando con el estudio de los sistemas dinámicos no autónomos, la tesis se centra en la dinámica generada por las ecuaciones diferenciales estocásticas, con una dependencia temporal aleatoria. Este análisis se realiza mediante la extensión del método de los descriptores lagrangianos al marco estocástico. Esta técnica ha sido aplicada a sistemas dinámicos deterministas con el fin de revelar estructuras destacadas del espacio de fases. En su aplicación a varios modelos estocásticos, los descriptores lagrangianos muestran una gran concordancia entre las estructuras lagrangianas y las trayectorias seguidas por las partículas advectadas por dichos modelos. Por otra parte se proporciona una discusión acerca de cómo extender la noción de órbita estacionaria hiperbólica al contexto estocástico y sus similitudes con el concepto de punto hiperbólico en un sistema autónomo.

La parte final de la tesis versa sobre cómo aplicar ideas elaboradas en el campo de los sistemas dinámicos no autónomos y aperiódicos a un contexto de análisis del transporte en el océano Ártico. A tal efecto se vuelve a utilizar la metodología de los descriptores lagrangianos, esta vez aplicados a campos de velocidad proporcionados como conjuntos de datos por el Copernicus Marine Environment Monitoring Service. El interés se centra en el análisis de la haloclina (a 30 metros de profundidad) emplazada en la región ártica, en el período comprendido entre marzo de 2013 y marzo de 2015. El método de los descriptores lagrangianos muestra estructuras dinámicas persistentes a largo plazo que se relacionan con las variedades invariantes, un objeto geométrico que caracteriza los procesos de transporte y mezcla de fluidos. Estas estruc-

turas juegan un papel crucial en la distribución de las masas de agua no salada y en la evolución de los contaminantes potencialmente vertidos en la región ártica. En concreto, tales estructuras son detectadas en el mar de Beaufort y median en los procesos de transporte induciendo una circulación en sentido horario, a su vez relacionada con el giro de Beaufort. Los descriptores lagrangianos también identifican la corriente denominada *Transpolar Drift* como una barrera al transporte que sustenta un gradiente de salinidad entre la cuenca oceánica ártica de Canadá y las aguas del Atlántico.

Contents

Chapter 1

Introduction

Over the last decades, dynamical systems theory has been successfully applied for describing transport and mixing processes in geophysical flows. Several approaches to flow structures in the ocean throughout the 1980s motivated the study of geophysical flows from the viewpoint of dynamical systems through an enhancement of data visualization [Wiggins, 2005]. In this sense, the work by Aref [1984] is a seminal contribution to the use of dynamical systems theory for describing advection problems in fluid mechanics. In particular, Aref's work reports a simple fluid model with an unsteady motion where chaotic advection is a robust event leading to what is currently referred to as the "dynamical systems approach" to transport and mixing problems in fluid mechanics.

Since then, many works have continued this approach, providing deep insights into our understanding of flow phenomena. Monographs by Ottino [1989]; Wiggins [1992] illustrate this tendency from different perspectives. The first one gathers mathematical criteria that formally treats mixing phenomena from a kinematic viewpoint, while the second deals with fluid flows made time dependent by means of small perturbations in the context of *phase space transport*. Both provide a wide mathematical background and tools for facilitating the understanding of fluid flow events present in nature. More recently the work by Samelson & Wiggins [2006] points in this same direction by providing a set of modern methods in the analysis of geophysical flows.

Mathematically the description of transport in fluid mechanics in the purely advective approach is given by the following continuous time system

$$\dot{\mathbf{x}} = f(\mathbf{x}, t), \quad \mathbf{x} \in X \subseteq \mathbb{R}^N, \quad t \in \mathbb{R}, \tag{1.1}$$

or in the discrete time approach by

$$\mathbf{x}_{n+1} = f_n(\mathbf{x}_n), \quad \mathbf{x}_n, \mathbf{x}_{n+1} \in X \subseteq \mathbb{R}^N, \quad n \in \mathbb{Z},$$

where N equals 1, 2 or 3 depending on the dimension of the environment, $X \subseteq \mathbb{R}^N$ is an open subset and the temporal domain $\mathbb{R}$ or $\mathbb{Z}$ comes generally denoted as $\mathbb{T}$.

As pointed out before, one of the most notable features arising in dynamical systems such as those given in (1.1) is chaos, which has been related to mixing processes [Sturman *et al.*, 2006], and indeed constitutes a fundamental part of dynamical systems theory. In particular, geophysical fluid flows are frequently described as "chaotic" when there is evidence of mixing. Although there is no formal definition of chaos (a notion initially introduced by Li & Yorke [1975]) according to the viewpoint adopted, there coexist mainly two distinct tendencies [Hunt & Ott, 2015]: one involves the notion of entropy and the other "sensitive dependence". This last version of chaos is the one followed in this work, and is usually referred to as Devaney chaos due to [Devaney, 1989], although preceding authors such as Poincaré [1914] and Lorenz [1963] noticed sensitivity of orbits to small perturbations before.

In accordance with this choice, the Smale horseshoe map (introduced for instance in [Smale, 1980]) is a particular construction for which the existence of a chaotic invariant set has been proven. It consists of infinite crossings of material strips over a given area in which initial conditions follow distinct and unpredictible evolutions (see [Wiggins, 2003] for further details). Moser [1973] and Wiggins [2003] report necessary conditions for an autonomous map to present a chaotic invariant set, similarly to previous works by Alekseev [1968a,b, 1969]. These conditions are referred to as the Conley-Moser conditions. The analysis conducted in Chapter 2 consists of an adaptation of these conditions for nonautonomous (aperiodic) maps, including the formal statement and proof of the third nonautonomous Conley-Moser condition, as an expansion of previous work by Wiggins [1999]. Moreover, in this chapter the well-known Hénon map is taken as a reference in the construction of a benchmark example of nonautonomous map performing a chaotic behaviour. The interest of these results also lies on the possible translation of the characterization of chaos to the continuous dynamical systems setting by means of the solution mappings introduced in Chapter 3, although this issue is beyond the scope of this thesis.

Dynamical systems theory also contributes to the study of transport in systems such as (1.1) by realizing Poincaré's idea of seeking geometrical structures in the phase space (for fluid applications, the phase space is the physical space, such as the ocean surface), which can be used to schematically organize regions corresponding to qualitatively different types of trajectories. Among these geometrical objects are the stable and unstable manifolds of hyperbolic trajectories. However, not every notion or technique coming from the

classical theory of dynamical systems directly applies to nonautonomous dynamical systems, and more concretely to geophysical fluid flows.

Furthermore, geophysical velocity fields are frequently provided as finite time data sets, which makes a reformulation necessary for asymptotic time concepts as basic as the stability of a stationary fixed point. On the other hand geophysical flows are aperiodically time dependent, and therefore techniques such as the Poincaré map, applicable in periodically time dependent systems, is no longer applicable in this context. Among the mathematical concepts that can be applied in geophysical flows, apart from chaos or the above-mentioned stable and unstable manifolds of hyperbolic trajectories, lobe dynamics linked with Melnikov-type methods for aperiodic dynamical systems (illustrated in [Malhotra & Wiggins, 1998; Rogerson *et al.*, 1999]), for example, provide a wide understanding of the exchange of fluid between different flow regimes from a theoretical viewpoint.

New Lagrangian[1] concepts and techniques were also introduced to address the geometrical approach in the context of geophysical flows. In particular, manifolds have been approximated by computing ridges of fields, such as finite-size Lyapunov exponents (FSLE) [Aurell *et al.*, 1997], successfully applied into oceanic contexts (see for instance [d'Ovidio *et al.*, 2004]), and also finite-time Lyapunov exponents (FTLE) [Nese, 1989; Shadden *et al.*, 2005]. In this latter article, the authors redefine the concept of "Lagrangian coherent structures" (LCS) in terms of FTLEs, an idea inspired by the previous work by Haller [2001]. The notion of LCS refers to the temporal-spatial surfaces located at the boundaries between distinct circulation regimes, and consequently the technique of FTLEs is proven to display a great applicability in the geophysical flows framework.

Another perspective within the geometrical approach that differs from Lyapunov exponents is that provided by distinguished hyperbolic trajectories (DHT), a revision of the notion of fixed point adapted to dynamical systems with a general time dependence. This concept was first introduced in the works by Ide *et al.* [2002]; Ju *et al.* [2003], mainly based on the mathematical ideas exposed in [Malhotra & Wiggins, 1998]. Analogously to stationary points in the autonomous setting, the interest of detecting DHTs for a general time dependent dynamical system resides in their capability to govern the long-term behaviour of nearby trajectories, and also through the computation of their corresponding stable and unstable manifolds as material surfaces (see for instance [Mancho *et al.*, 2003, 2006]). Moreover, this method has also provided valuable insights into oceanic problems [Mancho *et al.*, 2008; Men-

[1]The term Lagrangian serves to label those concepts based on the coordinates of the particles trajectories advected by the corresponding dynamical system.

doza & Mancho, 2010].

In the range of all different Lagrangian techniques applied to a geophysical context, a recent tool that reveals phase space structures of general time dependent dynamical systems is the so-called function M, initially introduced in [Madrid & Mancho, 2009] for redefining DHTs and further developed in [Mendoza & Mancho, 2010, 2012; Mancho *et al.*, 2013]. This function is the basis of the method of Lagrangian descriptors (denoted as LDs) and has been successfully used for describing transport processes in the atmosphere (for instance [de la Cámara *et al.*, 2012, 2013]) and in the ocean [García-Garrido *et al.*, 2015]. More recently, two articles [Lopesino *et al.*, 2015a, 2017] have suggested a new version of the method of LDs applied to discrete time and continuous time dynamical systems, respectively. This is supported by formal proofs that simplify the calculations to obtain the explicit expression of the Lagrangian descriptor function, while at the same time preserving the same features displayed by the original method based on function M.

Chapters 3 and 4 of this thesis address the extension of this tool for the context of stochastic dynamical systems. When modelling real behaviour, as in the case of geophysical flows, dynamical systems are often subject to random influences such as external fluctuations, uncertain parameters, etc. Uncertainty or randomness may have a profound impact on the overall evolution of complex dynamical systems. Stochastic differential equations (SDE) are appropriate models for randomly influenced systems. These chapters explore notions and ideas which are familar in the context of deterministic differential equations and examine whether they are still valid for SDEs. In particular, the notions of hyperbolic trajectory and its stable and unstable manifolds are considered in the context of SDEs. Additionally, a reflexion is made on how such notions would manifest themselves in the context of phase space transport for SDE.

Finally, Chapter 5 addresses an application of Lagrangian descriptors to the study of transport processes in the Arctic Ocean. Many of the discussions addressed in the previous chapters are built on 2D dynamical systems, although the study of transport processes in 3-D flows has also been addressed with this and similar tools [Rempel *et al.*, 2013; Bettencourt *et al.*, 2015; Curbelo *et al.*, 2017]. Nevertheless, many studies of Lagrangian coherent structures in the atmosphere and in the ocean have been performed in a two-dimensional scenario. This is because the Lagrangian motion of the particles stays on 2D surfaces [Branicki & Kirwan, 2010; Curbelo *et al.*, 2017] in an appropriate range of space scales and timescales. This is the perspective adopted in this report, in which transport processes within the Arctic halocline are also studied to explore the implications of currents in salinity anomalies. In

oceanography, the halocline is the horizontal layer of water in the sea at which the vertical salinity gradient undergoes pronounced variations; in the Arctic Ocean, in particular, this layer is located at the sea surface within the upper 150-200 metres [Tomczak & Godfrey, 1994]. This study is not based on a generic model of the Arctic Ocean, but rather on data sets (which include salinity, temperature and velocity fields) produced by realistic simulations which include assimilation of observational data measured by buoys, other *in situ* gadgets and satelite altimeters [Melsom *et al.*, 2017; Xie *et al.*, 2017]. These processed data are integrated into a product called "Arctic Ocean Physics Analysis and Forecast", which is freely available from Copernicus Marine Environment Monitoring Service[2] and forms the basis of the computations required for the implementation of the method of Lagrangian descriptors over the Arctic Ocean.

Arctic currents present different characteristics to those found in the Earth's other oceans, since typical velocities are much slower, and particles may take from months to years to navigate through significant distances. Although transport timescales in the Arctic are thus longer than in other areas, similar challenges exist in the qualitative and quantitative description of fluid transport and mixing issues. For instance, even in apparently simple velocity fields, nearby particles can evolve by following completely different paths. In this sense, the method of LDs, computed for a sufficiently large integration time and applied to these velocity fields, has the ability to display geometrical Lagrangian features that support the interpretation of the paths traced by the water fluid parcels. Finally, the method draws a general circulation pattern of the entire Arctic.

These results are of great interest, since the Arctic Ocean is one of the regions most sensitive to climate change, as manifested by dramatic changes of the Arctic sea ice cover, including the reduction in the extent of the ice and the thinning of the ice layer [Krishfield *et al.*, 2014]. As a result, the reduced ice cover in the Arctic is making this region more attractive to offshore activities such as oil and gas exploration. Consequently, these studies on the fate of water masses are highly significant for characterizing the dispersion of potential coast accidents due to exploitation, and thereby contribute to their remediation.

[2] As stated on its website (*http://www.copernicus.eu/main/overview*), "Copernicus is a European Union Programme aimed at developing European information services based on satellite Earth Observation and *in situ* data".

Chapter 2

Chaos in nonautonomous maps

In this chapter the chaotic dynamics for two-dimensional nonautonomous maps are evaluated through the use of a set of analytical conditions which ensure the existence of *chaotic invariant sets*. Here it is considered the specific example of a nonautonomous version of the well-known Hénon map, for which are given enough conditions to display a hyperbolic chaotic invariant set, in terms of the parameters defining it. All these results are reported in [Balibrea-Iniesta *et al.*, 2015].

Studies of the Hénon map (see [Hénon, 1976]) have played a seminal role in the development of our understanding of chaotic dynamics and strange attractors. The map depends on two parameters, A and B, and has the following form

$$\begin{array}{rccc} H & : & \mathbb{R}^2 & \longrightarrow & \mathbb{R}^2, \\ & & (x,y) & \longmapsto & (A+By-x^2,x), \end{array} \tag{2.1}$$

where it is required $B \neq 0$ in order to endure the existence of the inverse map

$$\begin{array}{rccc} H^{-1} & : & \mathbb{R}^2 & \longrightarrow & \mathbb{R}^2, \\ & & (x,y) & \longmapsto & (y,(x-A+y^2)/B). \end{array} \tag{2.2}$$

The "heart" of chaotic dynamics is exemplified by the so-called "Smale horseshoe map" (see [Smale, 1980] for a general description, with background). The essential feature of the Smale horseshoe map for chaos is that the map contains an invariant Cantor set on which the dynamics are topologically conjugate to a shift map defined on a finite number of symbols (a "chaotic invariant set", sometimes also referred to as a "chaotic saddle"). Devaney & Nitecki [1979] gave sufficient conditions, in terms of the parameters A and B, for the Hénon map to have an invariant Cantor set on which it is

topologically conjugate to a shift map of two symbols. The proof uses a technique due to Conley and Moser (see [Moser, 1973]) that is referred to as the "Conley-Moser conditions" (but for earlier work in a similar spirit see [Alekseev, 1968a,b, 1969]). Holmes [1982] used these conditions to show the existence of a chaotic invariant set in the so-called "bouncing ball map". The Conley-Moser conditions were given a more detailed exposition, along with a slight weakening of the hypotheses, in [Wiggins, 2003]. More recently, the Conley-Moser conditions were used to show the existence of a chaotic invariant set in the Lozi map [Lopesino *et al.*, 2015b].

In this chapter a similar analysis for a nonautonomous version of the Hénon map is carried out. The generalization of the Conley-Moser conditions for nonautonomous systems, i.e. in the discrete time setting with dynamics defined by an infinite sequence of maps, was given in [Wiggins, 1999]. Here the nonautonomous Conley-Moser conditions are extended further by providing an additional condition which is sufficient for the nonautonomous chaotic invariant set to be hyperbolic. Hyperbolicity of nonautonomous invariant sets is discussed in general in [Katok & Hasselblatt, 1995]. Earlier work on chaos in nonautonomous systems is described in [Lerman & Silnikov, 1992; Stoffer, 1988a,b]. Recent interesting work is described in [Lu & Wang, 2010, 2011].

While the development of the "dynamical systems approach to nonautonomous dynamics" is currently a topic of much interest, it is not a topic that is widely known in the applied dynamical systems community (especially the fundamental work that was done in the 1960's). An applied motivation for such work is an understanding of fluid transport from the dynamical systems point of view for aperiodically time dependent flows. Wiggins & Mancho [2014] have given a survey of the history of nonautonomous dynamics as well as its application to fluid transport.

This chapter is outlined as follows. In Section 2.1 the required concepts for "building" chaotic invariant sets are developed for two-dimensional nonautonomous maps. In Section 2.2 the "main theorem" generalizing the Conley-Moser conditions is proved; these provide necessary conditions for two-dimensional nonautonomous maps to have a chaotic invariant set as mentioned before. In the course of the proof of the theorem the nature of chaotic invariant sets, and chaos, for nonautonomous maps is developed. This theorem was first given in [Wiggins, 1999], but in Section 2.2.1 this theory is further developed by providing a more analytical, rather than topological, construction for one of the Conley-Moser conditions that leads to conclude that the nonautonomous chaotic invariant set is hyperbolic. In Section 2.3 a version of the nonautonomous Hénon map is given and the previously sufficient conditions for the map to possess a nonautonomous chaotic invariant set are applied

to this example. Finally the directions for future work along these lines are discussed.

2.1 Preliminary concepts

Here the basic setting and concepts used throughout this chapter are introduced.

Nonautonomous dynamics come defined by a sequence of maps and domains $\{f_n, D_n\}_{n=-\infty}^{+\infty}$ acting as follows

$$f_n : D_n \longrightarrow D_{n+1} \qquad \forall n \in \mathbb{Z} \quad \text{and} \quad f_n^{-1} : D_{n+1} \longrightarrow D_n, \tag{2.3}$$

where D_n will be an appropriately chosen domain in $\mathbb{R}^2$ for every n.

Similar to the Smale horseshoe construction [Wiggins, 2003], on each domain D_n a finite collection of vertical strips $V_i^n \subset D_n$ ($\forall n \in \mathbb{Z}$ and $\forall i \in I = \{1, 2, ..., N\}$) must be constructed in order to map to a finite collection of horizontal strips H_i^{n+1} located in D_{n+1}

$$H_i^{n+1} \subset D_{n+1} \quad \text{with} \quad f_n(V_i^n) = H_i^{n+1} \ , \quad \forall n \in \mathbb{Z} \ , \quad i \in I. \tag{2.4}$$

Associated with these mappings a *transition matrix* as the following is needed

$A \equiv \{A^n\}_{n=-\infty}^{+\infty}$ is a sequence of matrices of dimension $N \times N$ such that

$$A_{ij}^n = \begin{cases} 1 & \text{if } f_n(V_i^n) \cap V_j^{n+1} \neq \emptyset \\ 0 & \text{otherwise} \end{cases} \quad \text{or equivalently}$$

$$A_{ij}^n = \begin{cases} 1 & \text{if } H_i^{n+1} \cap V_j^{n+1} \neq \emptyset \\ 0 & \text{otherwise} \end{cases} \quad \forall i, j \in I. \tag{2.5}$$

However, it is firstly required the precise definition of the domains used onwards, the horizontal and vertical strips in those domains, in order to provide a characterization of the intersection of horizontal and vertical strips in the domain appropriate for the example exposed onwards.

To begin let $D \subset \mathbb{R}^2$ denote a closed and bounded set, and consider two associated subsets of $\mathbb{R}$

$$D_x = \{x \in \mathbb{R} \mid \text{there exists a } y \in \mathbb{R} \text{ with } (x, y) \in D\}$$

$$D_y = \{y \in \mathbb{R} \mid \text{there exists an } x \in \mathbb{R} \text{ with } (x, y) \in D\}. \tag{2.6}$$

Therefore D_x and D_y represent the projections of D onto the x-axis and the y-axis respectively. From this it is easy to see that $D \subset D_x \times D_y$. Now

consider two closed intervals $I_x \subset D_x$ and $I_y \subset D_y$ over which μ_h-horizontal and μ_v-vertical curves are defined.

Definition 1. *Let $0 \leq \mu_h < +\infty$. A μ_h-horizontal curve $\overline{H}$ is defined to be the graph of a function $h : I_x \to \mathbb{R}$ where h satisfies the following two conditions:*

1. *The set $\overline{H} = \{(x, h(x)) \in \mathbb{R}^2 \mid x \in I_x\}$ is contained in D.*
2. *For every $x_1, x_2 \in I_x$ the Lipschitz condition*

$$|h(x_1) - h(x_2)| \leq \mu_h |x_1 - x_2| \text{is satisfied.} \tag{2.7}$$

Similarly, let $0 \leq \mu_v < +\infty$. A μ_v-vertical curve $\overline{V}$ is defined to be the graph of a function $v : I_y \to \mathbb{R}$ where v satisfies the following two conditions:

1. *The set $\overline{V} = \{(v(y), y) \in \mathbb{R}^2 \mid y \in I_y\}$ is contained in D.*
2. *For every $y_1, y_2 \in I_y$ the Lipschitz condition*

$$|v(y_1) - v(y_2)| \leq \mu_v |y_1 - y_2| \text{is satisfied.} \tag{2.8}$$

Next these curves are "fattened" into strips.

Definition 2. *Given two nonintersecting μ_v-vertical curves $v_1(y) < v_2(y)$, $y \in I_y$, a μ_v-vertical strip is defined as*

$$V = \{(x, y) \in \mathbb{R}^2 \mid x \in [v_1(y), v_2(y)],\ y \in I_y\}. \tag{2.9}$$

Similarly, given two nonintersecting μ_h-horizontal curves $h_1(x) < h_2(x)$, $x \in I_x$, a μ_h-horizontal strip is defined as

$$H = \{(x, y) \in \mathbb{R}^2 \mid y \in [h_1(x), h_2(x)],\ x \in I_x\}. \tag{2.10}$$

The width of horizontal and vertical strips is defined as

$$d(H) = \max_{x \in I_x} |h_2(x) - h_1(x)| \quad , \quad d(V) = \max_{y \in I_y} |v_2(y) - v_1(y)|. \tag{2.11}$$

Different parts of the boundary of the strips are required to be considered in relation to the domain over which they are defined. The following three definitions provide the necessary concepts.

Definition 3. *The vertical boundary of a μ_h-horizontal strip H is denoted*

$$\partial_v H \equiv \{(x, y) \in H \mid x \in \partial I_x\}. \tag{2.12}$$

The horizontal boundary of a μ_h-horizontal strip H is denoted

$$\partial_h H \equiv \partial H \setminus \partial_v H. \tag{2.13}$$

Definition 4. *H is said to be a μ_h-horizontal strip contained in a μ_v-vertical strip V if the two μ_h horizontal curves defining the horizontal boundaries of H (denoted by $\partial_h H$) are contained in V, with the remaining boundary components of H (denoted by $\partial_v H$) contained in $\partial_v V$. These two last subsets, $\partial_h H$ and $\partial_v H$ are referred to as the horizontal and vertical boundaries of H, respectively. See Figure 2.1.*

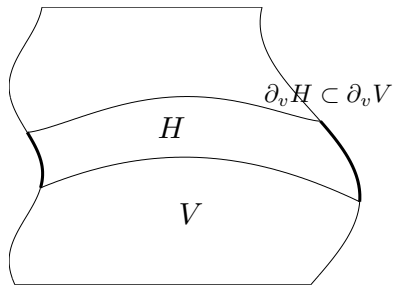

Figure 2.1: H is bounded by two μ_h-horizontal curves, each of them linking the two μ_v-vertical curves composing $\partial_v V$.

Definition 5. *Let V and $\widetilde{V}$ be μ_v-vertical strips. $\widetilde{V}$ is said to intersect V fully if $\widetilde{V} \subset V$ and $\partial_h \widetilde{V} \subset \partial_h V$. See Figure 2.2.*

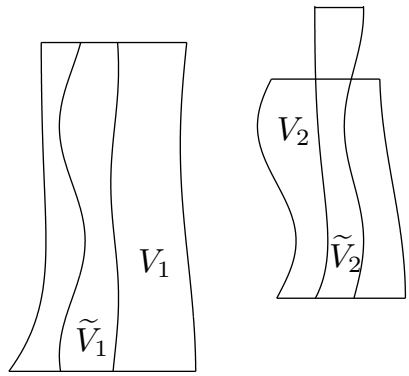

Figure 2.2: $\widetilde{V}_1$ intersects V_1 fully. This does not happen for $\widetilde{V}_2$ and V_2.

2.2 The main theorem

In this section it is proved the main general theorem which provides sufficient conditions for the existence of a chaotic invariant set for nonautonomous maps. In the course of the proof the meaning of "chaos" for nonautonomous dynamics will be made precise.

Following the original development of the Conley-Moser conditions [Moser, 1973] there are three geometrical and analytical conditions which, if satisfied, provide sufficient conditions for an autonomous map (in the original formulation) to present a chaotic invariant set. These are referred to as A1, A2, and A3. The conditions A1 and A2 provide sufficient conditions for the existence of a topological chaotic invariant set. The conditions A1 and A3 provide sufficient conditions for a hyperbolic chaotic invariant set. Conditions A1 and A2 were developed for nonautonomous dynamics in [Wiggins, 1999]. In this section A1 and A2 are recalled, but a new construction of A3 for nonautonomous dynamics[1] is also given. In particular it is shown that A1 and A3 imply that A1 and A2 also hold.

The following two lemmas play an important role in the proof of the main theorem.

Lemma 1. *i) If $V_1 \supset V_2 \supset \cdots \supset V_k \supset \cdots$ is a nested sequence of μ_v-vertical strips with $d(V_k) \to 0$ as $k \to \infty$, then $\cap_{k=1}^{\infty} V_k \equiv V_\infty$ is a μ_v-vertical curve.*

ii) If $H_1 \supset H_2 \supset \cdots \supset H_k \supset \cdots$ is a nested sequence of μ_h-horizontal strips with $d(H_k) \to 0$ as $k \to \infty$, then $\cap_{k=1}^{\infty} H_k \equiv H_\infty$ is a μ_h-horizontal curve.

Lemma 2. *Suppose $0 \leq \mu_v \mu_h < 1$. Then a μ_v-vertical curve and a μ_h-horizontal curve intersect in a unique point.*

The proof of both these two lemmas can be found in [Wiggins, 2003].

[1] A minor technical point is pointed out here. In previous development of the Conley-Moser conditions (e.g. [Moser, 1973; Wiggins, 2003]) the set-up considers the mapping of horizontal strips to vertical strips. However, for the Hénon map it is more natural to consider vertical strips mapping to horizontal strips. Of course, the choice of what is referred to as "horizontal" and "vertical" is arbitrary. However, the same choice of coordinate labeling as is used in the previous literature can be used for the Hénon map if a rotation $P = \begin{pmatrix} 0 & 1 \\ 1 & 0 \end{pmatrix}$ is imposed on the sequence of maps $\{f_n\}_{n=-\infty}^{+\infty}$ or, alternatively, take each map f_n as f_{-n}^{-1} for every $n \in \mathbb{Z}$.

It is assumed that for each $D_n \subset \mathbb{R}^2$

$$f_n(D_n) \cap D_{n+1} \neq \emptyset \ , \quad \forall n \in \mathbb{Z}. \tag{2.14}$$

Furthermore it is assumed that on each D_n one can find a set of disjoint μ_v vertical strips $D_V^n \equiv \cup_{i=1}^N V_i^n$ such that each f_n is one-to-one over $D_V^n \equiv \cup_{i=1}^N V_i^n$. Therefore it is defined

$$\begin{aligned} H_{ij}^{n+1} &\equiv f_n(V_i^n) \cap V_j^{n+1} = H_i^{n+1} \cap V_j^{n+1} \\ \text{and} \quad V_{ji}^n &\equiv f_n^{-1}(V_j^{n+1}) \cap V_i^n \end{aligned} \tag{2.15}$$

with inverse function f_n^{-1} defined on

$$D_H^{n+1} \equiv \cup_{i=1}^N H_i^{n+1} = f_n\left(\cup_{i=1}^N V_i^n\right) \quad \text{for every } n \in \mathbb{Z}.$$

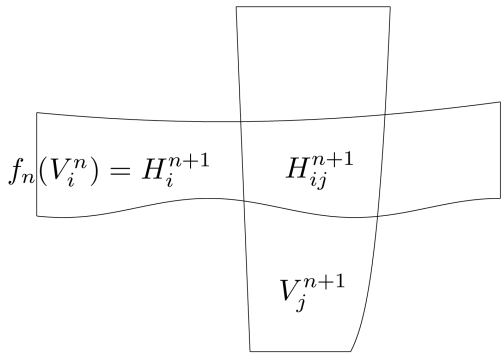

Figure 2.3: Assuming that A1 is satisfied for a given sequence of maps, this figure illustrates that every non empty $H_{ij}^{n+1} \subset D_{n+1}$ is a μ_h-horizontal strip contained in V_j^{n+1}. This also shows that the two μ_h-horizontal curves which form the boundary $\partial_h f_n(V_i^n) = \partial_h(H_i^{n+1})$ cut the vertical boundary of V_j^{n+1} in exactly four points.

The transition matrix $\{A^n\}_{n=-\infty}^{+\infty}$ is defined as follows

$$A_{ij}^n = \begin{cases} 1 & \text{if } H_{ij}^{n+1} = H_i^{n+1} \cap V_j^{n+1} \neq \emptyset \\ 0 & \text{otherwise} \end{cases} \quad \forall i,j \in I. \tag{2.16}$$

At this point the already given concepts allow to state the first two Conley-Moser conditions for a sequence of maps, which are sufficient conditions to prove the existence of a chaotic invariant set for nonautonomous systems.

Assumption (A1). *For all $i, j \in I$ such that $A_{ij}^n = 1$, H_{ij}^{n+1} is a μ_h-horizontal strip contained in V_j^{n+1} with $0 \leq \mu_v \mu_h < 1$. Moreover, f_n maps V_{ji}^n homeomorphically onto H_{ij}^{n+1} with $f_n^{-1}(\partial_h H_{ij}^{n+1}) \subset \partial_h V_i^n$.*

Also since f_n maps V_{ji}^n homeomorphically onto H_{ij}^{n+1} with $f_n^{-1}(\partial_h H_{ij}^{n+1}) \subset \partial_h V_i^n$ then f_n^{-1} maps H_{ij}^{n+1} homeomorphically onto V_{ji}^n $(\forall i, j \in I)$ with

$$f_n\left(f_n^{-1}(\partial_h H_{ij}^{n+1})\right) = \partial_h H_{ij}^{n+1} \subset f_n(\partial_h V_i^n). \tag{2.17}$$

Assumption (A2). *Let V^{n+1} be a μ_v-vertical strip which intersects V_j^{n+1} fully. Then $f_n^{-1}(V^{n+1}) \cap V_i^n \equiv \widetilde{V}_i^n$ is a μ_v-vertical strip intersecting V_i^n fully for all $i \in I$ such that $A_{ij}^n = 1$. Moreover,*

$$d(\widetilde{V}_i^n) \leq \nu_v \; d(V^{n+1}) \quad \textit{for some} \quad 0 < \nu_v < 1. \tag{2.18}$$

Similarly, let H^n be a μ_h-horizontal strip contained in V_j^n such that also $H^n \subset H_{ij}^n$ for some $i, j \in I$ with $A_{ij}^{n-1} = 1$. Then $f_n(H^n) \cap V_k^{n+1} \equiv \widetilde{H}_k^{n+1}$ is a μ_h-horizontal strip contained in V_k^{n+1} for all $k \in I$ such that $A_{jk}^n = 1$. Moreover,

$$d(\widetilde{H}_k^{n+1}) \leq \nu_h \; d(H^n) \quad \textit{for some} \quad 0 < \nu_h < 1. \tag{2.19}$$

Now the symbolic dynamics are developed in a form appropriate for nonautonomous dynamics. Let

$$s = (\cdots s_{n-k} \cdots s_{n-2} s_{n-1} . s_n s_{n+1} \cdots s_{n+k} \cdots) \tag{2.20}$$

denote a bi-infinite sequence with $s_l \in I$ $(\forall l \in \mathbb{Z})$ where adjacent elements of the sequence satisfy the rule $A_{s_n s_{n+1}}^n = 1$, $\forall n \in \mathbb{Z}$.

Similarly to the symbolic dynamics implemented for the Smale horseshoe (see page 575 of [Wiggins, 2003]), here the set of all such symbol sequences is denoted by $\Sigma_{\{A^n\}}^N$. If σ denotes the shift map

$$\sigma(s) = \sigma(\cdots s_{n-2} s_{n-1} . s_n s_{n+1} \cdots) = (\cdots s_{n-2} s_{n-1} s_n . s_{n+1} \cdots) \tag{2.21}$$

on $\Sigma_{\{A^n\}}^N$, the "extended shift map" $\tilde{\sigma}$ on $\widetilde{\Sigma} \equiv \Sigma_{\{A^n\}}^N \times \mathbb{Z}$ comes defined by

$$\tilde{\sigma}(s, n) = (\sigma(s), n+1). \quad \text{Moreover, } f(x, y; n) = (f_n(x, y), n+1). \tag{2.22}$$

Now there exist enough conditions to state the main theorem.

Theorem 3 (Main theorem). *Suppose* $\{f_n, D_n\}_{n=-\infty}^{+\infty}$ *satisfies A1 and A2. There exists a sequence of sets* $\Lambda_n \subset D_n$*, with* $f_n(\Lambda_n) = \Lambda_{n+1}$*, such that the following diagram commutes*

$$\begin{array}{ccc} & \overset{f}{} & \\ \Lambda_n \times \mathbb{Z} & \longrightarrow & \Lambda_{n+1} \times \mathbb{Z} \\ \phi \quad \downarrow & & \downarrow \quad \phi \\ & \overset{\tilde{\sigma}}{} & \\ \Sigma^N_{\{A^n\}} \times \mathbb{Z} & \longrightarrow & \Sigma^N_{\{A^n\}} \times \mathbb{Z} \end{array} \tag{2.23}$$

where $\phi(x, y; n) \equiv (\phi_n(x, y), n)$ *with* $\phi_n(x, y)$ *a homeomorphism mapping* Λ_n *onto* $\Sigma^N_{\{A^n\}}$.

Remark 1. The sequence of sets $\{\Lambda_n\}_{n=-\infty}^{+\infty}$ is what is referred to as a chaotic set for nonautonomous dynamics. Consequently our "main theorem" is a theoretical result which gives sufficient conditions for the existence of such a sequence of sets. The original proof can be found in [Wiggins, 1999], keeping in mind the geometrical considerations mentioned before. □

In next subsection the third Conley-Moser condition is generalized to the nonautonomous case. This will provide an alternative and more analytical (as opposed to topological) method for proving that the second Conley-Moser condition holds, and it will also provide the additional information that the chaotic invariant set is hyperbolic.

2.2.1 Nonautonomous third Conley-Moser condition

A natural definition of stable and unstable sector bundles is given for the nonautonomous setting:

$$\mathcal{V}^n \equiv \bigcup_{i,j \in I} V^n_{ji} = \bigcup_{i,j \in I} f_n^{-1}(V_j^{n+1}) \cap V_i^n, \tag{2.24}$$

$$\mathcal{H}^{n+1} \equiv \bigcup_{i,j \in I} H^{n+1}_{ij} = \bigcup_{i,j \in I} H_i^{n+1} \cap V_j^n, \quad f_n(\mathcal{V}^n) = \mathcal{H}^{n+1}, \tag{2.25}$$

$$S^u_{\mathcal{K}} \equiv \{(\xi_z, \eta_z) \in \mathbb{R}^2 \mid |\eta_z| \leq \mu_h |\xi_z|,\ z \in \mathcal{K}\} \text{ (unstable sector bundle)}, \tag{2.26}$$

$$S^s_{\mathcal{K}} \equiv \{(\xi_z, \eta_z) \in \mathbb{R}^2 \mid |\xi_z| \leq \mu_v |\eta_z|,\ z \in \mathcal{K}\} \quad \text{(stable sector bundle)}, \tag{2.27}$$

with $\mathcal{K}$ being either $\mathcal{V}^n$ or $\mathcal{H}^{n+1}$.

With this notation now it is possible to state the following assumption: the third Conley-Moser condition for the nonautonomous setting.

Assumption (A3). $Df_n(S^u_{\mathcal{V}^n}) \subset S^u_{\mathcal{H}^{n+1}}$, $Df_n^{-1}(S^s_{\mathcal{H}^{n+1}}) \subset S^s_{\mathcal{V}^n}$.

Moreover, if $(\xi_{f_n(z_0^n)}, \eta_{f_n(z_0^n)}) \equiv Df_n(z_0^n)\cdot(\xi_{z_0^n}, \eta_{z_0^n}) \in S^u_{\mathcal{H}^{n+1}}$ *then*

$$|\xi_{f_n(z_0^n)}| \geq \left(\frac{1}{\mu}\right)|\xi_{z_0^n}|. \tag{2.28}$$

If $(\xi_{f_n^{-1}(z_0^{n+1})}, \eta_{f_n^{-1}(z_0^{n+1})}) \equiv Df_n^{-1}(z_0^{n+1})\cdot(\xi_{z_0^{n+1}}, \eta_{z_0^{n+1}}) \in S^s_{\mathcal{V}^n}$ *then*

$$|\eta_{f_n^{-1}(z_0^{n+1})}| \geq \left(\frac{1}{\mu}\right)|\eta_{z_0^{n+1}}| \quad \textit{for } \mu > 0. \tag{2.29}$$

Obviously an additional condition is required in order to guarantee the existence of the Jacobian matrices Df_n and Df_n^{-1}. From now it is considered that $f_n, f_n^{-1} \in C^1$ for every $n \in \mathbb{Z}$ on their respective domains. Now it is possible to establish an important relationship between assumptions A2 and A3.

Theorem 4. *If nonautonomous A1 and A3 are satisfied for* $0 < \mu < 1-\mu_h\mu_v$ *then A2 is satisfied.*

Part of the proof of this theorem is based on the following result.

Lemma 5. *Let* $\{f_n, D_n\}_{n=-\infty}^{+\infty}$ *be a sequence of maps satisfying A1 and A3. For every* $n \in \mathbb{Z}$ *and every pair of indices* $i, j \in I$ *the following statements are true:*

i) if $\overline{V}^{n+1} \subset V_j^{n+1}$ *is a* μ_v*-vertical curve, then* $f_n^{-1}(\overline{V}^{n+1}) \cap V_i^n$ *is a* μ_v*-vertical curve in case* $\overline{V}^{n+1} \cap H_i^{n+1} \neq \emptyset$.

ii) if $\overline{H}^n \subset V_{ji}^n$ *is a* μ_h*-horizontal curve, then* $f_n(\overline{H}^n) \cap H_i^{n+1}$ *is a* μ_h*-horizontal curve in case* $\overline{H}^n \cap V_i^n \neq \emptyset$.

Proof. The proof of ii) is omitted as it follows the same line of reasoning as i).

Let $\overline{V}^{n+1} \subset V_j^{n+1}$ be a μ_v-vertical curve. By definition there exist an interval $T \subset \mathbb{R}$ and a function $v : T \to \mathbb{R}$ such that $\overline{V}^{n+1}$ is the graph of v and also the Lipschitz condition $|v(t_1) - v(t_2)| \leq \mu_v|t_1 - t_2|$ holds for a constant $\mu_v > 0$ and every pair of points $t_1, t_2 \in T$.

It follows from Assumption 1 that (f_n^{-1}) is a homeomorphism over $H_{ij}^{n+1} = H_i^{n+1} \cap V_j^{n+1}$. In particular a homeomorphism over $\overline{V}^{n+1} \cap H_i^{n+1} \neq \emptyset$. This implies that

$$f_n^{-1}(\overline{V}^{n+1} \cap H_i^{n+1}) = f_n^{-1}(\overline{V}^{n+1}) \cap f_n^{-1}(H_i^{n+1}) = f_n^{-1}(\overline{V}^{n+1}) \cap V_i^n \neq \emptyset. \quad (2.30)$$

Since the curve $\overline{V}^{n+1}$ can be parametrized by $(v(t), t)|_{t \in T}$ (take also $v \in C^1$) then this last subset $f_n^{-1}(\overline{V}^{n+1}) \cap V_i^n$ can also have a parametrization but over a smaller domain $T^* \subset T$:

$$\begin{pmatrix} x(t) \\ y(t) \end{pmatrix} = f_n^{-1}(v(t), t) \quad \text{with} \quad t \in T^* \equiv \{\bar{t} \in T : (v(\bar{t}), \bar{t}) \in H_i^{n+1}\}. \quad (2.31)$$

The image of ant tangent vector of $\overline{V}^{n+1}$ under Df_n^{-1} has the form

$$\begin{pmatrix} \dot{x}(t) \\ \dot{y}(t) \end{pmatrix} = Df_n^{-1}(v(t), t) \cdot \begin{pmatrix} \dot{v}(t) \\ 1 \end{pmatrix}$$

$$\text{with} \quad \begin{pmatrix} \dot{v}(t) \\ 1 \end{pmatrix} \in S^s_{\mathcal{H}^{n+1}}, \quad \forall t \in T^*. \quad (2.32)$$

This last relation follows directly from the Lipschitz condition

$$|\dot{v}(t)| \leq \limsup_{\substack{\epsilon \to 0 \\ (t+\epsilon) \in T^*}} \left| \frac{v(t+\epsilon) - v(t)}{\epsilon} \right| \leq \limsup_{\substack{t_1 \in T^* \\ t_1 \neq t}} \frac{|v(t_1) - v(t)|}{|t_1 - t|} \leq$$

$$\leq \limsup_{\substack{t_1 \in T^* \\ t_1 \neq t}} \frac{\mu_v |t_1 - t|}{|t_1 - t|} = \mu_v. \quad (2.33)$$

By applying Assumption 3 the tangent vectors belong to $S^s_{\mathcal{V}^n}$:

$$|\dot{x}(t)| \leq \mu_v \cdot |\dot{y}(t)|, \quad \forall t \in T^*. \quad (2.34)$$

Moreover as it is assumed that $(f_n^{-1}) \in C^1$, any tangent vector

$$\begin{pmatrix} \dot{x}(t) \\ \dot{y}(t) \end{pmatrix} = Df_n^{-1}(v(t), t) \cdot \begin{pmatrix} \dot{v}(t) \\ 1 \end{pmatrix}$$

$$\text{cannot be equal to} \begin{pmatrix} 0 \\ 0 \end{pmatrix} \text{ at any point } t \in T^*.$$

From these two relations it follows that $\dot{y}(t)$ cannot change its sign in the entire domain T^*. Consequently for every pair of points $(x_1, y_1), (x_2, y_2) \in$

$f_n^{-1}(\overline{V}^{n+1}) \cap V_i^n$ there exist $t_1, t_2 \in T^*$ such that $(x_k, y_k) = (x(t_k, y(t_k))$, $(k = 1, 2)$ and this leads to the inequality

$$|x_1 - x_2| = |x(t_1) - x(t_2)| = \left| \int_{t_2}^{t_1} \dot{x}(t)dt \right| \leq \int_{t_2}^{t_1} |\dot{x}(t)|dt \leq \mu_v \int_{t_2}^{t_1} |\dot{y}(t)|dt =$$

$$= \mu_v \left| \int_{t_2}^{t_1} \dot{y}(t)dt \right| = \mu_v |y(t_1) - y(t_2)| = \mu_v |y_1 - y_2|, \tag{2.35}$$

and this result implies that $f_n^{-1}(\overline{V}^{n+1}) \cap V_i^n$ is a μ_v-vertical curve. □

Proof of Theorem 4. The theorem will be proved by verifying the following steps.

Step 1: Let $\overline{V}^{n+1} \subset V_j^{n+1}$ be a μ_v-vertical curve. Then $f_n^{-1}(\overline{V}^{n+1}) \cap V_i^n$ is a μ_v-vertical curve for every $i \in I$ such that $\overline{V}^{n+1} \cap H_i^{n+1} \neq \emptyset$.

Step 2: Let V^{n+1} be a μ_v-vertical strip which intersects V_j^{n+1} fully. Then $f_n^{-1}(V^{n+1}) \cap V_i^n$ is a μ_v-vertical strip that intersects V_i^n fully for every $i \in I$ such that $V^{n+1} \cap H_i^{n+1} \neq \emptyset$.

Step 3: Show that $d(\widetilde{V}_i^n) \leq (\mu/(1-\mu_h\mu_v)) \cdot d(V^{n+1})$ for $\widetilde{V}_i^n = f_n^{-1}(V^{n+1}) \cap V_i^n$.

The part of the proof dealing with horizontal strips is omitted since it follows from the same reasoning used to prove the part concerning vertical strips.

At Step 1, let $\overline{V}^{n+1} \subset V_j^{n+1}$ be a μ_v-vertical curve. For each $i \in I$ such that $\overline{V}^{n+1} \cap H_i^{n+1} \neq \emptyset$, by applying A1 it follows that $H_{ij}^{n+1} = V_j^{n+1} \cap H_i^{n+1} \neq \emptyset$ is a μ_h-horizontal strip contained in V_j^{n+1}. Since implicitly $\overline{V}^{n+1}$ is considered as one of the two components of the vertical boundary of a vertical strip V^{n+1} intersecting V_j^{n+1} fully, the curve $\overline{V}^{n+1}$ intersects $\partial_h H_i^{n+1}$ in exactly two points.

Also because f_n^{-1} maps the horizontal boundaries of each subset $H_{ij}^{n+1} (= H_i^{n+1} \cap V_j^{n+1})$ onto the horizontal boundaries of V_i^n, it follows that $f_n^{-1}(\overline{V}^{n+1}) \cap V_i^n$ is a curve linking the two horizontal boundaries of V_i^n. Finally if by applying Lemma 5 to this curve then $f_n^{-1}(\overline{V}^{n+1}) \cap V_i^n$ is also a μ_v-vertical curve.

To prove Step 2, the statement of Step 1 is applied to the μ_v-vertical boundaries of the μ_v-vertical strip V^{n+1} which intersects V_j^{n+1} fully. It then follows that $f_n^{-1}(V^{n+1}) \cap V_i^n$ is also a μ_v-vertical strip for every $i \in I$ such that

$V^{n+1} \cap H_i^{n+1} \neq \emptyset$. Moreover this last strip intersects each V_i^n fully because of the geometric considerations in Step 1.

For proving Step 3 it is firstly needed to fix an iteration $n \in \mathbb{Z}$ and an index $i \in I$. The width of each μ_v-vertical strip $\widetilde{V}_i^n$ will be the distance between two points $p_0, p_1 \in \widetilde{V}_i^n$ with the same y-component and located in separate vertical boundaries, $d(\widetilde{V}_i^n) = |p_1 - p_0|$.

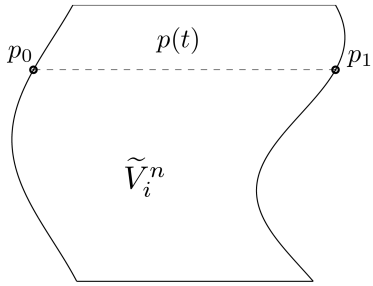

Figure 2.4: The segment $p(t) = tp_1 + (1-t)p_0$, $t \in [0,1]$ which represents the maximum amplitude of $\widetilde{V}_i^n$ is obviously a μ_h-horizontal curve.

By taking segment $p(t)$ considered in Figure 2.2.1, $\dot{p}(t) = p_1 - p_0$ is a vector with its y-component equal to zero. Therefore $\dot{p}(t) \in S^u_{\mathcal{V}^n}$, $\forall t \in [0,1]$. Now the curve $f_n(p(t)) \equiv z(t) = (x(t), y(t))$ located in D_{n+1} is a μ_h-horizontal curve because of the second part of Lemma 5. Moreover A3 states that

$$\dot{z}(t) = D(f_n(p(t))) = Df_n(p(t)) \cdot \dot{p}(t) \in S^u_{\mathcal{H}^{n+1}}. \tag{2.36}$$

Furthermore since the graph of $z(t) = (x(t), y(t))$ is a μ_h-horizontal curve,

$$|y(1) - y(0)| \leq \mu_h |x(1) - x(0)| \quad \rightarrow \quad |y_1 - y_0| \leq \mu_h |x_1 - x_0|, \tag{2.37}$$

by denoting $(x_i, y_i) \equiv (x(i), y(i)) = z(i) = f_n(p(i)) = f_n(p_i)$ for $i = 0, 1$.

Using this last fact and also the geometric considerations in Figure 2.5, it follows that

$$\begin{aligned} |x_1 - x_0| = |v_1(y_1) - v_0(y_0)| \leq |v_1(y_1) - v_1(y_0)| + |v_1(y_0) - v_0(y_0)| \leq \\ \leq \mu_v |y_1 - y_0| + d(V^{n+1}) \leq \mu_v \mu_h |x_1 - x_0| + d(V^{n+1}) \rightarrow \\ \rightarrow \quad |x_1 - x_0| \leq \frac{d(V^{n+1})}{(1 - \mu_h \mu_v)}. \end{aligned} \tag{2.38}$$

In addition, as a result of the last part of Assumption 3, there exists a

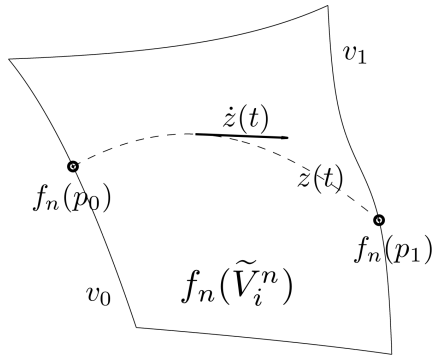

Figure 2.5: $f_n(p_0)$ and $f_n(p_1)$ are on the graphs of two distinct μ_v-vertical curves, denoted by v_0 and v_1 respectively.

positive constant μ imposed to be $\mu < 1 - \mu_h\mu_v$ such that

$$|\dot{x}(t)| \geq \left(\frac{1}{\mu}\right)|\dot{p}(t)| = \left(\frac{1}{\mu}\right)|p_1 - p_0| \quad \text{and then}$$

$$d(\widetilde{V}_i^n) = |p_1 - p_0| \leq \mu \int_0^1 |\dot{x}(t)|dt = \mu \left| \int_0^1 \dot{x}(t)dt \right| = \mu|x_1 - x_0|. \tag{2.39}$$

Note that the two expressions containing the integrals are equal since $\dot{x}(t)$ does not change its sign at any point. This is due to the fact that the graph of $z(t) = (x(t), y(t))$ is a μ_h-horizontal curve.

Finally this leads to the result

$$d(\widetilde{V}_i^n) = |p_1 - p_0| \leq \mu|x_1 - x_0| \leq \frac{\mu}{(1 - \mu_h\mu_v)} d(V^{n+1}) \quad \text{and} \tag{2.40}$$

$$\nu_v = \frac{\mu}{(1 - \mu_h\mu_v)} < 1 \quad \text{will be the required constant for Assumption 2.}$$

□

2.3 Nonautonomous Hénon map

At this point the necessary tools for proving the existence of a chaotic invariant set for the nonautonomous Hénon map are already developed. Recall the general notation for nonautonomous dynamics (a sequence of maps defined on a sequence of domains), $\{f_n, D_n\}_{n=-\infty}^{+\infty}$.

The domains D_n for the nonautonomous Hénon map will be constructed in such a way that each of them contains an associated pair of horizontal strips and another of vertical strips. Moreover the transition matrices will be

shown to be identical for each map f_n, with $A = \begin{pmatrix} 1 & 1 \\ 1 & 1 \end{pmatrix}$ for each iteration n.

Recall that the autonomous Hénon map takes the form

$$H(x, y) = (A + By - x^2, x),$$

$$\text{with inverse function} \quad H^{-1}(x, y) = (y, (x - A + y^2)/B). \tag{2.41}$$

Following [Devaney & Nitecki, 1979], sufficient conditions for the existence of a chaotic invariant set in the autonomous context can be proven when the parameters satisfy the following inequalities in case that $B = \pm 1$

$$A > A_2 = \frac{(5 + 2\sqrt{5})(1 + |B|)^2}{4}, \quad A_2 = 5 + 2\sqrt{5} \approx 9.47. \tag{2.42}$$

Note that when $B = -1$ the map is orientation-preserving and area-preserving. For the version of the nonautonomous Hénon map exposed onwards, this parameter is chosen to be $B = -1$ for the sequence of maps $\{f_n, D_n\}_{n=-\infty}^{+\infty}$ in order to retain these properties, but parameter A will vary for each iteration n. Therefore

$$f_n(x, y) = (A(n) - y - x^2, x), \quad f_n^{-1}(x, y) = (y, A(n) - x - y^2) \tag{2.43}$$

$$\text{where} \quad A(n) = 9.5 + \epsilon \cdot \cos(n) \quad \text{with} \quad \epsilon = 0.1. \tag{2.44}$$

This choice is motivated by the fact that $A_2 = 5+2\sqrt{5} \approx 9.47$ is the minimum threshold for parameter A for which the autonomous Hénon map satisfies the autonomous versions of Assumptions 1 and 3 of the Conley-Moser conditions.

In the following it is proved that this version of nonautonomous Hénon map satisfies the conditions described in Theorem 3. In particular the following theorem is proved.

Theorem 6. *If $A^* \geq 9.5$ then the nonautonomous Hénon map $f_n = (A(n) - y - x^2, x)$ with $A(n) = A^* + \epsilon \cdot \cos(n)$, $\epsilon = 0.1$ has a nonautonomous chaotic invariant set in $\mathbb{R}^2$.*

Proof. This proof is carried out for the specific case where $A_0 = 9.5$. The case for $A_0 > 9.5$ follows similar reasoning as for the case $A_0 = 9.5$ with the main difference being that some values in the inequalities appearing when checking Assumption 3 must be changed. The starting point of the proof is the first Conley-Moser condition.

Assumption 1. The domain D_n on which each function f_n will be defined is the square

$$D_n = D = [-R, R] \times [-R, R]$$
$$\text{with} \quad R = \sup_{n\in\mathbb{Z}} R(n) = 1 + \sqrt{1 + A(0)} \approx 4.25 \tag{2.45}$$

analogously to the domain considered for the autonomous Hénon map.

The horizontal strips and the vertical strips associated to any iteration $n \in \mathbb{Z}$ will be taken as

$$D_H^{n+1} \equiv f_n(D) \cap D, \quad D_V^n \equiv f_n^{-1}(D) \cap D \tag{2.46}$$

and since f_n is a homeomorphism it follows that vertical strips "move" to horizontal strips in forward iteration:

$$f_n(D_V^n) = f_n\left(f_n^{-1}(D) \cap D\right) = (f_n \circ f_n^{-1})(D) \cap f_n(D) = D_H^{n+1}. \tag{2.47}$$

Moreover the index I indicating the number of strips in either D_H^n or D_V^n is $I = \{1, 2\}$ and the strips are defined by

$$\begin{aligned} H_1^{n+1} &\equiv f_n(D) \cap ([-R, R] \times [0, R]), \\ H_2^{n+1} &\equiv f_n(D) \cap ([-R, R] \times [-R, 0]), \\ V_1^n &\equiv f_n^{-1}(D) \cap ([0, R] \times [-R, R]), \\ V_2^n &\equiv f_n^{-1}(D) \cap ([-R, 0] \times [-R, R]). \end{aligned} \tag{2.48}$$

These are determined by the images of D with respect to f_n and f_n^{-1} for every $n \in \mathbb{Z}$. They result easy to compute. Let

$$L_1 = \{(x, y) \in D \mid y = R\}, \quad L_2 = \{(x, y) \in D \mid y = -R\},$$
$$L_3 = \{(x, y) \in D \mid x = R\}, \quad L_4 = \{(x, y) \in D \mid x = -R\}$$

be the segments which conform the boundary of D. Their images with respect f_n and f_n^{-1} are either another segment or a parabola, and as f_n is a homeomorphism, both $f_n(D)$ and $f_n^{-1}(D)$ are two strips with a parabolic form.

The key points of $f_n(D)$ and $f_n^{-1}(D)$ shown in Figure 2.6 take the following coordinates

$$p_1 \equiv (A(n) + R, 0),\ p_2 \equiv (A(n) - R, 0),\ p_3 \equiv (A(n) + R - R^2, -R),$$
$$p_4 \equiv (A(n) - R - R^2, -R),\ p_5 \equiv (A(n) - R - R^2, R),\ p_6 \equiv (A(n) + R - R^2, R),$$

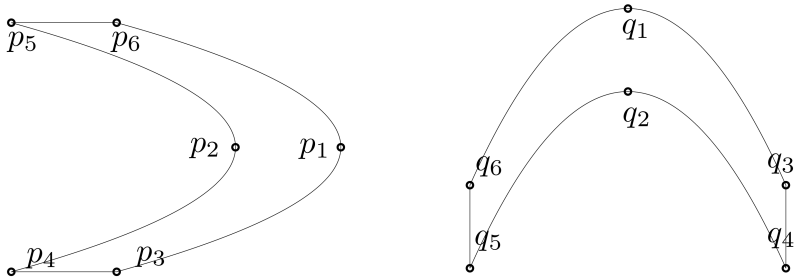

Figure 2.6: $f_n(D)$ and $f_n^{-1}(D)$ take these two shapes respectively, for any given $n \in \mathbb{Z}$. The set of points $p_1, p_2, p_3, p_4, p_5, p_6$ and $q_1, q_2, q_3, q_4, q_5, q_6$ determine the height and length of both geometric forms.

$$q_1 \equiv (0, A(n) + R),\ q_2 \equiv (0, A(n) - R),\ q_3 \equiv (R, A(n) + R - R^2),$$
$$q_4 \equiv (R, A(n) - R - R^2),\ q_5 \equiv (-R, A(n) - R - R^2),\ q_6 \equiv (-R, A(n) + R - R^2).$$

The coordinates of these points satisfy $A(n) > 2R$, $\forall n \in \mathbb{Z}$ and

$$A(n) + R - R^2 = A(n) + 1 + \sqrt{1 + A(0)} - (1 + \sqrt{1 + A(0)})^2 =$$
$$= (A(n) - A(0)) - R \leq -R \tag{2.49}$$

with strict inequality when $n \neq 0$. Only in case $n = 0$, the points $p_6, p_3 = q_6, q_3$ are inside the domain D and actually these are three vertices of the square D. In any case, it follows that the points p_1, p_2, p_4, p_5 and q_1, q_2, q_4, q_5 do not belong to D for any n.

The arguments of the parabolic curves are denoted by X and Y, therefore their equations take the expressions

$$Y = \sqrt{A(n) - R - X} \quad \text{in the horizontal case,} \tag{2.50}$$

$$X = \sqrt{A(n) - R - Y} \quad \text{in the vertical case.} \tag{2.51}$$

By using this notation the absolute value of the derivatives of these functions

$$\left|\frac{dY}{dX}\right| = \frac{1}{2\sqrt{A(n) - R - X}} \quad , \quad \left|\frac{dX}{dY}\right| = \frac{1}{2\sqrt{A(n) - R - Y}} \tag{2.52}$$

and their maximum values are assumed when $X = R$ and $Y = R$ respectively. Consequently

$$\frac{1}{2\sqrt{A(n) - 2R}} \leq \frac{1}{2\sqrt{9.5 + \epsilon\cos(n) - 2R}} \approx \frac{1}{2\sqrt{9.5 - 0.1 - 8.5}} \approx 0.527.$$

Due to reasons explained later, for convenience the thresholds μ_h, μ_v are chosen to be $\mu_h = \mu_v = 0.615$ for the maximum values that the slopes of the horizontal and vertical boundaries can assume, respectively. Using this fact, one can conclude that H_i^{n+1} is a μ_h-horizontal strip and V_i^n a μ_v-vertical strip for every $i \in I$ and $n \in \mathbb{Z}$. Moreover, $\mu_h \cdot \mu_v = (0.615)^2 = 0.378225 < 1$. This proves part of Assumption 1.

Furthermore for any $i, j \in I$ and $n \in \mathbb{Z}$ the horizontal boundaries of $f_n(V_i^n) = H_i^{n+1}$ are two μ_h-horizontal curves which link the left and right sides of the square D. Since the two μ_v-vertical curves bounding $\partial_v V_j^{n+1}$ link the upper and the bottom sides of D_{n+1}, both boundaries $\partial_h f_n(V_i^n)$ and $\partial_v V_j^{n+1}$ intersect in four different points. From this fact it follows that $H_{ij}^{n+1} = f_n(V_i^n) \cap V_j^{n+1}$ is a μ_h-horizontal strip contained in V_j^{n+1}.

Since f_n is a homeomorphism for every $n \in \mathbb{Z}$,

$$f_n \text{ maps } V_{ji}^n = f_n^{-1}(V_j^{n+1}) \cap V_i^n = f_n^{-1}\left(f_n(V_i^n) \cap V_j^{n+1}\right) \text{ onto } H_{ij}^{n+1}$$
$$\text{and } f_n^{-1}\left(\partial_h H_{ij}^{n+1}\right) \subset \partial_h V_i^n \text{ because } \partial_h H_{ij}^{n+1} \subset \partial_h H_i^{n+1}. \tag{2.53}$$

This can be checked by an easy computation. Therefore the nonautonomous Hénon map satisfies Assumption 1.

Assumption 3. To start with the verification of A3, it results important to recall the notation for several concepts developed earlier:

$$Df_n(x,y) = \begin{pmatrix} -2x & -1 \\ 1 & 0 \end{pmatrix}, \quad Df_n^{-1}(x,y) = \begin{pmatrix} 0 & 1 \\ -1 & -2y \end{pmatrix}, \tag{2.54}$$

$$S_{\mathcal{K}}^u = \{(\xi_z, \eta_z) \in \mathbb{R}^2 \mid |\eta_z| \leq \mu_h |\xi_z|,\ z \in \mathcal{K}\},$$
$$S_{\mathcal{K}}^s = \{(\xi_z, \eta_z) \in \mathbb{R}^2 \mid |\xi_z| \leq \mu_v |\eta_z|,\ z \in \mathcal{K}\},$$

with $\mathcal{K}$ being either $\mathcal{V}^n$ or $\mathcal{H}^{n+1}$.

Now given any point $z_0 = (x_0, y_0) \in \mathcal{H}^{n+1}$ and any $(\xi_{z_0}, \eta_{z_0}) \in S_{\mathcal{H}^{n+1}}^s$ (which by definition, $|\xi_{z_0}| \leq \mu_v |\eta_{z_0}|$) the product

$$Df_n^{-1}(z_0) \cdot (\xi_{z_0}, \eta_{z_0}) = \begin{pmatrix} 0 & 1 \\ -1 & -2y_0 \end{pmatrix} \cdot \begin{pmatrix} \xi_{z_0} \\ \eta_{z_0} \end{pmatrix} = \begin{pmatrix} \eta_{z_0} \\ -\xi_{z_0} - 2y_0\eta_{z_0} \end{pmatrix}$$

belongs to $S_{\mathcal{V}^n}^s$ if and only if the inequality

$$|\eta_{z_0}| \leq \mu_v \cdot |\xi_{z_0} + 2y_0\eta_{z_0}| \quad \text{holds.} \tag{2.55}$$

Since it is also true that

$$\mu_v \cdot |\xi_{z_0} + 2y_0\eta_{z_0}| \geq \mu_v \cdot [2|y_0||\eta_{z_0}| - |\xi_{z_0}|] \geq$$
$$\geq \mu_v \cdot [2|y_0||\eta_{z_0}| - \mu_v|\eta_{z_0}|] = \left(2|y_0|\mu_v - \mu_v^2\right)|\eta_{z_0}|. \tag{2.56}$$

In case $\left(2|y_0|\mu_v - \mu_v^2\right) \geq 1$, the previous inequality (2.55) will hold.

To verify this it is needed to check if

$$|y_0| \geq \frac{1}{2}\left(\mu_v + \frac{1}{\mu_v}\right) = 1.1205 \quad \text{for any } z_0 = (x_0, y_0) \in \mathcal{H}^{n+1}. \tag{2.57}$$

At this point a geometrical argument is given.

• The horizontal lines $\{Y = \pm 1.1205\}$ cut the parabola $\{X = A(n) - R - Y^2\}$ at two points

$$(x_1, y_1) = (8.5 + \epsilon\cos(n) - \sqrt{10.6} - 1.2555, 1.1205) \quad \text{and}$$
$$(x_2, y_2) = (8.5 + \epsilon\cos(n) - \sqrt{10.6} - 1.2555, -1.1205).$$

• The horizontal lines $\{Y = \pm 1.1205\}$ cut the parabola $\{Y = A(n+1) + R - X^2\}$ at two points with a positive x-component

$$(\bar{x}_1, \bar{y}_1) = (\sqrt{10.5 + \epsilon\cos(n+1) + \sqrt{10.6} - 1.1205}, 1.1205) \quad \text{and}$$
$$(\bar{x}_2, \bar{y}_2) = (\sqrt{10.5 + \epsilon\cos(n+1) + \sqrt{10.6} + 1.1205}, -1.1205).$$

From here one can conclude

$$\bar{x}_1 < \bar{x}_2 = \sqrt{10.5 + \epsilon\cos(n+1) + \sqrt{10.6} + 1.1205} \leq \sqrt{10.6 + \sqrt{10.6} + 1.1205}$$
$$= \sqrt{14.9758} = 3.8699 < 3.8887 = 8.5 - 0.1 - \sqrt{10.6} - 1.2555$$
$$\leq 8.5 + \epsilon\cos(n) - \sqrt{10.6} - 1.2555 = x_2 = x_1 < 4.25 < R, \quad \forall n \in \mathbb{Z}. \tag{2.58}$$

The inequalities $\bar{x}_1 < \bar{x}_2 < x_2 = x_1$ (note that $\bar{x}_1 < \bar{x}_2$ is trivial due to the definitions) also hold for every parameter $A(n) = A^* + \epsilon\cos(n)$ satisfying $A^* \geq 9.5$ and $\epsilon = 0.1$. The reason comes from comparing the derivatives of $\bar{x}_2$ and x_2 with respect to A^*:

$$\bar{x}_2 = \sqrt{A^* + \epsilon\cos(n+1) + 1 + \sqrt{1 + A^* + \epsilon\cos(n)} + 1.1205}$$

$$\geq \sqrt{10.4+\sqrt{10.4}+1.1205} \approx 3.84,$$

$$x_2 = A^* + \epsilon\cos(n) - 1 - \sqrt{1+A^*+\epsilon\cos(n)} - 1.1205,$$

$$\frac{d\bar{x}_2}{dA^*} = \frac{1}{2\bar{x}_2}\cdot\left(1+\frac{1}{2\sqrt{1+A^*+\epsilon\cos(n)}}\right) \leq \frac{1}{2\bar{x}_2}\cdot\left(1+\frac{1}{2\sqrt{1+A^*-\epsilon}}\right)$$

$$\leq \frac{1}{2\bar{x}_2}\cdot\left(1+\frac{1}{2\sqrt{10.4}}\right) \leq \frac{1}{2\cdot 3.84}\cdot\left(1+\frac{1}{2\sqrt{10.4}}\right) \approx 0.1504,$$

$$\frac{dx_2}{dA^*} = 1-\frac{1}{2\sqrt{1+A^*+\epsilon\cos(n)}} \geq 1-\frac{1}{2\sqrt{1+A^*-\epsilon}} \geq 1-\frac{1}{2\sqrt{10.4}} \approx 0.8450.$$

Clearly $\frac{d\bar{x}_2}{dA^*} < \frac{dx_2}{dA^*}$ for every $A^* \geq 9.5$. It follows that $\bar{x}_2 < x_2$ for $A^* \geq 9.5$.

This setup shows that every point $z_0 = (x_0, y_0) \in \mathcal{H}^{n+1}$ satisfies that $|y_0| > 1.1205 = \frac{1}{2}\left(\mu_v + \frac{1}{\mu_v}\right)$, since the four areas composing $\mathcal{H}^{n+1}$ are either beneath the line $\{Y = -1.1205\}$ or above the line $\{Y = 1.1205\}$, as can be observed in Figure 2.7.

Since $z_0 \in \mathcal{H}^{n+1}$ is an arbitrary point, the inclusion $Df_n^{-1}(S^s_{\mathcal{H}^{n+1}}) \subset S^s_{\mathcal{V}^n}$ is proven.

For the second inclusion $Df_n(S^u_{\mathcal{V}^n}) \subset S^u_{\mathcal{H}^{n+1}}$ consider the fact that $\mathcal{V}^n = f_n^{-1}(\mathcal{H}^{n+1})$. Moreover since $f_n^{-1}(x,y) = (y, A(n) - x - y^2)$ transforms the y-components of the points of $\mathcal{H}^{n+1}$ into the x-components of the points of $\mathcal{V}^n$, it immediately follows that

$$|x_0| > \frac{1}{2}\left(\mu_v + \frac{1}{\mu_v}\right) = \frac{1}{2}\left(\mu_h + \frac{1}{\mu_h}\right) \text{ for every } z_0 = (x_0, y_0) \in \mathcal{V}^n. \quad (2.59)$$

As in the previous case this inequality allows to prove the inclusion

$$Df_n(z_0)\cdot(\xi_{z_0}, \eta_{z_0}) = \begin{pmatrix} -2x_0 & -1 \\ 1 & 0 \end{pmatrix}\cdot\begin{pmatrix} \xi_{z_0} \\ \eta_{z_0} \end{pmatrix} = \begin{pmatrix} -2x_0\xi_{z_0} - \eta_{z_0} \\ \xi_{z_0} \end{pmatrix} \in S^u_{\mathcal{H}^{n+1}}$$

$$\text{if and only if} \quad |\xi_{z_0}| \leq \mu_h \cdot |2x_0\xi_{z_0} + \eta_{z_0}|. \quad (2.60)$$

Taking in mind that $(\xi_{z_0}, \eta_{z_0}) \in S^u_{\mathcal{V}^n}$ and then $|\eta_{z_0}| \leq \mu_h|\xi_{z_0}|$, one observes

$$\mu_h \cdot |2x_0\xi_{z_0} + \eta_{z_0}| \geq \mu_h \cdot [2|x_0||\xi_{z_0}| - |\eta_{z_0}|]$$

$$\geq \mu_h \cdot [2|x_0||\xi_{z_0}| - \mu_h|\xi_{z_0}|] = \left[2|x_0|\mu_h - \mu_h^2\right]|\xi_{z_0}|$$

$$\geq \left[2\mu_h \cdot \frac{1}{2}\left(\mu_h + \frac{1}{\mu_h}\right) - \mu_h^2\right]|\xi_{z_0}| = \left[\mu_h^2 + 1 - \mu_h^2\right]|\xi_{z_0}| = |\xi_{z_0}| \quad (2.61)$$

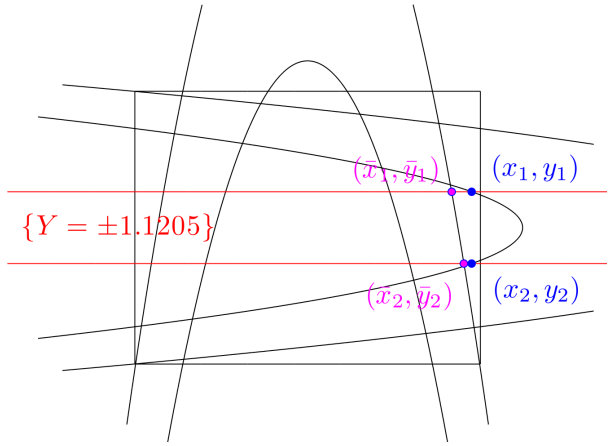

Figure 2.7: The four areas composing $\mathcal{H}^{n+1}$ are those bounded by the four parabolic strips (two horizontal and two vertical) contained in the square domain D_{n+1}.

and then the inclusion $Df_n(S^u_{\mathcal{V}^n}) \subset S^u_{\mathcal{H}^{n+1}}$ is proved.

Finally for the last part of Assumption 3 it is only required to prove the inequality

$$|\eta_{f_n^{-1}(z_0)}| \geq \frac{1}{\mu}|\eta_{z_0}| \quad \text{for } 0 < \mu < 1 - \mu_h\mu_v \tag{2.62}$$

and $z_0 \in \mathcal{H}^{n+1}$, $(\xi_{z_0}, \eta_{z_0}) \in S^s_{\mathcal{H}^{n+1}}$, since the inequality

$$|\xi_{f_n(z_0)}| \geq \frac{1}{\mu}|\xi_{z_0}|, \quad \text{with } z_0 \in \mathcal{V}^n,\ (\xi_{z_0}, \eta_{z_0}) \in S^u_{\mathcal{V}^n} \tag{2.63}$$

is proved by using the same argument. Hence

$$|\eta_{f_n^{-1}(z_0)}| = |2y_0\eta_{z_0} + \xi_{z_0}| \geq 2|y_0||\eta_{z_0}| - |\xi_{z_0}| \geq 2|y_0||\eta_{z_0}| - \mu_v|\eta_{z_0}|$$

$$= [2|y_0| - \mu_v]\,|\eta_{z_0}| \geq \frac{1}{\mu}|\eta_{z_0}| \quad \text{if and only if}$$

$$2|y_0| - \mu_v \geq \frac{1}{\mu} \quad \longleftrightarrow \quad |y_0| \geq \frac{1}{2}\left(\mu_v + \frac{1}{\mu}\right). \tag{2.64}$$

This last inequality is true in case that $\mu_v < \mu < 1 - \mu_h\mu_v$. This interval exists since $\mu_v = 0.615$ is less than $(1 - \mu_h\mu_v) = 0.621775$. Therefore

$$|y_0| > \frac{1}{2}\left(\mu_v + \frac{1}{\mu_v}\right) > \frac{1}{2}\left(\mu_v + \frac{1}{\mu}\right) \text{ for every } z_0 = (x_0, y_0) \in \mathcal{H}^{n+1}. \tag{2.65}$$

Analogously for any $z_0 = (x_0, y_0) \in \mathcal{V}^n$,

$$|x_0| > \frac{1}{2}\left(\mu_h + \frac{1}{\mu_h}\right) > \frac{1}{2}\left(\mu_h + \frac{1}{\mu}\right) \tag{2.66}$$

and the proof that the nonautonomous Hénon map satisfies A1 and A3 with $0 < \mu < 1 - \mu_h\mu_v$ is complete. Consequently it also satisfies A2 by using Theorem 4.

By applying the main theorem it follows that there exists a chaotic invariant set $\{\Lambda_n\}_{n=-\infty}^{+\infty}$ (with respect to the nonautonomous Hénon map $\{f_n\}$) contained in $\{D_n\}_{n=-\infty}^{+\infty}$ (let say $\Lambda_n \subset D_n = D$ and $f_n(\Lambda_n) = \Lambda_{n+1}$) which is conjugate to a shift map of two symbols. □

Remark 2. Comparing this result to the situation for the autonomous Hénon map, it results curious that for some $n \in \mathbb{Z}$ the quantity $A(n) = 9.5 + \epsilon\cos(n)$ is less than $A_2 = 5+2\sqrt{5} \approx 9.47$, which is actually the minimum threshold for parameter A for which the autonomous Hénon map satisfies the autonomous Assumption 3.

In other words, this given example shows that although for some $n \in \mathbb{Z}$ the values that parameter A takes imply that f_n does not satisfy the autonomous Assumption 3 separately, this fact does not necessarily mean that the nonautonomous Assumption 3 is not satisfied for the sequence $\{f_n\}_{n=-\infty}^{+\infty}$. □

In this chapter a nonautonomous version of the Hénon map has been introduced. Necessary conditions have been provided for this map to possess a nonautonomous chaotic invariant set. This has been accomplished by using a nonautonomous version of the Conley-Moser conditions given in [Wiggins, 1999]. These were sharpen by providing a more analytical condition that, as a consequence, enables to show that the chaotic invariant set is hyperbolic. In the course of the proof a precise characterization of what is mean by the phrase "hyperbolic chaotic invariant set" for nonautomous dynamical systems has been provided. Currently there is much interest in nonautomous dynamics and a thorough analysis of a specific example might provide a benchmark for further studies, just as the work in [Devaney & Nitecki, 1979] provided a benchmark for studies of chaotic dynamics for autonomous maps. Indeed this generalization of the Hénon map to the nonautonomous setting provides an approach to generalizing the map to even more general nonautonomous settings, such as a consideration of "noise". This would be an interesting topic for future studies. Finally a graphical approximation to the chaotic invariant set generated by the nonautonomous Hénon map is provided in Appendix 1.

Chapter 3

Notions on nonautonomous dynamics

In this chapter, several definitions and formal aspects of nonautonomous dynamical systems are provided as they are required for use in Chapter 4. These are notions coming from the classical theory of autonomous dynamical sytems, and are adapted to the nonautonomous framework. For instance, in this setting, due to the explicit dependence on the time variable t (or the iteration n) of the dynamical systems (1.1), the concept of hyperbolic equilibrium point is replaced by that of hyperbolic trajectory. This new context is illustrated in Figure 3.1 by the graphical representation of the dynamics induced by a nonautonomous system in the so-called extended phase space, which includes the time variable t in the representation. From this figure it is clear that phase space structures are "moving" in the nonautonomous case, while those of an autonomous system are not. More formally, the extended phase space of a nonautonomous dynamical system shows that the locations of the hyperbolic trajectories, as well as those of their stable and unstable manifolds, are different at different time slices, while this is not the case for autonomous systems. This representation is adapted for the continuous time case in which $\mathbb{T} = \mathbb{R}$, but it is also valid for the discrete time case in which $\mathbb{T} = \mathbb{Z}$. This context motivates a re-statement of the basic notions on dynamical systems.

The starting point of this concept re-formulation is the definition of a solution mapping for a nonautonomous dynamical system. Taking as reference the book by Kloeden & Rasmussen [2011], solution mappings are defined over a general temporal domain $\mathbb{T}$ and over an open spatial domain $X \subseteq \mathbb{R}^N$. For an autonomous dynamical system the solution mapping is usually referred to as a flow and depends only on two variables: the independent (or temporal) variable $t \in \mathbb{T}$ and the initial condition $\mathbf{x}_0 \in X$, although this flow function might not be defined over the entire domains $\mathbb{T}$ and X. For any fixed initial

condition $\mathbf{x}_0 \in X$, the flow mapping $\phi(\cdot, \mathbf{x}_0)$ is a solution of the differential or difference equation associated to the dynamical system. Formally, it satisfies the properties in next definition.

Definition 6 (Flow). *A flow is a continuous function $\phi : \mathbb{T} \times X \to X$ which satisfies the following two properties,*

(i) Initial value condition. $\phi(0, x_0) = x_0$ for all $x_0 \in X$,

(ii) Group property. $\phi(s+t, x_0) = \phi(s, \phi(t, x_0))$ for all $s, t \in \mathbb{T}$ and $x_0 \in X$.

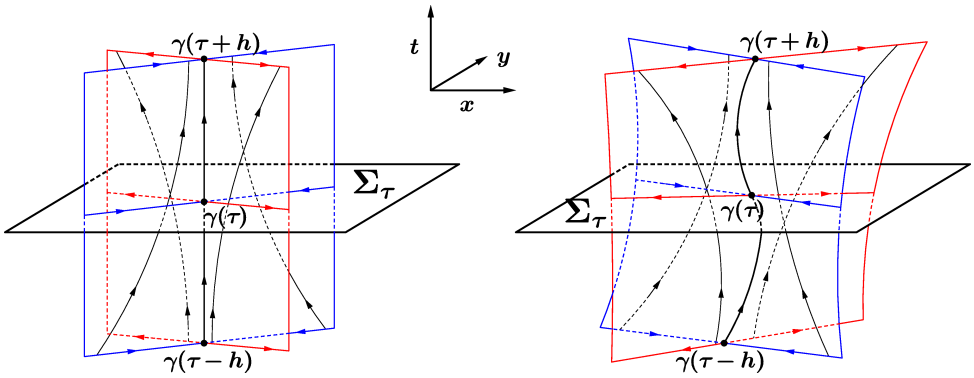

Figure 3.1: Geometry of the stable and unstable subspaces $E^s(t)$ and $E^u(t)$ (depicted in blue and red colour respectively) of the linearized system associated with the hyperbolic trajectory $\gamma(t)$, both in the extended phase space and on a time slice $\Sigma_{t=\tau}$. The left-hand picture corresponds to an autonomous dynamical system, for which the stable and unstable subspaces $E^s(t)$ and $E^u(t)$ remain constant at every time slice Σ_t, and the hyperbolic trajectory $\gamma(t)$ is nothing else than a stationary fixed point. The right-hand picture draws a hyperbolic trajectory $\gamma(t)$ of a nonautonomous system with its corresponding stable and unstable subspaces $E^s(t)$ and $E^u(t)$ evolving in time. In both pictures several trajectories with initial conditions in $E^s(\tau - h)$ and $E^u(\tau - h)$ are tracked along the time period $(\tau - h, \tau + h)$ and projected onto the stable and unstable subspaces in the full extended subspace.

The solution mappings for nonautonomous dynamical systems (either a nonautonomous velocity field or a map) are known as processes (a notion also taken from [Kloeden & Rasmussen, 2011]) and present many similarities with flows in the autonomous setting. The main difference is that ϕ depends on an extra variable t_0, the initial time when the solution $\mathbf{x}(t)$ passes through $\mathbf{x}_0$, let us say $\mathbf{x}(t_0) = \mathbf{x}_0$, due to the time dependence of the dynamical system.

Definition 7 (**Process**). *A process is a continuous mapping* $(t, t_0, x_0) \mapsto \phi(t, t_0, x_0) \in X$ *for* $t, t_0 \in \mathbb{T}$ *and* $x_0 \in X$*, which satisfies the initial value and evolution properties,*

(i) $\phi(t_0, t_0, x_0) = x_0$ *for all* $t_0 \in \mathbb{T}$ *and* $x_0 \in X$*,*

(ii) $\phi(t_2, t_0, x_0) = \phi(t_2, t_1, \phi(t_1, t_0, x_0))$ *for all* $t_0, t_1, t_2 \in \mathbb{T}$ *and* $x_0 \in X$*.*

These two last definitions assume that either the flow or process generated by the dynamical system are invertible, which is consistent with the maps and velocity fields considered in this work. Otherwise some technical aspects should be included in these definitions. These two are applicable to both discrete-time and continuous-time dynamical systems, however this notation is used in the latter case much more frequently, for which $\mathbb{T} = \mathbb{R}$. The usual notation for nonautonomous maps is

$$f_n \equiv \phi(n+1, n, \cdot), \quad f_n(\mathbf{x}) = \phi(n+1, n, \mathbf{x}) \text{ for every } n \in \mathbb{Z} \text{ and } \mathbf{x} \in X, \tag{3.1}$$

the one used in Chapter 2 about chaotic dynamics.

A remark here is that the solution mapping of any discrete-time dynamical system (either a flow or a process) needs to be continuous only on the spatial domain X, due to the discrete topology of the temporal domain $\mathbb{T} = \mathbb{Z}$.

Once the solution mapping ϕ of a nonautonomous dynamical system is established, we are ready to introduce the notion of invariance. As mentioned in the introduction one main objective of this thesis is the characterization of the phase space structures generated by a nonautonomous dynamical system by applying the method of Lagrangian descriptors, and these structures share the same property: the invariance with respect to ϕ. The following definition is adapted from [Kloeden *et al.*, 2013].

Definition 8 (**Invariant set**). *A collection* $\mathcal{A} = \{A_t : t \in \mathbb{T}\}$ *of nonempty subsets of* X *is invariant under a process* ϕ *on* X*, or* ϕ*-invariant, if*

$$\phi(t_1, t_0, A_{t_0}) = A_{t_1} \quad \text{for all } t_0, t_1 \in \mathbb{T},$$

or, equivalently, if $f_n(A_n) = A_{n+1}$ *for all* $n \in \mathbb{Z}$ *in case that* $\mathbb{T} = \mathbb{Z}$*.*

It is thus clear from that every trajectory generated by any nonautonomous dynamical system is invariant with respect to the corresponding process ϕ. Among the set of all possible trajectories

$$\{\phi(t, t_0, x_0) \in X : t \in \mathbb{T}\}_{t_0 \in \mathbb{T}, x_0 \in X},$$

the focus is on those that exhibit a division between different circulation regimes such as the hyperbolic trajectories. Their particularity is that they hold an attracting and repelling behaviour over their neighbouring trajectories. Hyperbolic equilibrium points of autonomous systems have trajectories belonging to the stable and unstable manifolds, which display such behaviour in their neighbourhood, and similarly occurs for the hyperbolic trajectories of nonautonomous systems. According to Wiggins [2003], the trajectory $\gamma(t)$ of a sufficiently differentiable velocity field $\dot{\mathbf{x}} = f(\mathbf{x}, t)$ (f is C^r with $r \geq 1$) is said to be hyperbolic if the associated linearized system

$$\dot{\xi} = D_{\mathbf{x}} f(\gamma(t), t) \cdot \xi \tag{3.2}$$

presents an exponential dichotomy.

Providing a full description of the formalism behind the notions dealing with hyperbolicity, as the previous definition of exponential dichotomy, is beyond the scope of this chapter. Briefly, this notion implies the existence of two time-evolving linearly independent subspaces $E^s(t)$ and $E^u(t)$, respectively indicating the stable and unstable directions of the hyperbolic trajectory $\gamma(t)$. These stable and unstable subspaces of $\gamma(t)$ display the locations at which the trajectories passing through them at time $t \in \mathbb{T}$ approximate in an exponential way to the hyperbolic trajectory asymptotically (induced by the linear velocity field $D_{\mathbf{x}} f$) when $t \to +\infty$ or $t \to -\infty$ respectively, in the same way that the eigenvectors associated to a constant matrix $A \in \mathcal{M}_{N \times N}$ work for a saddle point of an autonomous system $\dot{\mathbf{x}} = A\mathbf{x}$. These concepts are illustrated in Figure 3.1.

This statement only works for the linearized velocity field (3.2) of a more general nonautonomous dynamical system. Nevertheless, this result constitutes a good approximation to the dynamics of the trajectories passing through a neighbourhood of the hyperbolic trajectory. Indeed, the existence of the stable and unstable manifolds of $\gamma(t)$ is guaranteed once the presence of an exponential dichotomy is proved, due to the application of the "Theorem of Local Stable and Unstable Manifolds" in [Wiggins, 2003], which has been demonstrated in several ways by different authors. For instance, a discrete time version of this theorem can be found in [Katok & Hasselblatt, 1995]. At this point it is important to recall that there exist similarities between the stable and unstable manifolds of a hyperbolic trajectory $\gamma(t)$ and those of a hyperbolic equilibrium point in an autonomous setting: these are material curves for which every trajectory passing through them approximates asymptotically to $\gamma(t)$ in forward and backward time, depending on the stable or unstable nature of such curves.

These formally defined structures cannot be strictly computed in finite time

data sets, as required in applications in geophysical contexts. The reason is that these previous notions, the hyperbolic trajectories and their stable and unstable manifolds are defined for an infinite time period $\mathbb{T}$ and involve an asymptotic nature. Mancho *et al.* [2006] addressed this challenge for realistic ocean flows by identifying distinguished hyperbolic trajectories (concept introduced in Chapter 1) in a finite data set, and by computing stable and unstable manifolds as curves advected by the velocity field. At the initial integration time, the curves are small segments aligned with the stable and unstable subspaces of the linearized system (3.2). This initial step aims to build a finite-time version of the asymptotic property of manifolds. Mendoza & Mancho [2010, 2012] have performed systematic numerical computations of invariant manifolds in geophysical flows, where manifolds are defined in a constructive way, and have found that they are aligned with singular features of Lagrangian descriptors.

In this setting it is only possible to talk in terms of approximations to the dynamical structures, a point further justified in Chapter 4. Basic terminology for Stochastic Differential Equations (SDEs) and their solutions is introduced next. This will support the generalization of Lagrangian descriptors to this context, which will be addressed in Chapter 4. These concepts and examples are taken from [Balibrea-Iniesta *et al.*, 2016]. SDEs still constitute a nonautonomous framework for dynamical systems whose particularity is the random time-dependence of coefficients in the equations, and therefore the random evolution of their solutions. Due to this fact, the SDE setting is usually referred to as nonautonomous and non-deterministic.

3.1 Preliminary concepts on SDEs

The general framework in which Lagrangian descriptors (in their stochastic version) are defined, requires to carefully describe the nature of solutions of a stochastic differential equation (SDE). Therefore, to start a general system of SDEs expressed in differential form is considered:

$$dX_t = b(X_t, t)dt + \sigma(X_t, t)dW_t, \quad t \in \mathbb{R}, \tag{3.3}$$

where $b(\cdot) \in C^1(\mathbb{R}^N \times \mathbb{R})$ is the deterministic part, $\sigma(\cdot) \in C^1(\mathbb{R}^N \times \mathbb{R})$ is the random forcing, W_t is a Wiener process (also called Brownian motion) whose definition is given later, and X_t is the solution of the equation. All these functions take values in $\mathbb{R}^N$.

As the notion of solution of a SDE is closely related with the Wiener process, it remains to state what is meant by $W(\cdot)$. This definition is given in [Duan, 2015], and this reference serves to provide the background for all of

the notions in this section. Also throughout this thesis it is used Ω to denote the probability space where the Wiener process is defined.

Definition 9 (**Wiener process**). *A real valued stochastic Wiener or Brownian process $W(\cdot)$ is a stochastic process defined in a probability space $(\Omega, \mathcal{F}, \mathcal{P})$ which satisfies*

(i) $W_0 = 0$ *(standard Brownian motion),*

(ii) $W_t - W_s$ *follows a Normal distribution* $N(0, t-s)$ *for all* $t \geq s \geq 0$,

(iii) for all time $0 < t_1 < t_2 < ... < t_n$, *the random variables* $W_{t_1}, W_{t_2} - W_{t_1}, ..., W_{t_n} - W_{t_{n-1}}$ *are independent (independent increments).*

Moreover, $W(\cdot)$ is a real valued two-sided Wiener process if conditions (ii) and (iii) change into

(ii) $W_t - W_s$ *follows a Normal distribution* $N(0, |t-s|)$ *for all* $t, s \in \mathbb{R}$,

(iii) for all time $t_1, t_2, ..., t_{2n} \in \mathbb{R}$ *such that the intervals* $\{(t_{2i-1}, t_{2i})\}_{i=1}^n$ *are non-intersecting between them*[1], *the random variables* $W_{t_1} - W_{t_2}, W_{t_3} - W_{t_4}, ..., W_{t_{2n-1}} - W_{t_{2n}}$ *are independent.*

As it is mentioned in the introduction, one purpose of this work is to develop the method of Lagrangian descriptors for SDEs. This method of Lagrangian descriptors has been developed for deterministic differential equations whose temporal domain is $\mathbb{R}$. In this sense it is natural to work with two-sided solutions as well as two-sided Wiener processes. Henceforth, every Wiener process $W(\cdot)$ considered in this work will be of this form.

Given that any Wiener process $W(\cdot)$ is a stochastic process, by definition this is a family of random real variables $\{W_t, t \in \mathbb{R}\}$ in such a way that for each $\omega \in \Omega$ there exists a mapping

$$t \longmapsto W_t(\omega)$$

known as the trajectory of a Wiener process.

Analogously to the Wiener process, the solution X_t of the SDE (3.3) is

[1] The notation (t_{2i-1}, t_{2i}) refers to the interval of points between the values t_{2i-1} and t_{2i}, regardless the order of the two extreme values. Also with the asertion every pair of intervals of the family $\{(t_{2i-1}, t_{2i})\}_{i=1}^n$ is imposed to have an empty intersection, or alternatively the union $\bigcup_{i=1}^n (t_{2i-1}, t_{2i})$ is conformed by n distinct intervals over $\mathbb{R}$.

also a stochastic process. In particular, it is a family of random variables $\{X_t, t \in \mathbb{R}\}$ such that for each $\omega \in \Omega$, the trajectory of X_t satisfies

$$t \longmapsto X_t(\omega) = X_0(\omega) + \int_0^t b(X_s(\omega), s)ds + \int_0^t \sigma(X_s(\omega), s)dW_s(\omega), \quad (3.4)$$

where $X_0 : \Omega \to \mathbb{R}^N$ is the initial condition. In addition, as $b(\cdot)$ and $\sigma(\cdot)$ are smooth functions, they are locally Lipschitz and this leads to existence and pathway uniqueness of a local, continuous solution (see [Duan, 2015]). That is if any two stochastic processes X^1 and X^2 are local solutions in time of SDE (3.3), then $X_t^1(\omega) = X_t^2(\omega)$ over a time interval $t \in (t_i, t_f)$ and for almost every $\omega \in \Omega$.

At each instant of time t, the deterministic integral $\int_0^t b(X_s(\omega))ds$ is defined by the usual Riemann integration scheme since b is assumed to be a differentiable function. However, the stochastic integral term is chosen to be defined by the Itô integral scheme

$$\int_0^t \sigma(X_s(\omega), s)dW_s(\omega)$$

$$= \lim_{N\to\infty} \sum_{i=0}^{N-1} \sigma(X_{i\frac{t}{N}}(\omega), it/N) \cdot \left[W_{(i+1)\frac{t}{N}}(\omega) - W_{i\frac{t}{N}}(\omega)\right]. \quad (3.5)$$

This scheme will also facilitate the implementation of a numerical method for computing approximations for the solution X_t in Chapter 4.

Once the notion of solution X_t of a SDE (3.3) is established, it is natural to ask if the same notions and ideas familar from the study of deterministic differential equations from the dynamical systems point of view are still valid for SDEs. In particular, the notion of hyperbolic trajectory and its stable and unstable manifolds are studied in the context of SDEs. In addition it is considered how such notions would manifest themselves in the context of *phase space transport* for SDEs, and the stochastic Lagrangian descriptor will play a key role in considering these questions from a practical point of view.

Firstly the notion of an invariant set for a SDE is discussed. In the deterministic case the simplest possible invariant set is a single trajectory of the differential equation. More precisely, it is the set of points through which a solution passes. Building on this construction, an invariant set is a collection of trajectories of different solutions. This is the most basic way to characterize the invariant sets with respect to a determinsitic differential equation of the form

$$\dot{\mathbf{x}} = f(\mathbf{x}, t), \quad \mathbf{x} \in \mathbb{R}^N, \quad t \in \mathbb{R}. \quad (3.6)$$

For verifying the invariance of such sets the solution mapping generated by the vector field is used. As mentioned in previous section, for deterministic autonomous systems these are referred to as *flows* and for deterministic nonautonomous systems they are referred to as *processes*.

A similar notion of solution mapping for SDEs is introduced using the notion of a random dynamical system φ (henceforth referred to as RDS) in the context of SDEs. This function φ is also a solution mapping of a SDE that satisfies several conditions, but compared with the solution mappings in the deterministic case, this RDS depends on an extra argument which is the random variable $\omega \in \Omega$. Furthermore the random variable ω evolves with respect to t by means of a dynamical system $\{\theta_t\}_{t\in\mathbb{R}}$ defined over the probability space Ω.

Definition 10 (**Random dynamical system**). *Let $\{\theta_t\}_{t\in\mathbb{R}}$ be a measure-preserving*[2] *dynamical system defined over Ω, and let $\varphi : \mathbb{R}\times\Omega\times\mathbb{R}^N \to \mathbb{R}^N$ be a measurable mapping such that $(t,\cdot,x) \mapsto \varphi(t,\omega,x)$ is continuous for all $\omega \in \Omega$, and the family of functions $\{\varphi(t,\omega,\cdot) : \mathbb{R}^N \to \mathbb{R}^N\}$ has the cocycle property*

$$\varphi(0,\omega,x) = x \quad \textit{and} \quad \varphi(t+s,\omega,x) = \varphi(t,\theta_s\omega,\varphi(s,\omega,x))$$
$$\textit{for all } t,s \in \mathbb{R},\ x \in \mathbb{R}^N \textit{ and } \omega \in \Omega.$$

Then the mapping φ is a random dynamical system with respect to the stochastic differential equation

$$dX_t = b(X_t)dt + \sigma(X_t)dW_t$$

if $\varphi(t,\omega,x)$ is a solution of the equation.

Analogous to the deterministic case, the definition of invariance with respect to a SDE can be characterized in terms of a RDS. This is an important topic in our consideration of stochastic Lagrangian descriptors. Now it is introduced an example of a SDE for which the analytical expression of the RDS is obtained. This will be a benchmark example in the development of stochastic Lagrangian descriptors and their relation to stochastic invariant manifolds, taken in Chapter 4.

[2]Given the probability measure $\mathcal{P}$ associated with the space $(\Omega,\mathcal{F},\mathcal{P})$, this remains invariant under the dynamical system $\{\theta_t\}_{t\in\mathbb{R}}$. Formally, $\theta_t\mathcal{P} = \mathcal{P}$ for every $t \in \mathbb{R}$. This statement means that $\mathcal{P}(B) = \mathcal{P}(\theta_t(B))$ for every $t \in \mathbb{R}$ and every subset $B \in \mathcal{F}$. Indeed for any dynamical system $\{\theta_t\}_{t\in\mathbb{R}}$ defined over the same probability space Ω as a Wiener process $W(\cdot)$, the equality $W_s(\theta_t\omega) = W_{t+s}(\omega) - W_t(\omega)$ holds and implies that $dW_s(\theta_t\omega) = dW_{t+s}(\omega)$ for every $s,t \in \mathbb{R}$ (see [Duan, 2015] for a detailed explanation).

Example 1 (**Noisy saddle point**). For the stochastic differential equation

$$\begin{cases} dX_t = X_t dt + dW_t^1 \\ dY_t = -Y_t dt + dW_t^2 \end{cases} \tag{3.7}$$

where W_t^1 and W_t^2 are two different Wiener processes, the solutions take the expressions

$$X_t = e^t \left(X_0(\omega) + \int_0^t e^{-s} dW_s^1(\omega) \right), \quad Y_t = e^{-t} \left(Y_0(\omega) + \int_0^t e^s dW_s^2(\omega) \right)$$

and therefore the random dynamical system φ takes the form

$$\begin{array}{rccc} \varphi: & \mathbb{R} \times \Omega \times \mathbb{R}^2 & \longrightarrow & \mathbb{R}^2 \\ & (t, \omega, (x, y)) & \longmapsto & (\varphi_1(t, \omega, x), \varphi_2(t, \omega, y)) \\ & & & = \left(e^t \left(x + \int_0^t e^{-s} dW_s^1(\omega) \right), e^{-t} \left(y + \int_0^t e^s dW_s^2(\omega) \right) \right). \end{array} \tag{3.8}$$

□

Notice that this last definition (10) is expressed in terms of SDEs with time-independent coefficients b, σ. For more general SDEs a definition of nonautonomous RDS is introduced in Appendix 2, inspired in Definition 7 of processes for deterministic nonautonomous differential equations in previous section. However for the remaining examples considered in Chapter 4 the already given definition of RDS is applied.

Once the notion of RDS is established, it can be used to describe and detect geometrical structures and determine their influence on the dynamics of trajectories. Specifically, in clear analogy with the deterministic autonomous case, the focus is on those trajectories whose expressions do not depend explicitly on time t, which are referred as *random fixed points*. Moreover their stable and unstable manifolds, which may also depend on the random variable ω, are also objects of interest due to their influence on the dynamical behavior of nearby trajectories. Both types of objects are invariant. Therefore it results necessary a characterization of invariant sets with respect to a SDE by means of an associated RDS.

Definition 11 (**Invariant set**). *A non empty collection $M : \Omega \to \mathcal{P}(\mathbb{R}^N)$, where $M(\omega) \subseteq \mathbb{R}^N$ is a closed subset for every $\omega \in \Omega$, is called an invariant set for a random dynamical system φ if*

$$\varphi(t, \omega, M(\omega)) = M(\theta_t \omega) \quad \textit{for every } t \in \mathbb{R} \textit{ and every } \omega \in \Omega. \tag{3.9}$$

Again the noisy saddle (3.7) conforms an illustrative example of a SDE for which several invariant sets can be easily characterized by means of its corresponding RDS.

Example 2 (**Noisy saddle point**)**.** For the stochastic differential equations

$$\begin{cases} dX_t = X_t dt + dW_t^1 \\ dY_t = -Y_t dt + dW_t^2 \end{cases} \tag{3.10}$$

where W_t^1 and W_t^2 are two different Wiener processes, the solution mapping φ is given by the following expression

$$\begin{array}{rccc} \varphi: & \mathbb{R}\times\Omega\times\mathbb{R}^2 & \longrightarrow & \mathbb{R}^2 \\ & (t,\omega,(x,y)) & \longmapsto & (\varphi_1(t,\omega,x),\varphi_2(t,\omega,y)) \\ & & & = \left(e^t\left(x+\int_0^t e^{-s}dW_s^1(\omega)\right), e^{-t}\left(y+\int_0^t e^{s}dW_s^2(\omega)\right)\right). \end{array}$$

Notice that this is a decoupled random dynamical system. There exists a solution whose components do not depend on variable t and are convergent for almost every $\omega\in\Omega$ as a consequence of the properties of Wiener processes (see [Duan, 2015]). This solution takes the form

$$\tilde{X}(\omega) = (\tilde{x}(\omega),\tilde{y}(\omega)) = \left(-\int_0^{\infty} e^{-s}dW_s^1(\omega), \int_{-\infty}^0 e^{s}dW_s^2(\omega)\right).$$

Actually, $\tilde{X}(\omega)$ is a solution because it satisfies the invariance property

$$\begin{aligned} \varphi_1(t,\omega,\tilde{x}(\omega)) &= e^t\left(-\int_0^{+\infty} e^{-s}dW_s^1(\omega)+\int_0^t e^{-s}dW_s^1(\omega)\right) \\ &= -\int_t^{+\infty} e^{-(s-t)}dW_s^1(\omega) = -\int_0^{+\infty} e^{-t'}dW_{t'+t}^1(\omega) \\ &= -\int_0^{+\infty} e^{-t'}dW_{t'}^1(\theta_t\omega) = \tilde{x}(\theta_t\omega) \end{aligned} \tag{3.11}$$

$$\begin{aligned} \varphi_2(t,\omega,\tilde{y}(\omega)) &= e^{-t}\left(\int_{-\infty}^0 e^{s}dW_s^2(\omega)+\int_0^t e^{s}dW_s^2(\omega)\right) \\ &= \int_{-\infty}^t e^{s-t}dW_s^2(\omega) = \int_{-\infty}^0 e^{t'}dW_{t'+t}^2(\omega) \\ &= \int_{-\infty}^0 e^{t'}dW_{t'}^2(\theta_t\omega) = \tilde{y}(\theta_t\omega) \end{aligned} \tag{3.12}$$

in both cases by means of the change of variable $t' = s - t$.

This implies that $\varphi(t,\omega,\tilde{X}(\omega)) = \tilde{X}(\theta_t\omega)$ for every $t\in\mathbb{R}$ and every $\omega\in\Omega$.

Therefore $\tilde{X}(\omega)$ satisfies the invariance property (3.9). This conclusion comes from the fact that $\tilde{x}(\omega)$ and $\tilde{y}(\omega)$ are also invariant under the components φ_1 and φ_2, in case these are seen as separate RDSs defined over $\mathbb{R}$ (see (3.11) and (3.12), respectively).

Due to its independence with respect to the time variable t, it is said that $\tilde{X}(\omega)$ is a random fixed point of the SDE (3.7), or more commonly a stationary orbit. As the trajectory of $\tilde{X}(\omega)$ (and separately its components $\tilde{x}(\omega)$ and $\tilde{y}(\omega)$) is proved to be an invariant set, it is straightforward to check that the two following subsets of $\mathbb{R}^2$,

$$\mathcal{S}(\omega) = \{(x,y) \in \mathbb{R}^2 : x = \tilde{x}(\omega)\}, \quad \mathcal{U}(\omega) = \{(x,y) \in \mathbb{R}^2 : y = \tilde{y}(\omega)\}$$

are also invariant with respect to the RDS φ. Similarly to the deterministic setting, these are referred to as the stable and unstable manifolds of the stationary orbit respectively. Additionally, in order to prove the separating nature of these two manifolds and the stationary orbit with respect to their nearby trajectories, it is considered any other solution $(\overline{x}_t, \overline{y}_t)$ of the noisy saddle with initial conditions at time $t = 0$,

$$\overline{x}_0 = \tilde{x}(\omega) + \epsilon_1(\omega), \quad \overline{y}_0 = \tilde{y}(\omega) + \epsilon_2(\omega),$$

being $\epsilon_1(\omega), \epsilon_2(\omega)$ two random variables.

If the corresponding RDS φ is applied to compare the evolution of this solution $(\overline{x}_t, \overline{y}_t)$ and the stationary orbit, there arises an exponential dichotomy

$$\begin{aligned}
(\overline{x}_t, \overline{y}_t) - (\tilde{x}(\theta_t\omega), \tilde{y}(\theta_t\omega)) &= \varphi(t,\omega,(\overline{x}_0,\overline{y}_0)) - \varphi(t,\omega,(\tilde{x}(\omega),\tilde{y}(\omega))) \\
&= \Big(e^t \left[\overline{x}_0 + \int_0^t e^{-s} dW_s^1(\omega) - \tilde{x}(\omega) - \int_0^t e^{-s} dW_s^1(\omega) \right], \\
&\quad e^{-t} \left[\overline{y}_0 + \int_0^t e^{s} dW_s^2(\omega) - \tilde{y}(\omega) - \int_0^t e^{s} dW_s^2(\omega) \right] \Big) \\
&= \left(e^t \left(\tilde{x}(\omega) + \epsilon_1(\omega) - \tilde{x}(\omega) \right), e^{-t} \left(\tilde{y}(\omega) + \epsilon_2(\omega) - \tilde{y}(\omega) \right) \right) \\
&= \left(\epsilon_1(\omega) e^t, \epsilon_2(\omega) e^{-t} \right). \qquad (3.13)
\end{aligned}$$

Considering that $(\overline{x}_t, \overline{y}_t)$ is different from $(\tilde{x}(\omega), \tilde{y}(\omega))$ then one of the two cases $\epsilon_1 \not\equiv 0$ or $\epsilon_2 \not\equiv 0$ holds, let say $\epsilon_1 \neq 0$ or $\epsilon_2 \neq 0$ for almost every $\omega \in \Omega$. In the first case, the distance between both trajectories $(\overline{x}_t, \overline{y}_t)$ and $(\tilde{x}, \tilde{y})$ increases at an exponential rate in positive time:

$$||\varphi(t,\omega,(\overline{x}_t,\overline{y}_t)) - \varphi(t,\omega,(\tilde{x},\tilde{y}))|| \geq |\epsilon_1(\omega) e^t| \longrightarrow +\infty, \qquad (3.14)$$

when $t \to +\infty$ and for almost every $\omega \in \Omega$.

Similarly to this case, when the second option holds the distance between both trajectories increases at a exponential rate in negative time. It does not matter how close the initial condition $(\overline{x}_0, \overline{x}_0)$ is from $(\tilde{x}(\omega), \tilde{y}(\omega))$ at the initial time $t = 0$. Actually this same exponentially growing separation can be achieved for any other initial time $t \neq 0$. Following these arguments, one can check that the two manifolds $\mathcal{S}(\omega)$ and $\mathcal{U}(\omega)$ also exhibit this same separating behaviour as the stationary orbit. Moreover, it is remarkable that almost surely the stationary orbit is the only solution whose components are bounded. □

These facts highlight the distinguished nature of the stationary orbit (and its manifolds) in the sense that this is an isolated solution from the others. Apart from the fact that $(\tilde{x}, \tilde{y})$ "moves" in a bounded domain for every $t \in \mathbb{R}$, any other trajectory eventually passing through an arbitrary neighborhood of $(\tilde{x}, \tilde{y})$ at any given instant of time t leaves the neighborhood and then separates from the stationary orbit in either positive or negative time. Specifically this separation rate is exponential for the noisy saddle just in the same way as for the deterministic saddle.

These features are also observed for the trajectories within the stable and unstable manifolds of the stationary orbit, but in a more restrictive manner than $(\tilde{x}, \tilde{y})$. Taking for instance an arbitrary trajectory (x^s, y^s) located at $\mathcal{S}(\omega)$ for every $t \in \mathbb{R}$, its first component $x^s_t = \tilde{x}(\omega)$ remains bounded for almost every $\omega \in \Omega$. By contrast any other solution passing arbitrarily closed to (x^s, y^s) neither being part of $\mathcal{S}(\omega)$ nor being the stationary orbit, satisfies the previous inequality (3.14) and therefore separates from $\mathcal{S}(\omega)$ at an exponential rate for increasing time. With this framework there are already enough conditions to establish the formal definitions of stationary orbit and invariant manifold.

Definition 12 (**Stationary orbit**). *A random variable $\tilde{X} : \Omega \to \mathbb{R}^N$ is called a stationary orbit (random fixed point) for a random dynamical system φ if*

$$\varphi(t, \omega, \tilde{X}(\omega)) = \tilde{X}(\theta_t \omega), \quad \textit{for every } t \in \mathbb{R} \textit{ and every } \omega \in \Omega.$$

Obviously every stationary orbit $\tilde{X}(\omega)$ is an invariant set with respect to a RDS as it satisfies Definition 11. Among several definitions of invariant manifolds given in the bibliography (for example [Arnold, 1998; Boxler, 1989; Duan, 2015]), which have different formalisms but share the same philosophy, the one given in [Duan, 2015] is chosen because it adapts to our example in a very direct way.

Definition 13 (**Invariant manifold**). *A random invariant set $M : \Omega \to \mathcal{P}(\mathbb{R}^N)$ for a random dynamical system φ is called a C^k-Lipschitz invariant manifold if it can be represented by a graph of a C^k Lipschitz mapping ($k \geq 1$)*

$$\gamma(\omega, \cdot) : H^+ \to H^-, \quad \textit{with direct sum decomposition } H^+ \oplus H^- = \mathbb{R}^N$$

$$\textit{such that} \quad M(\omega) = \{x^+ \oplus \gamma(\omega, x^+) : x^+ \in H^+\} \quad \textit{for every } \omega \in \Omega.$$

This is a very limitated notion of invariant manifold as its formal definition requires the set to be represented by a Lipschitz graph. Anyway it is consistent with the already established manifolds $\mathcal{S}(\omega)$ and $\mathcal{U}(\omega)$ as these can be represented as the graphs of two functions γ_s and γ_u respectively:

$$\begin{array}{rcccc} \gamma_s(\omega,\cdot) & : & span\{\begin{pmatrix} 0 \\ 1 \end{pmatrix}\} & \longrightarrow & span\{\begin{pmatrix} 1 \\ 0 \end{pmatrix}\} \\ & & \begin{pmatrix} 0 \\ t \end{pmatrix} & \longmapsto & \begin{pmatrix} \tilde{x}(\omega) \\ 0 \end{pmatrix} \end{array} \quad \text{and}$$

$$\begin{array}{rcccc} \gamma_u(\omega,\cdot) & : & span\{\begin{pmatrix} 1 \\ 0 \end{pmatrix}\} & \longrightarrow & span\{\begin{pmatrix} 0 \\ 1 \end{pmatrix}\} \\ & & \begin{pmatrix} t \\ 0 \end{pmatrix} & \longmapsto & \begin{pmatrix} 0 \\ \tilde{y}(\omega) \end{pmatrix} \end{array} . \tag{3.15}$$

Actually the domains of such functions γ_s and γ_u are the linear subspaces $E^s(\omega)$ and $E^u(\omega)$, known as the stable and unstable subspaces of the random dynamical system $\Phi(t, \omega)$. This last mapping is obtained from linearizing the original RDS φ over the stationary orbit $(\tilde{x}, \tilde{y})$. This result serves as an argument to denote $\mathcal{S}(\omega)$ and $\mathcal{U}(\omega)$ as the stable and unstable manifolds of the stationary orbit, not only because these two subsets are invariant under φ as one can deduce from (3.11) and (3.12), but also due to the dynamical behaviour of their trajectories in a neighborhood of the stationary orbit $\tilde{X}(\omega)$. Hence the important characteristic of $\tilde{X}(\omega) = (\tilde{x}, \tilde{y})$ is not only its independence with respect to the time variable t, but also the fact that it exhibits hyperbolic behaviour with respect to its neighboring trajectories.

Considering the hyperbolicity of a given solution, as well as in the deterministic context, means considering the hyperbolicity of the RDS φ linearized over such solution. Specifically the Oseledets' multiplicative ergodic theorem for random dynamical systems [Arnold, 1998; Duan, 2015] ensures the existence of a Lyapunov spectrum which is necessary to determine whether the stationary orbit $\tilde{X}(\omega)$ is hyperbolic or not. All these issues are well reported in [Duan, 2015] and summarized in Appendix 3, including the proof that the noisy saddle (3.7) satisfies the Oseledets' multiplicative ergodic theorem conditions.

Chapter 4

The method of Lagrangian descriptors for SDEs

In this chapter the method of Lagrangian descriptors is extended to stochastic differential equations (SDEs). The resulting method provides a way of revealing the global phase space structure of SDEs that is analogous to the manner in which one can understand the global phase space structure of deterministic ordinary differential equations. In particular it is shown that stochastic versions of hyperbolic trajectories and their stable and unstable manifolds provide barriers to transport. This method is applied to the noisy saddle, the stochastically forced Duffing equation, and the stochastic double gyre model that is a benchmark for analyzing fluid transport. All these results are reported in [Balibrea-Iniesta *et al.*, 2016].

4.1 The original Lagrangian descriptor

The original Lagrangian descriptor, introduced in [Mancho *et al.*, 2013] for continuous dynamical systems, corresponds to the Euclidean arc length of a trajectory over a time interval (backwards and forwards). In particular a trajectory advected by any general time-dependent vector field

$$\frac{d\mathbf{x}}{dt} = \mathbf{v}(\mathbf{x}, t), \quad x \in \mathbb{R}^N, \quad t \in \mathbb{R}, \tag{4.1}$$

where $\mathbf{v}(\mathbf{x}, t) \in C^r (r \geq 1)$ in $\mathbf{x}$ and continuous in time. For any solution $\mathbf{x}(t) \equiv \mathbf{x}(\mathbf{x}_0, t, t_0)$ with initial condition $\mathbf{x}_0 \equiv \mathbf{x}(\mathbf{x}_0, t_0, t_0) \in \mathbb{R}^N$ and a fixed integration time τ, the Lagrangian descriptor was initially defined as

$$M(\mathbf{x}_0, t_0, \tau) = \int_{t_0-\tau}^{t_0+\tau} ||\dot{\mathbf{x}}(\mathbf{x}_0, t, t_0)||\, dt, \tag{4.2}$$

where $||\cdot||$ is the Euclidean norm. Afterwards in [Lopesino *et al.*, 2015a], the Lagrangian descriptor was adapted to the discrete dynamical systems setting

but including a small change in the chosen norm (p-norm). Let $\{x_i\}_{i=-n}^{i=n}$, $n \in \mathbb{N}$ denote an orbit of $(2n+1)$ nodes long and $x_i \in \mathbb{R}^N$. Considering the space of orbits as a sequence space, the discrete Lagrangian descriptor was defined in terms of the ℓ^p-norm of an orbit as follows:

$$MD_p(\mathbf{x}_0, n) = \sum_{i=-n}^{n-1} ||\mathbf{x}_{i+1} - \mathbf{x}_i||_p, \quad 0 < p \leq 1 \quad \text{where}$$

$$||\mathbf{x}_{i+1} - \mathbf{x}_i||_p = \sum_{j=1}^{N} \left| \mathbf{x}_{i+1}^j - \mathbf{x}_i^j \right|^p, \tag{4.3}$$

for points of the form $\mathbf{x}_i = (\mathbf{x}_i^1 \mathbf{x}_i^2 \cdots \mathbf{x}_i^n) \in \mathbb{R}^N$.

This alternative definition allows to formally prove the non-differentiability of the MD_p function at points that belong to invariant manifolds of a hyperbolic trajectory and along directions transversal to these manifolds. This definition allows a sharper visualization of the invariant manifolds by means of abrupt changes in the values taken by the function MD_p.

Later on this last definition was adapted to the continuous time case in [Lopesino *et al.*, 2017]. For any initial condition $\mathbf{x}_0 = \mathbf{x}(t_0) \in \mathbb{R}^N$ and any given time interval $[t_0 - \tau, t_0 + \tau]$, the M function is redefined as

$$M_p(\mathbf{x}_0, t_0, \tau) = \int_{t_0-\tau}^{t_0+\tau} ||\dot{\mathbf{x}}(\mathbf{x}_0, t, t_0)||_p \, dt, \tag{4.4}$$

where p is chosen from the interval $(0, 1]$.

In recent years Lagrangian descriptors have been shown to be a useful technique for discovering phase space structure in both autonomous and nonautonomous dynamical systems. In [Madrid & Mancho, 2009] Lagrangian descriptors (also referred to in the literature as the M function) were used to discover hyperbolic trajectories and their stable and unstable manifolds in aperiodically time-dependent vector fields. Particularly in this chapter, "important hyperbolic trajectories" are considered and referred to as distinguished trajectories, which build on the well-known idea of distinguished hyperbolic trajectory discussed earlier in [Ide *et al.*, 2002].

Lagrangian descriptors can easily be applied to the analysis of velocity fields defined as data sets. Early work demonstrating this was concerned with transport associated with the Kuroshio current, described in [Mendoza & Mancho, 2010, 2012]. This work set the stage for further geophysical transport studies described in [de la Cámara *et al.*, 2012, 2013], for instance. An application concerned with determining the connection between coherent

structures and the saturation of a nonlinear dynamo is described in [Rempel *et al.*, 2013]. In the last years Lagrangian descriptors have been used to analyze issues related to the search strategy for the Malaysian airliner MH370 [García-Garrido *et al.*, 2015] as well as to an understanding of events surrounding the Deepwater Horizon oil spill [Mendoza *et al.*, 2014] and more recently to an analysis of the real time development of an oil spill in the Canary Islands [García-Garrido *et al.*, 2016].

In [Mancho *et al.*, 2013] a general assessment of Lagrangian descriptors was carried out. Different Lagrangian descriptors were considered and applied to a variety of benchmark examples containing known phase space structures. While most of the previous applications of Lagrangian descriptors had been to two-dimensional time-dependent flows, it was also shown that dimensionality is not a restriction to the application of the method. In particular transport associated with the three dimensional time dependent Hill's spherical vortex was considered. The computational requirements of Lagrangian descriptors were also considered and compared with those of finite time Lyapunov exponents.

The applications of Lagrangian descriptors mentioned above are in areas of fluid mechanics. However the method of Lagrangian descriptors applies to general vector fields in n dimensions, and there is no obstacle to using Lagrangian descriptors for applications in a higher dimensional setting. Recently this has been illustrated by a series of applications of Lagrangian descriptors to problems in chemistry by Hernandez and co-workers. More concretely they applied Lagrangian descriptors to a study of chemical reactions under external time-dependent driving in [Craven & Hernandez, 2015], barrierless reactions in [Junginger & Hernandez, 2016a,b] and ketene isomerization in [Craven & Hernandez, 2016]. Furthermore the use of Lagrangian descriptors for visualizing phase space structures in complex dynamical systems is described in [Mancho *et al.*, 2015].

Next the development of the method of Lagrangian descriptors is carried out in the setting of stochastic differential equations. This provides a computational tool for revealing the phase space structure of stochastic dynamical systems. What this means is discussed in detail by considering explicit examples and comparing them with their deterministic counterparts.

4.2 Dynamical structures of SDEs

Before implementing the numerical method of Lagrangian descriptors to several examples of SDEs, it is important to remark why random fixed points and their respective stable and unstable manifolds govern the nearby trajec-

tories, and furthermore, how they may influence the dynamics throughout the rest of the domain. These are essential issues in order to describe the global phase space motion of solutions of SDEs. However these questions do not have a simple answer. For instance in the noisy saddle example (3.7) the geometrical structures arising from the dynamics generated around the stationary orbit are quite similar to the dynamics corresponding to the deterministic saddle point $\{\dot{x} = x, \dot{y} = -y\}$. Significantly the manifolds $\mathcal{S}(\omega)$ and $\mathcal{U}(\omega)$ of the noisy saddle form two dynamical barriers for other trajectories in the same way that the manifolds $\{x = 0\}$ and $\{y = 0\}$ of the deterministic saddle work. This means that for any particular experiment, i.e. for any given $\omega \in \Omega$, the manifolds $\mathcal{S}(\omega)$ and $\mathcal{U}(\omega)$ are determined and cannot be "crossed" by other trajectories due to the uniqueness of solutions (remember that the manifolds are invariant under the RDS (3.8) and are comprised of an infinite family of solutions). Also by considering the exponential separation rates reported in (3.14) with the rest of trajectories, the manifolds $\mathcal{S}(\omega)$ and $\mathcal{U}(\omega)$ divide the plane $\mathbb{R}^2$ of initial conditions into four qualitatively distinct dynamical regions, therefore providing a phase portrait representation.

Nevertheless it remains to show that such analogy can be found between other SDEs and their corresponding non-noisy deterministic differential equations[1]. In this direction there is a recent result (see [Cheng *et al.*, 2016], Theorem 2.1) which ensures the equivalence in the dynamics of both kinds of equations when the noisy term σ is additive (i.e., σ does not depend on the solution X_t). Although this was done by means of the *most probable phase portrait*, a technique that closely resembles the ordinary phase space for deterministic systems, this fact might indicate that such analogy in the dynamics cannot be achieved when the noise does depend explicitly on the solution X_t. Actually any additive noise affects all the particles together at the same magnitude.

Anyway the noisy saddle serves to establish an analogy to the dynamics with the deterministic saddle. One of its features is the contrast between the growth of the components X_t and Y_t, which mainly have a positive and negative exponential growth respectively. Actually this is graphically captured when applying the stochastic Lagrangian descriptors method to the SDE (3.7) over a domain of the stationary orbit. Moreover when represent-

[1] Otherwise if nonlinearity is dominating the behavior of the terms in equation (3.3) then the correspondence between the manifolds for $\Phi(t, \omega)$ to the manifolds for φ needs to be made by means of the local stable and unstable manifold theorem (see [Mohammed & Scheutzow, 1999], Theorem 3.1). Therein it is considered a homeomorphism $H(\omega)$ which establishes the equivalence of the geometrical structures arising for both sets of manifolds, and as a consequence the manifolds for φ inherit the same dynamics as the ones for $\Phi(t, \omega)$ but only in a neighborhood of the stationary orbit. In this sense the existence of such manifolds for a nonlinear RDS φ is only ensured locally. Anyway this result provides a very good approximation to the stochastic dynamics of a system, and enables to discuss the different patterns of behavior of the solutions in the following examples.

ing the stochastic Lagrangian descriptor values for the noisy saddle, one can observe that the lowest values are precisely located on the manifolds $\mathcal{S}(\omega)$ and $\mathcal{U}(\omega)$. These are manifested as sharp features indicating a rapid change of the values that the stochastic Lagrangian descriptor assumes. This geometrical structure formed by "local minimums" has a very marked crossed form and it is straightforward to think that the stationary orbit is located at the intersection of the two cross-sections. These statements are supported afterwards by numerical simulations and analytical results.

However there persists an open question about how reliable the stochastic Lagrangian descriptors method is when trying to depict the phase space of an arbitrary stochastic differential equation. This is the main issue concerning this method and has only been partially reported for deterministic dynamical systems in previous articles [Mancho *et al.*, 2015; Lopesino *et al.*, 2017]. In this last paper it is analytically proven the efficacy of this method for autonomous and non-autonomous Hamiltonian systems. The theoretical idea that supports this assertion is the discontinuity of the transversal derivative of the Lagrangian descriptor function over the manifolds of the corresponding hyperbolic trajectory. Following this idea, the "singular features" arising on the manifolds of a hyperbolic trajectory for a deterministic Hamiltonian system motivates to study whether the "abrupt changes" on the stochastic Lagrangian descriptor function represent the location of the manifolds of a stationary orbit or not. Another related question is to determine the size of the random term σdW in relation to its influence on the phase space of the deterministic equation $dX = bdt$. The next sections in this chapter will be dedicated to addressing these issues by considering concrete examples of SDEs.

4.3 The stochastic Lagrangian descriptor

Onwards in this chapter the ideas about Lagrangian descriptors exposed in Chapter 3 are extended to the context of stochastic differential equations. For this purpose it is considered a general SDE of the form

$$dX_t = b(X_t, t)dt + \sigma(X_t, t)dW_t, \quad X_{t_0} = x_0, \tag{4.5}$$

where X_t denotes the solution of the system, $b(\cdot)$ and $\sigma(\cdot)$ are Lipschitz functions which ensure uniqueness of solutions and W_t is a two-sided Wiener process. Henceforth it is used the following notation

$$X_{t_j} := X_{t_0+j\Delta t}, \tag{4.6}$$

for a given $\Delta t > 0$ small enough and $j = -n, \cdots, -1, 0, 1, \cdots, n$.

Definition 14. *The stochastic Lagrangian descriptor evaluated for SDE* (4.5) *with general solution* $\boldsymbol{X}_t(\omega)$ *is given by*

$$MS_p(\boldsymbol{x}_0, t_0, \tau, \omega) = \sum_{i=-n}^{n-1} \left|\left| \boldsymbol{X}_{t_{i+1}} - \boldsymbol{X}_{t_i} \right|\right|_p, \tag{4.7}$$

where $\{\boldsymbol{X}_{t_j}\}_{j=-n}^{n}$ *is a discretization of the solution such that* $\boldsymbol{X}_{t_{-n}} = \boldsymbol{X}_{-\tau}$, $\boldsymbol{X}_{t_n} = \boldsymbol{X}_{\tau}$, $\boldsymbol{X}_{t_0} = \boldsymbol{x}_0$, *for a given* $\omega \in \Omega$.

Obviously every output of the MS_p function (denoted onwards as SLD) highly depends on the experiment $\omega \in \Omega$ where Ω is the probability space that includes all the possible outcomes of a given phenomena. Therefore in order to analyze the homogeneity of a given set of outputs, consider a sequence of results of the MS_p function for the same stochastic equation (4.5): $MS_p(\cdot, \omega_1)$, $MS_p(\cdot, \omega_2)$, $\cdots$, $MS_p(\cdot, \omega_M)$. It is feasible that the following relation holds

$$d(MS_p(\cdot, \omega_i), MS_p(\cdot, \omega_j)) < \delta, \quad \text{for all } i, j, \tag{4.8}$$

where d is a metric that measures the similarity between two matrices (for instance $||A - B||_F = \sqrt{Tr((A-B)\cdot(A-B)^T)}$ - Frobenius norm) and δ a positive tolerance. Nevertheless for general stochastic differential equations, expression ((4.8)) does not usually hold. Alternatively if the elements of the sequence of matrices $MS_p(\cdot, \omega_1)$, $MS_p(\cdot, \omega_2)$, $\cdots$, $MS_p(\cdot, \omega_M)$ do not have much similarity to each other, it may be of more use to define the mean of the outputs

$$\mathbb{E}\left[MS_p(\cdot, \omega)\right] = \left(\frac{MS_p(\cdot, \omega_1) + MS_p(\cdot, \omega_2) + \cdots + MS_p(\cdot, \omega_M)}{M} \right), \tag{4.9}$$

for a sufficiently large number of experiments M. Since the solution of a SDE is affected by the noisy term, the phase portrait of the studied SDE for an arbitrary ω becomes unpredictable and one can only refer to places where hyperbolic trajectories and invariant manifolds are likely located. This way of understanding the geometry of transport for SDEs is similar in spirit as the one explained in [Banisch & Koltai, 2017] where the authors provide an alternative method for revealing coherent sets from Lagrangian trajectory data.

4.4 Numerical simulation of the SLD function

In this section it is described the method numerically solving the SDEs used throughout this chapter. Consider a general N-dimensional SDE of the form

$$dX_t^j = b^j(X_t,t)dt + \sum_{k=1}^{M} \sigma_k^j(X_t,t)dW_t^k, \;\; X_{t_0} = x_0 \in \mathbb{R}^N, \;\; j = 1, \cdots, N \tag{4.10}$$

where $X_t = (X_t^1, \cdots, X_t^N)$ and $W_t^1, \cdots, W_t^M$ are $M \in \mathbb{N}$ independent Wiener processes. If the time step Δt is firstly fixed then the temporal grid $t_p = t_0 + p\Delta t$ ($p \in \mathbb{Z}$) is already determined and this leads to the difference equation

$$X_{t+\Delta t}^j = X_t^j + b^j(X_t,t)\Delta t + \sum_{k=1}^{m} \sigma_k^j(X_t,t)dW_t^k. \tag{4.11}$$

This scheme is referred to as the Euler-Marayuma method for solving a single path of the SDE. If the stochastic part is removed from the equation, then the method is reduced to the classical Euler method. Suppose X_{t_p} is the solution of the SDE and $\tilde{X}_{t_p}$ its numerical approximation at any time t_p. Since both of them are random variables, the accuracy of the method must be determined in probabilistic terms. With this aim the following definition is introduced.

Definition 15. *A stochastic numerical method has an order of convergence equal to γ if there exists a constant $C > 0$ such that*

$$\mathbb{E}\left[X_{t_p} - \tilde{X}_{t_p}\right] \leq C\Delta t^{\gamma}, \tag{4.12}$$

for any arbitrary $t_p = t_0 + p\Delta t$ and Δt small enough.

Indeed, the Euler-Maruyama method has an order of convergence equal to 1/2 (see [Kloeden & Platen, 1992] for further details).

4.5 The noisy saddle

The noisy saddle is a fundamental benchmark for assessing numerical methods for revealing phase space structures. Its main advantage is the simplicity of the expressions taken by the components of the stationary orbit and its corresponding stable and unstable manifolds. From these one clearly observes the exponential separation rates between particles passing near the manifolds. Now for the stochastic differential equations

$$\begin{cases} dX_t = a_1 X_t dt + b_1 dW_t^1 \\ dY_t = -a_2 Y_t dt + b_2 dW_t^2 \end{cases} \tag{4.13}$$

it is straightforward to check that the only stationary orbit takes the expression

$$\widetilde{X}(\omega) = (\tilde{x}(\omega), \tilde{y}(\omega)) = \left(-\int_0^{\infty} e^{-a_1 s} b_1 dW_t^1(\omega), \int_{-\infty}^{0} e^{b_1 s} b_2 dW_t^2(\omega) \right), \tag{4.14}$$

where $a_1, a_2, b_1, b_2 \in \mathbb{R}$ are constants with $a_1, a_2 > 0$. Its corresponding stable and unstable manifolds are

$$\mathcal{S}(\omega) = \{(x, y) \in \mathbb{R}^2 : x = \tilde{x}(\omega)\}, \quad \mathcal{U}(\omega) = \{(x, y) \in \mathbb{R}^2 : y = \tilde{y}(\omega)\}. \tag{4.15}$$

These play a very relevant role as dynamical barriers for the particles tracked by the RDS, which comes generated by the SDE (4.13). This fact has been justified in the previous section, but can be analytically demonstrated when computing the stochastic Lagrangian descriptor (4.7) for the solution of the noisy saddle.

According to the notation used for the definition of SLD in (4.7),

$$MS_p(\mathbf{x}_0, t_0, \tau, \omega) = \sum_{i=-N}^{N-1} \left|\left|\mathbf{X}_{t_{i+1}} - \mathbf{X}_{t_i}\right|\right|_p,$$

at which the components of the solution satisfy the initial conditions $\mathbf{X}_{t_0} = (X_{t_0}, Y_{t_0}) = (x_0, y_0) = \mathbf{x}_0$, these take the expressions

$$X_t = e^{a_1 t} \left(x_0 + \int_0^t e^{-a_1 s} b_1 dW_s^1 \right), \quad Y_t = e^{-a_2 t} \left(y_0 + \int_0^t e^{a_2 s} b_2 dW_s^2(\omega) \right) \tag{4.16}$$

and the temporal nodes satisfy the rule $t_i = t_0 + i\Delta t$ with t_0 and Δt already given. Now it is possible to compute analytically the increments $\left|\left|\mathbf{X}_{t_{i+1}} - \mathbf{X}_{t_i}\right|\right|_p = \left|X_{t_{i+1}} - X_{t_i}\right|^p + \left|Y_{t_{i+1}} - Y_{t_i}\right|^p$ also by applying Itô's formula (3.5):

$$\begin{aligned}
&\left|X_{t_{i+1}} - X_{t_i}\right|^p \\
&= \left| e^{a_1 t_{i+1}} \left(x_0 + \int_0^{t_{i+1}} e^{-a_1 s} b_1 dW_s^1 \right) - e^{a_1 t_i} \left(x_0 + \int_0^{t_i} e^{-a_1 s} b_1 dW_s^1 \right) \right|^p \\
&= \left| e^{a_1 t_i} \left(e^{a_1 \Delta t} - 1 \right) \left[x_0 + \int_0^{t_i} e^{-a_1 s} b_1 dW_s^1 \right] + e^{a_1 (t_i + \Delta t)} \int_{t_i}^{t_i + \Delta t} e^{-a_1 s} b_1 dW_s^1 \right|^p \\
&= \left| e^{a_1 t_i} \left(e^{a_1 \Delta t} - 1 \right) \left[x_0 + \int_0^{t_i} e^{-a_1 s} b_1 dW_s^1 \right] + e^{a_1 \Delta t} b_1 dW_{t_i}^1 \right|^p.
\end{aligned}$$

Moreover for large values of t_i such that $e^{a_1 t_i} \gg e^{a_1 \Delta t}$ and taking into account that $dW_{t_i}^1$ is finite almost surely, the following approximation can be

considered

$$\left|X_{t_{i+1}} - X_{t_i}\right|^p \approx e^{a_1 t_i \cdot p} \left|e^{a_1 \Delta t} - 1\right|^p \left|x_0 + \int_0^{t_i} e^{-a_1 s} b_1 dW_s^1\right|^p . \tag{4.17}$$

By following these arguments, one can get an analogous result for the second component Y_t

$$\left|Y_{t_{i+1}} - Y_{t_i}\right|^p = \left|e^{-a_2 t_i}\left(e^{-a_2 \Delta t} - 1\right)\left[y_0 + \int_0^{t_i} e^{a_2 s} b_2 dW_s^2\right] + e^{-a_2 \Delta t} b_2 dW_{t_i}^2\right|^p ,$$

which for small values of t_i such that $e^{-a_2 t_i} \gg e^{-a_2 \Delta t}$, this approximation can be further simplified as follows

$$\left|Y_{t_{i+1}} - Y_{t_i}\right|^p \approx e^{-a_2 t_i \cdot p} \left|e^{-a_2 \Delta t} - 1\right|^p \left|y_0 + \int_0^{t_i} e^{a_2 s} b_2 dW_s^2\right|^p . \tag{4.18}$$

Once the analytic expression of the SLD applied to the noisy saddle (4.13) is known, it can be proved that the stable and unstable manifolds of the stationary orbit are manifested as singularities of the SLD function over any given domain of initial conditions containing the stationary orbit. This fact implies that the SLD method realizes a procedure to detect these geometrical objects and, consequently, provides a phase portrait representation of the dynamics generated by the noisy saddle. In the same way as described in [Lopesino *et al.*, 2017], singularities are referred to as points of the domain of spatial initial conditions where the derivative of the SLD is not defined. The paradigm example of the mathematical manifestation of singularities of the LD on stable and unstable manifolds of hyperbolic trajectories is provided by the scalar function $|\cdot|^p$ with $p \in (0, 1]$. This function is singular, alternatively non-differentiable, at those points where their argument is zero. Graphically this feature is detected as a set of sharp changes in the representation of the SLD values, where the contour lines concentrate in a very narrow space.

In this particular example one can explicitly identify within the expression of the SLD the terms that are largest in magnitude. In other words, it was possible to identify the terms whose particular singularities determine the non-differentiability of the entire sum[2]. This is better understandable if the expression of the SLD is divided into two sums

$$MS_p(\mathbf{x}_0, t_0, \tau, \omega) = \sum_{i=-n}^{n-1} \left|\left|\mathbf{X}_{t_{i+1}} - \mathbf{X}_{t_i}\right|\right|_p$$

[2]Note that the differentiability of the SLD is analyzed with respect to the components of the initial conditions (x_0, y_0), as the experiment $\omega \in \Omega$ and the starting point t_0 are previously fixed.

$$= \sum_{i=-n}^{n-1} \left|X_{t_{i+1}} - X_{t_i}\right|^p + \sum_{i=-n}^{n-1} \left|Y_{t_{i+1}} - Y_{t_i}\right|^p .$$

The highest order term within the first sum is $\left|X_{t_n} - X_{t_{n-1}}\right|^p = |X_\tau - X_{\tau-\Delta t}|^p$, which according to (4.17) is approximated by

$$|X_\tau - X_{\tau-\Delta t}|^p \;\approx\; e^{a_1(\tau-\Delta t)\cdot p} \left|e^{a_1\Delta t} - 1\right|^p \left|x_0 + \int_0^{\tau-\Delta t} e^{-a_1 s} b_1 dW_s^1\right|^p \tag{4.19}$$

for enough large values of τ.

Similarly the highest order term within the second sum is $\left|Y_{t_{-n+1}} - Y_{t_{-n}}\right|^p = |Y_{-\tau+\Delta t} - Y_{-\tau}|^p$, approximated by

$$|Y_{-\tau+\Delta t} - Y_{-\tau}|^p \;\approx\; e^{a_2\tau\cdot p} \left|e^{-a_2\Delta t} - 1\right|^p \left|y_0 - \int_{-\tau}^{0} e^{a_2 s} b_2 dW_s^2\right|^p \tag{4.20}$$

for enough large values of τ.

Consequently it results evident that the sharper features will be located closed to the points where these two last quantities (4.19), (4.20) are zero. In other words where the initial condition (x_0, y_0) satisfies one of the two following

$$x_0 = -\int_0^{\tau-\Delta t} e^{-a_1 s} b_1 dW_s^1 \quad \text{or} \quad y_0 = \int_{-\tau}^{0} e^{a_2 s} b_2 dW_s^2$$

for enough large values of τ.

This statement is in agreement with the distinguished nature of the manifolds of the stationary orbit discussed in the previous section. Note also that the two quantities for x_0 and y_0 converge to the coordinates of the stationary orbit $(\tilde{x}(\omega), \tilde{y}(\omega))$ with τ tending to infinity. These features are observed in Figure 4.1, where the sharpness of the SLD representation highlights the location of the stable and unstable manifolds. The intersection of the two "singular" curves represents the position of the stationary orbit $(\tilde{x}(\omega), \tilde{y}(\omega))$ for a given $\omega \in \Omega$. This fact is validated by the depiction of the stationary orbit, whose components have been computed separately from the SLD by using the same output of the Wiener process.

Remark 3. Due to the properties of Itô integrals, see for instance [Duan, 2015], the components of the stationary orbit satisfy

$$\mathbb{E}\left[\tilde{x}(\omega)\right] = \mathbb{E}\left[-\int_0^{\infty} e^{-s} dW_s^1\right] = 0, \quad \mathbb{E}\left[\tilde{y}(\omega)\right] = \mathbb{E}\left[\int_{-\infty}^{0} e^{s} dW_s^2\right] = 0,$$

$$\mathbb{V}\left[\tilde{x}(\omega)\right] = \mathbb{E}\left[\tilde{x}(\omega)^2\right] = \mathbb{E}\left[\int_0^\infty e^{-2s} ds\right] = \frac{1}{2},$$
$$\mathbb{V}\left[\tilde{y}(\omega)\right] = \mathbb{E}\left[\tilde{y}(\omega)^2\right] = \mathbb{E}\left[\int_{-\infty}^0 e^{2s} ds\right] = \frac{1}{2}.$$

This means that the stationary orbit $(\tilde{x}(\omega), \tilde{y}(\omega))$ is highly probable to be located closed to the origin of coordinates $(0, 0)$, and this feature is displayed in Figure 4.1. This result gives more evidences and supports the similarities between the stochastic differential equation (3.7) and the deterministic analogue system $\{\dot{x} = x,\ \dot{y} = -y\}$ whose only fixed point is $(0, 0)$. □

Therefore one can assert that the stochastic Lagrangian descriptor is a technique that provides a phase portrait representation of the dynamics generated by the noisy saddle equation (4.13). In next section this same technique is applied to further examples.

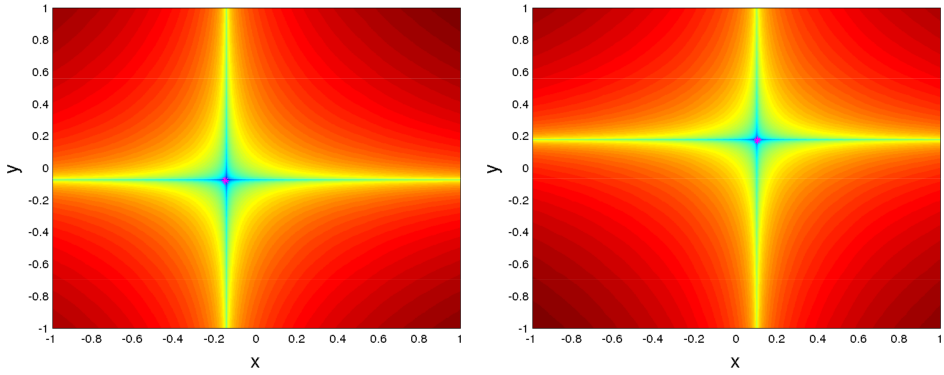

Figure 4.1: Two different experiments representing contours of MS_p for $p = 0.1$ and $\tau = 15$. The contours of MS_p are computed on a 1200×1200 points grid of initial conditions and the time step for integration of the vector field is chosen to be $\Delta t = 0.05$. The magenta colored point corresponds to the location of the stationary orbit for each experiment. The chosen parameters are $a_1 = a_2 = b_2 = 1$ and $b_1 = -1$.

4.6 Stochastically forced Duffing equation

Another classical problem is the Duffing oscillator. Its deterministic version is given by

$$\ddot{x} = \alpha\dot{x} + \beta x + \gamma x^3 + \epsilon\cos(t). \tag{4.21}$$

If $\epsilon = 0$ the Duffing equation becomes time-independent, meanwhile for $\epsilon \neq 0$

the oscillator is a time-dependent system where α is the damping parameter, β controls the rigidity of the system and γ controls the size of the nonlinearity of the restoring force.

The stochastically forced Duffing equation is studied in [Datta & Bhattacharjee, 2001] and can be written as follows

$$\begin{cases} dX_t = \alpha Y_t, \\ dY_t = (\beta X_t + \gamma X_t^3)dt + \epsilon dW_t. \end{cases} \tag{4.22}$$

For the numerical experiments the parameters were selected as $\alpha = \beta = 1$, $\gamma = -1$ and $\epsilon = 0.25$. The results of three different experiments (let say three different samples of $\omega_1, \omega_2, \omega_3 \in \Omega$) are shown in Figure 4.2.

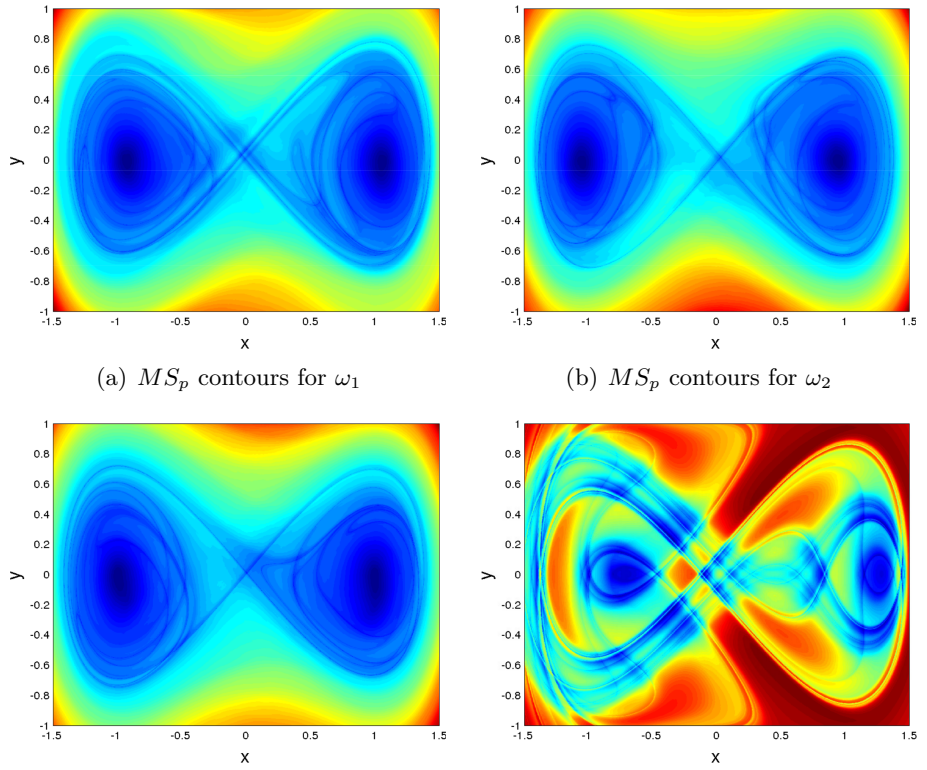

(a) MS_p contours for ω_1

(b) MS_p contours for ω_2

(c) MS_p contours for ω_3

(d) M_p for equation (4.21)

Figure 4.2: a), b), c) Three different experiments representing MS_p contours for $p = 0.5$ over a grid of initial conditions. d) The last image corresponds to the M_p function for equation (4.21) and $p = 0.75$. All these pictures were computed for $\tau = 15$, and over a 1200×1200 points grid. The time step for integration of the vector field was chosen to be $\Delta t = 0.05$.

4.7 Stochastically forced Double Gyre

The double gyre is a standard benchmark velocity field in the study of the dynamical systems approach to Lagrangian transport. Recently it has been studied in the situation where the time-dependence is stochastic [Hsieh *et al.*, 2012]. These equations are given by

$$\begin{cases} dX_t = \left(-\pi A \sin\left(\pi \dfrac{f(X_t,t)}{s}\right) \cos\left(\pi \dfrac{Y_t}{s}\right) - \mu X_t\right) dt + \alpha dW_t^1, \\ dY_t = \left(\pi A \cos\left(\pi \dfrac{f(X_t,t)}{s}\right) \sin\left(\pi \dfrac{Y_t}{s}\right) \dfrac{\partial f}{\partial X_t} - \mu Y_t\right) dt + \alpha dW_t^2, \end{cases} \tag{4.23}$$

where

$$f(X_t,t) = \epsilon \sin(\phi t + \psi) X_t^2 + (1 - 2\epsilon \sin(\phi t + \psi)) X_t. \tag{4.24}$$

When $\epsilon = 0$ the double-gyre is time-independent, meanwhile if $\epsilon \neq 0$ the gyres force a periodic behavior in the x direction. Among the parameters within the equation, A models the amplitude of the velocity vectors, $\frac{\phi}{2\pi}$ gives the oscillation frequency, ψ is the phase, μ determines the dissipation, s scales the dimensions of the grid and dW_t^i describes a Wiener process (stochastic white noise) with mean zero and standard deviation $\sigma = \Delta t$, while α is the amplitude of the noise. The results of two different experiments are observed in Figure 4.3. For such experiments the following values for the parameters were used: $A = 0.25$, $\phi = 2\pi$, $\psi = 0$, $\mu = 0$, $s = 1$, $\alpha = 0.1$, $\epsilon = 0.25$.

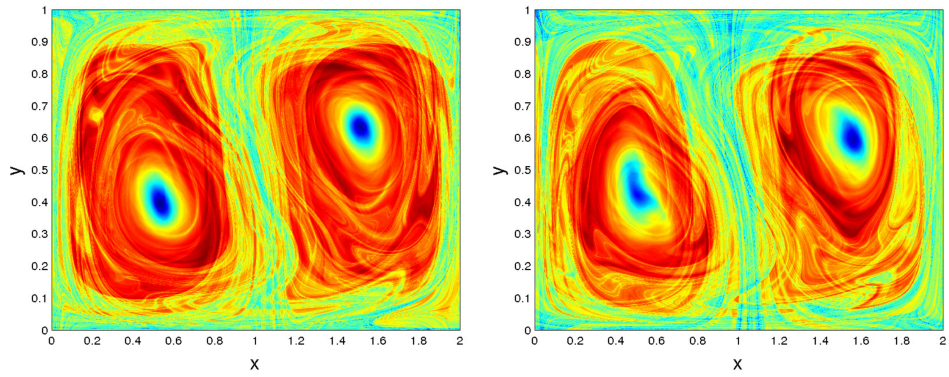

Figure 4.3: Two different experiments representing contours of MS_p for $p = 0.5$ and $\tau = 15$. The contours of MS_p are computed on a 1200×1200 points grid of initial conditions and the time step for integration of the vector field is chosen to be $\Delta t = 0.05$.

The outputs are quite different between these two experiments. Therefore it

is used the mean expression (4.9). In Figure 4.4 one can observe the values of $\mathbb{E}[MSp]$ when considering 30 different experiments. This is the expected phase space structure: two gyre centers are detected near the points $(0.5, 0.5)$ and $(1.5, 0.5)$ in dark blue, while around the line $\{x = 1\}$ bundles of invariant manifolds are detected in light blue. Thus for almost every $\omega \in \Omega$ two centers are depicted close to the middle of each gyre and by separating each gyre, the invariant manifolds can be interpreted as transport barriers.

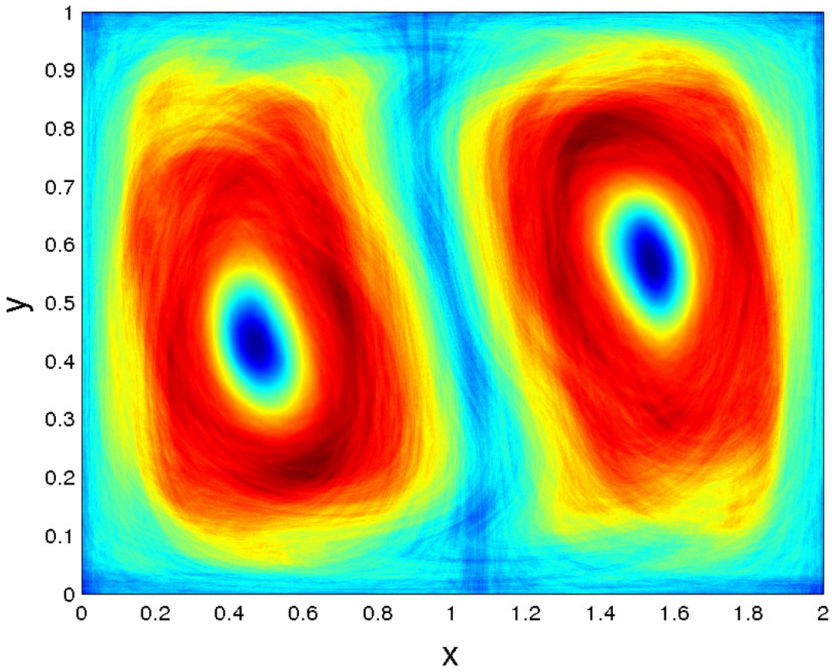

Figure 4.4: Computation of $\mathbb{E}[MS_p(\cdot, \omega)]$ for $p = 0.5$, $\tau = 15$ and 30 different experiments with a time step integration $\Delta t = 0.05$.

In order to clarify the structures highlighted in Figure 4.4, the location of a particle is selected in the middle of the gyre, the point $(0.5, 0.425)$, and evolved forwards and backwards in time for different realizations of the random variable ω. In Figure 4.5 there are represented different snapshots for several units of time. As the random dynamical system evolves, the different trajectories starting at the point $(0.5, 0.425)$ remain bounded inside the gyre. Only when the system evolves for a enough period of time, it is observable that hyperbolicity affects most of the trajectories.

Furthermore in order to verify the shape that the invariant manifolds take, the point $(1, 0.5)$ is evolved forward and backward in time for different realizations of the random variable ω. In Figure 4.6 5000 different trajectories are

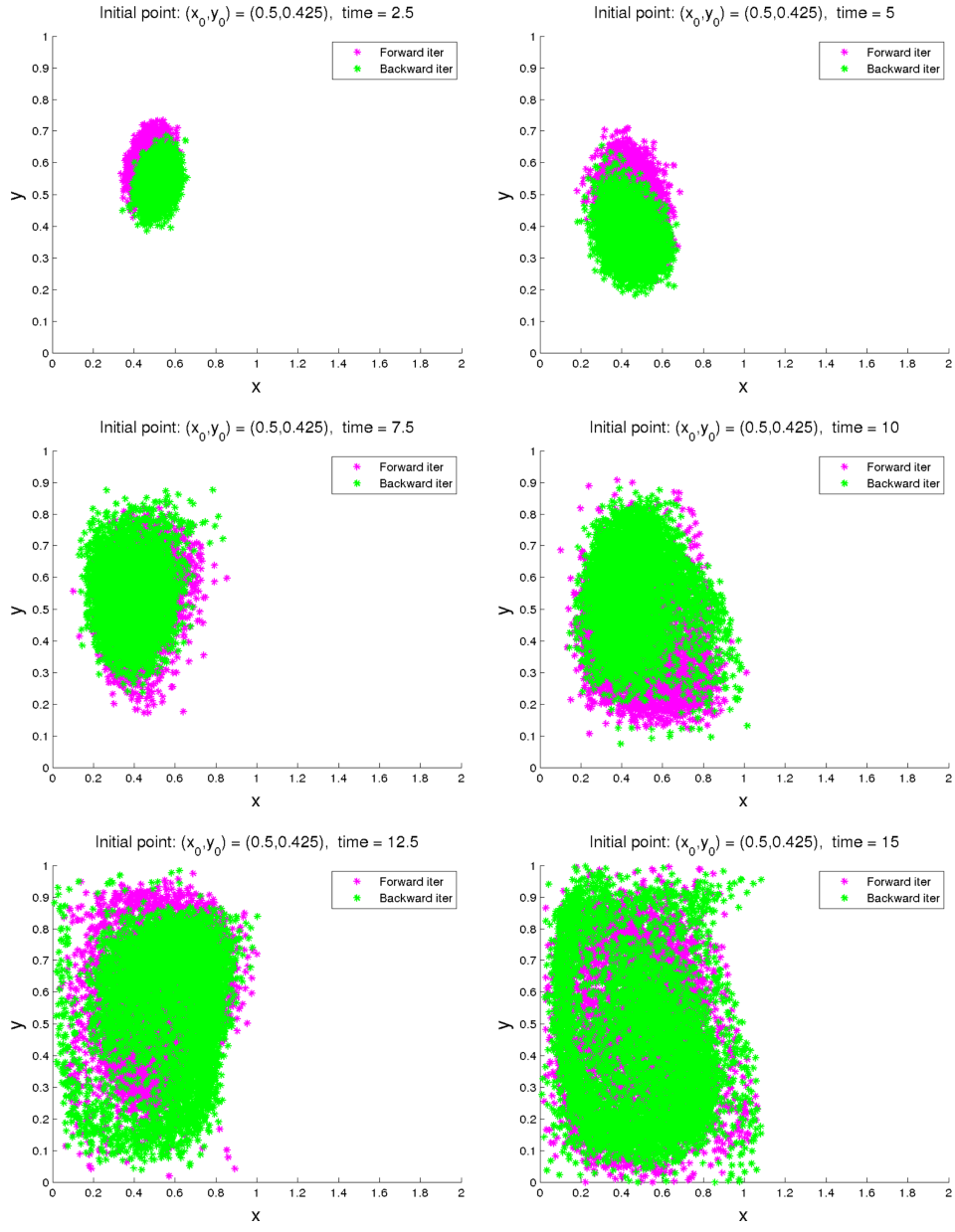

Figure 4.5: 5000 distinct simulations of trajectories starting at the point $(0.5, 0.425)$ and performed forwards and backwards for several intervals of time.

overlapped, all of them starting at the same point with the expected phase space shown in the background. Here it is examined how these trajectories fit the sharp lines corresponding to the already computed invariant manifolds.

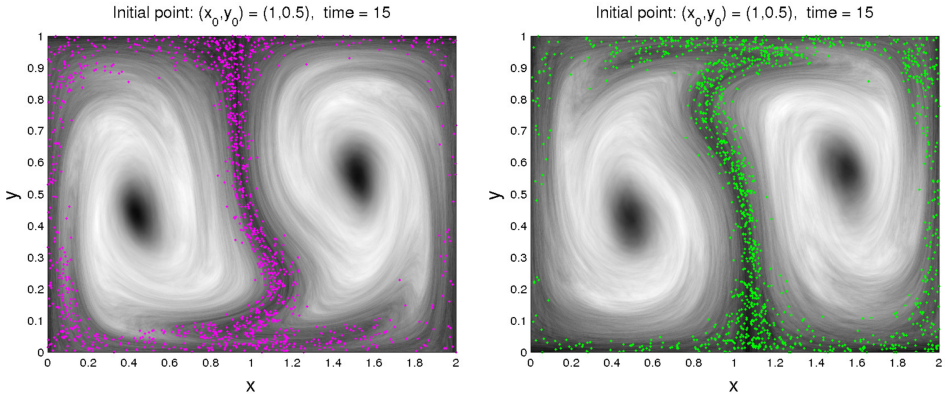

Figure 4.6: Representation of the ending points of 5000 distinct trajectories iterated in forward time from $t = 0$ until $t = 15$ (left hand panel, in magenta dots) and the ending points of 5000 distinct trajectories iterated in backward time from $t = 0$ until $t = -15$ (right hand panel, in green dots). All these trajectories start at the same initial point $(x_0, y_0) = (1, 0.5)$ but their respective evolutions are influenced by different Wiener processes. In addition, $\mathbb{E}[MS_p(\cdot, \omega)]$ is computed for the time periods $[-\tau, 0]$ and $[0, \tau]$. These expected phase spaces are depicted in the background of the left and right hand panels respectively with $p = 0.5$ for 30 different experiments.

These pictures provide evidence for the strong correspondance between the paths followed by the particles and the structures depicted in bluish colours in Figure 4.4. Notice that in this last Figure 4.6, the mean $\mathbb{E}[MS_p(\cdot, \omega)]$ computed for the time period $[-\tau, \tau]$ and represented in Figure 4.4 has been split into two quantities. From the deterministic Lagrangian descriptors setting (see [Lopesino *et al.*, 2017]), the trajectories iterated in forward time and starting in a neighborhood of a hyperbolic point approximate the location of the unstable manifold for a large integration time τ. Similarly, the trajectories iterated in backward time follow the path of the stable manifold in a neighborhood of the hyperbolic point. In summary, these simulations support the idea of the method of stochastic Lagrangian descriptors as useful for depicting areas where the hyperbolic trajectories with their stable and unstable manifolds are likely located.

Chapter 5

Transport processes in the Arctic Ocean

In this chapter the method of Lagrangian descriptors, based on the original function M described in [Mendoza & Mancho, 2010; Mancho *et al.*, 2013], is applied to velocity field datasets of water currents in the Arctic Ocean. This work provides a description of the Lagrangian circulation within the halocline (concretely at 30 metres depth) of the Arctic Ocean and studies the implications in the freshwater distribution within this layer. It is explained how these structures articulate fluid transport over two relevent Arctic features: the Beaufort Gyre (BG) and the Transpolar Drift Stream (TDS). The results described in this chapter are reported in [Balibrea-Iniesta *et al.*, 2017].

5.1 Overview

The Arctic Ocean is one of the regions most sensitive to climate change. This phenomenon, known as "Arctic amplification" [Cohen *et al.*, 2014], is manifested by dramatic changes of the Arctic sea ice cover, including the reduction of ice extent and the thinning of the ice [Krishfield *et al.*, 2014]. The enhanced melting of sea ice contributes to the freshening of the surface Arctic waters [Morison *et al.*, 2012], together with an intensification of the hydrological cycle. The largest freshwater storage in the Arctic Ocean resides in the Beaufort Gyre, an anticyclonic gyre in the Canada Basin [Aagaard & Carmack, 1989]. Several studies of the circulation of Arctic water masses [Jones, 2001; Tomczak & Godfrey, 1994] suggest that in recent years the qualitative circulation patterns may not have undergone significant variations, except for the strengthening of the Beaufort Gyre [Wood *et al.*, 2013].

In this chapter the ocean circulation patterns are explored as revealed by a regional model reanalysis [Xie *et al.*, 2017]. Those from March 2013 to March 2015 are examined by means of Lagrangian techniques and the dynamical

barriers responsible for the freshwater storage in the Canada Basin are identified. Arctic currents present distinctive characteristics to those found in other oceans, since typical velocities are much slower and particles may take from months to years to navigate significant distances. Although transport timescales in the Arctic are thus longer than in other areas, similar questions arise in the qualitative and quantitative description of fluid transport and horizontal mixing issues. For example, even in apparently simple velocity fields, nearby particles can evolve following completely different paths (i.e. the ocean currents are subject to chaotic dynamics and are thus sensitive to the initial conditions of fluid parcels).

This difficulty is addressed by means of the "dynamical systems approach" to Lagrangian transport. As mentioned in the Introduction, this paradigm seeks to discover geometrical flow structures that divide the ocean (phase space) into distinct regions corresponding to trajectories with qualitatively different dynamical behaviors. These distinguished material fluid structures are relevant because they act as transport barriers that fluid particles cannot cross, becoming the principal agents that mediate transport and mixing processes between different flow regions. In this way, they govern the evolution of biogeochemical tracers such as heat, salt and carbon dioxide and also potential contaminants produced by human exploitation of Arctic resources.

All these elements play a key role in the present and future of the Arctic Ocean ecosystem. In particular the Lagrangian technique used in this chapter identifies well the Transpolar Drift and revisits the paradigm of the Beaufort Gyre, which is reformulated in terms of dynamical systems concepts such as invariant manifolds. One finds that these mathematical structures are indeed present in the Arctic Ocean, and confirms that they play a key role in governing clockwise transport in the Beaufort Sea.

5.2 Datasets and dynamical systems tools

5.2.1 The CMEMS dataset

In order to describe the Arctic Ocean circulation patterns, we use the velocity and salinity fields distributed by the Copernicus Marine Environment Monitoring System (CMEMS) into a product called "Arctic Ocean Physics Analysis and Forecast", available at *http://marine.copernicus.eu/*. It is based on the TOPAZ4 ice-ocean prediction system, an operational real-time ocean monitoring and forecasting system covering the North Atlantic and Arctic Oceans with a resolution of 12.5 km [Sakov *et al.*, 2012; Melsom *et al.*, 2017]. TOPAZ4 is based on the HYbrid Coordinate Ocean Model (HYCOM, [Bleck, 2002]), using the K-Profile Parameter (KPP, [Large *et al.*, 1994]) and coupled

to a sea ice model with an Elastic-Visco-Plastic rheology [Hunke & Dukowicz, 1997] and simple themodynamics. TOPAZ4 uses the Ensemble Kalman Filter with 100 dynamical members for assimilating different ocean and sea ice observations. Moreover the TOPAZ4 production cycle is run on a weekly basis, starting with a data assimilation step, followed by a one-week simulation run producing a best estimate for the past week. Finally a 10-day ensemble forecast is run daily using the most recent analysis and a reduced ensemble of 10 members, forced by updated and perturbed atmospheric fields. The resulting ensemble mean forecast is delivered to the users and used also for validation [Melsom *et al.*, 2017].

The velocity and salinity data are provided from March 2013 to March 2015 as daily averages over 12 depth levels, varying from 5 m to 3000 m. At each vertical level, the fields have a horizontal spatial resolution of 12.5 km (a grid of 881×609 geophysical points expressed in polar stereographic projection coordinates (x, y)) covering the North Atlantic, the Arctic Ocean and other adjacent seas. The use of this projection is convenient to bypass the singularity that arises when working with longitude/latitude coordinates (λ, ϕ) at the North Pole ($\phi = \frac{\pi}{2}$), as becomes apparent from the transformation equations

$$\begin{cases} \dfrac{d\lambda}{dt} &= \dfrac{u(\lambda, \phi, t)}{R \cos \phi} \\ \dfrac{d\phi}{dt} &= \dfrac{v(\lambda, \phi, t)}{R} \end{cases}, \tag{5.1}$$

where u and v are, respectively, the zonal and meridional velocity components and R the Earth radius.

5.2.2 The Dynamical Systems Approach

In order to understand transport and mixing processes and the circulation patterns across the Arctic Ocean within the halocline level (30 m depth), we examine particle evolutions using a purely advective approach. Particle motion is assumed to be approximately quasi-horizontal within this layer, and thus motions are restricted to a 2D plane. Under these assumptions, fluid particles follow trajectories $\mathbf{x}(t) = (x(t), y(t))$ that evolve according to the dynamical system

$$\frac{d\mathbf{x}}{dt} = \mathbf{v}(\mathbf{x}(t), t), \tag{5.2}$$

where $\mathbf{v} = (v_x, v_y)$ are the ocean velocity components along the (x, y) polar stereographic projection coordinates (projection parameters given in the metadata). The results discussed later in this chapter require the integration of particle trajectories in Eq. (5.2), where the velocity field $\mathbf{v}$ is provided on a discrete grid. In order to obtain a continuous description, the velocity field is interpolated with a cubic scheme both in space in time, and after

the integration of particle trajectories is performed by means of a Cash-Karp Runge-Kutta scheme with a fixed integration time step.

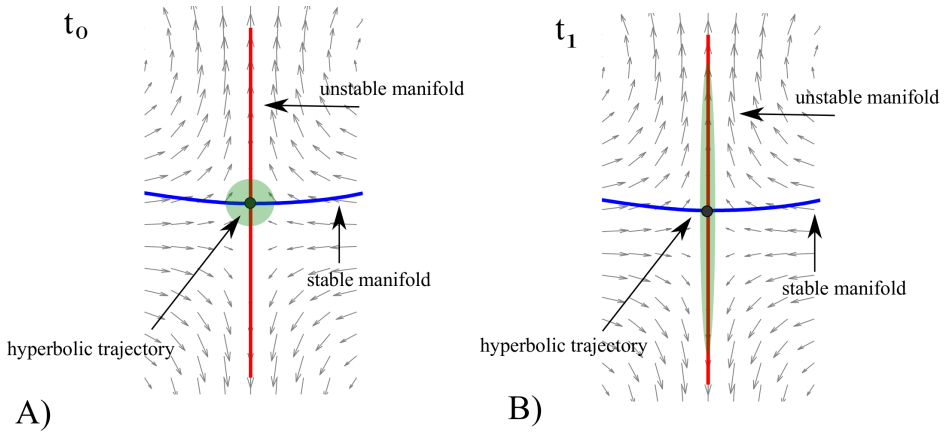

Figure 5.1: Evolution of a blob of particles in the neighbourhood of a hyperbolic trajectory at two distinct instants of time $t = t_0, t_1$ for which $t_0 < t_1$.

Among the geometrical features that divide the ocean surface into sectors with qualitatively different dynamical behaviors, of particular interest are hyperbolic trajectories (introduced in Chapter 1), which highlight regions in the fluid characterized by high expansion and contraction rates. Figure 5.1 illustrates how blobs in the neighbourhood of these trajectories evolve, contracting along the so-called stable direction (stable manifold) and stretching along the unstable direction (unstable manifold). Thus particles in the stable and unstable directions of the hyperbolic trajectory evolve, respectively, by approaching or moving away from the hyperbolic trajectory. If the time interval between t_0 and t_1 in Fig. 5.1 is long enough, the blob particles align along a (possibly complex) curve, the unstable manifold, which is an attracting material curve: advected particles remain close to it for a sufficiently long time. In a similar way but going backwards in time, blob particles align along a repelling material curve: the stable manifold.

Apart from hyperbolic trajectories other types of dynamical flow structures exist, in which particles tend to stay together, coherently without dispersing. In 2D flows these include eddies or jets, which act as dynamical barriers that trap fluid in their interiors ([Mancho *et al.*, 2006; Samelson & Wiggins, 2006]). Figure 5.2 shows the evolution of blobs in this type of flow. Vortices keep fluid parcels inside them and jets transport them with small distortion. Eventually all possible complex particle evolutions in time dependent 2D flows, such as the ocean, are then a result of transitions between these elementary features (vortices, jets and hyperbolic trajectories and their stable

and unstable manifolds) and their nonlinear interactions. The three aforementioned features cover exhaustively all possibilities in 2-dimensional flows.

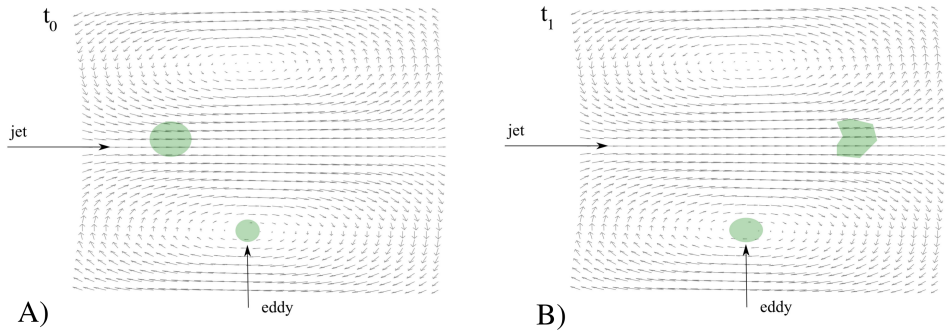

Figure 5.2: Evolution of a blob in the interior of a vortex and within a jet.

Several Lagrangian methods have been developed in the literature to reveal a geometrical template from time dependent velocity fields, a template formed by the stable and unstable manifolds of hyperbolic trajectories and other coherent structures in flows with aperiodic time dependence, as mentioned in the Introduction. Here the technique used for such target is the method of Lagrangian descriptors (LDs), in particular those depicted by function M [Mendoza & Mancho, 2010; Mancho *et al.*, 2013] (already introduced in Eq. 4.2) defined as follows

$$M(\mathbf{x}_0, t_0, \tau) = \int_{t_0-\tau}^{t_0+\tau} ||\mathbf{v}(\mathbf{x}(t), t)||\, dt\ , \tag{5.3}$$

where $||\cdot||$ represents the Euclidean norm. At a given time t_0, function M measures the arclength of a particle trajectory starting from $\mathbf{x}(t_0) = \mathbf{x}_0$ as it evolves forwards and backwards in time for a period $\tau > 0$. In order to evaluate M we are firstly required to solve Eq. 5.2 to finally compute the particle trajectories. At the performing of such computations, given an initial time t_0, a value for τ and also a grid of initial conditions $\mathbf{x}_0$ over the region of interest are chosen. This computation process is detailed in Appendix 4.

Large values of M are related to fluid regions of highest speed (such as jets), while small values of M denote calmer regions. This function, if evaluated for a sufficiently large τ, develops singular features aligned with invariant stable and unstable manifolds. Since the Arctic currents are generally slow, the integration period τ must be long to reveal these structures. For instance Fig. 5.3 displays the evaluation of M between the 1st April and 1st July 2013 over the Beaufort Sea by using $\tau = 300$ days. In Fig. 5.3 a) the yellow and red curves are aligned with the stable and unstable manifolds respectively,

which intersect at hyperbolic points. Four illustrative blobs are placed over the singular features aligned with manifolds. The evolution of both blobs and the manifolds is shown for the 1st May, 1st June and 1st of July 2013 in Figs. 5.3 b), c) and d) respectively, therefore confirming the hyperbolic character of the crossing lines as the blobs stretch and contract along the unstable and stable manifolds. The fact that particles remain on the sharp boundaries of the pattern confirms the invariant character of these features.

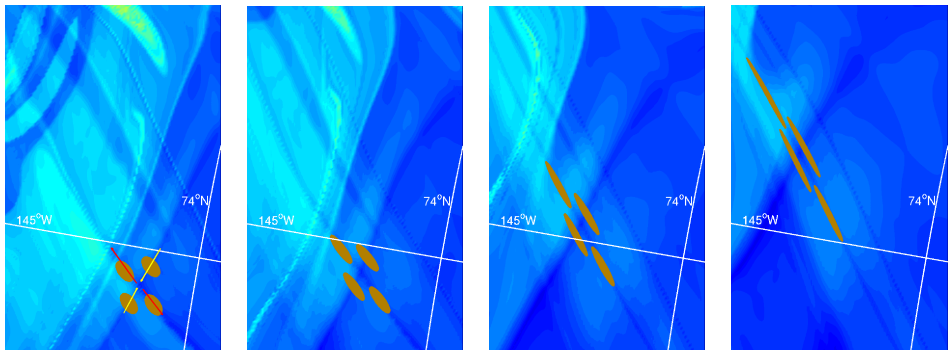

a) 1st April 2013 b) 1st May 2013 c) 1st June 2013 d) 1st July 2013

Figure 5.3: Evolution of the structures arising over the Beaufort Sea area as sharp changes of the values of M for an integration time of $\tau = 300$ days. Panel a) depicts four blobs of fluid particles aligned with the stable and unstable manifolds of a hyperbolic trajectory located in the Beaufort Sea at 1st April 2013. The directions of the stable and unstable manifolds of the hyperbolic trajectory are marked in yellow and red color respectively. b), c) and d) show the evolution of the four blobs of particles and of the surrounding Lagrangian structures on different dates.

Figure 5.4 shows function M also has the capability of highlighting jets present in the fluid [Mancho *et al.*, 2013; de la Cámara *et al.*, 2010, 2013; Curbelo *et al.*, 2017]. In this particular case, the TDS is clearly visible and the cyan greenish color highlights the parts of the jet with the highest speeds. This figure shows the evolution of a blob between the 15th August 2013 and the 1st January 2014. The blob evolves within the jet with almost no distortion, confirming the schematic representation of Figure 5.2. Typically vortex- or jet-like structures are mathematically related for periodic domains to one dimensional tori (1-tori) or two dimensional tori (2-tori). In continuous time systems 1-tori are periodic trajectories; these are localized and characterized by a single frequency and they trap regions of fluid. 2-tori are characterized by two frequencies whose ratio is not a rational number (they are said to be incommensurate). While such trajectories are not closed (which would be the case for periodic orbits), they trace out a two-dimensional torus. Such

a flow structure traps regions of fluid in the same way as periodic orbits. There exist formal results linking contour lines of the time average of M with tori-like invariant sets [Lopesino *et al.*, 2017]. In this manner, contour lines of converged averages of M highlight invariant tori. In the Arctic case, however, the average of M does not converge as the flow is aperiodic and thus contours of M do not strictly represent invariant sets.

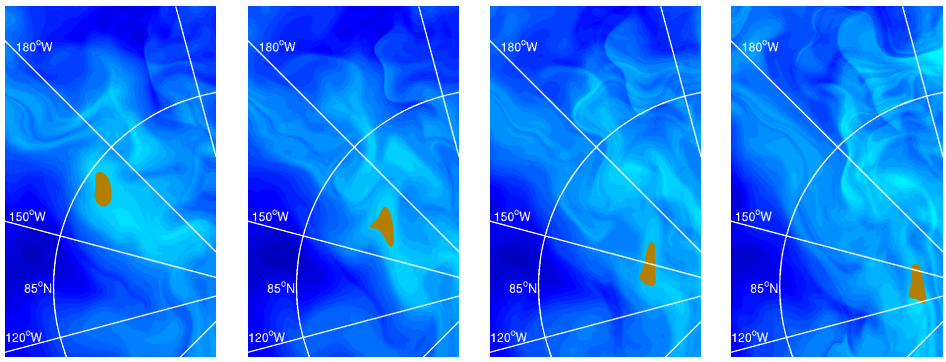

a) 15th Aug 2013 b) 1st Oct 2013 c) 15th Nov 2013 d) 1st Jan 2014

Figure 5.4: Identification of the Transpolar Drift Stream (TDS) in the Arctic Ocean by means of function M evaluated with $\tau = 300$ days. At 15th August 2013 (picture a)) a blob of water particles is placed on the jet. The evolution of the fluid blob and the Lagrangian structures based on function M are shown in panels b), c) and d) on different dates.

5.3 The Arctic Ocean circulation

In this section the major circulation currents in the Arctic Ocean are described from an Eulerian point of view, which takes into consideration the instantaneous velocity fields only and not the Lagrangian transport related to them. A summary of the circulation patterns at the surface are displayed in Fig. 5.5.

The geographic location of the Arctic Ocean and its physical characteristics make its environment unique among all the seas. It is connected with the major ocean basins through four geographical features: the Bering Strait, the Canadian Archipelago, the Fram Strait and the Barents Sea. From these regions, the Fram Strait and the Barents Sea concentrate almost all of the water exchange. The limited connection with the Pacific and the Atlantic Ocean due to the bathymetry formally classifies the Arctic as a mediterranean sea. Currents in mediterranean seas are driven mainly by temperature and salinity gradients (the salinity effect usually dominates) and also by atmo-

spheric winds [Tomczak & Godfrey, 1994], contrary to the dynamics of the major ocean basins, where the wind is the most influential factor. The Arctic Ocean is also characteristic because of its positive precipitation-evaporation balance. The amount of river run-off and melted snow widely overcomes the total evaporation of water in the Arctic, and this situation produces an evident contrast between ocean layers at different depths. According to their physical properties, the water masses are classified as: *Arctic Surface Water* (which occupies the depth ranging from the surface to 150-200 m), *Atlantic Water* (between depths of about 150 m and 900 m) and *Arctic Bottom Water* (from 1000 m to the ocean floor).

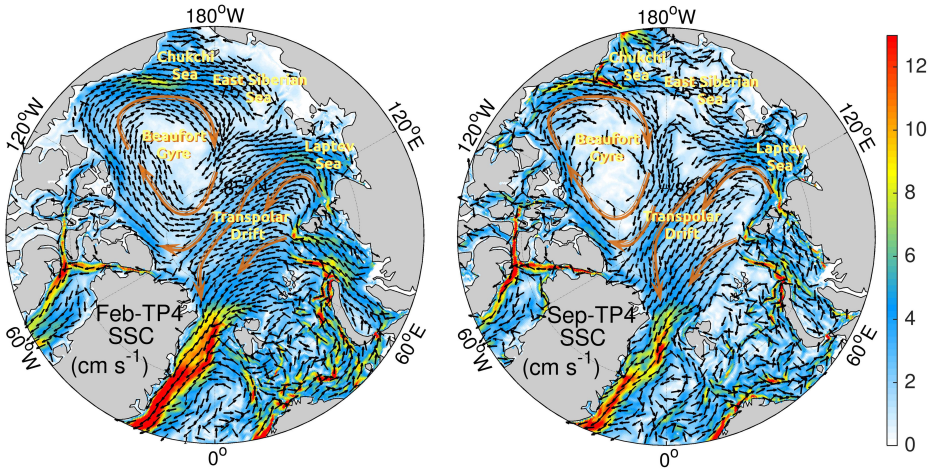

Figure 5.5: The Arctic mean ocean current circulations near surface in February (left) and September (right) from the TOPAZ reanalysis during 1993-2013. The current speeds are denoted by shading and the velocity vectors are shown at every 6 model grids, except where the mean velocity is below 1 cm/s.

Among all the ocean currents within the Arctic, the TDS carries to the North Atlantic the largest volume of sea ice. Its main path originates in the East Siberian Sea, where freshwater coming from the Siberian rivers is discharged. The TDS then flows transversally across the Arctic Basin, close to the North Pole and ends in the Fram Strait, the main outflow of the Arctic Ocean. The TDS is mainly a wind-driven current which has not experienced significant variations in the second half of the 20th century [Mysak, 2001], except for distortions induced by the phenomenon known as the Arctic Oscillation (AO), consisting in air mass fluctuations. The AO influence has implied a curved path of the TDS from the early 1980s towards the Beaufort Sea before exiting the Arctic [Macdonald *et al.*, 2005].

5.4 Lagrangian analysis results

Fig. 5.5 indicates the general circulation patterns of the Arctic Ocean currents near surface by the TOPAZ reanalysis. Next the results of the Lagrangian transport analysis over the Arctic by means of the function M are discussed. We study velocity fields at 30 m depth (within the halocline), therefore the ocean currents do not bear the marks of the sea ice motions on the surface. According to the values that function M takes over the central Arctic Ocean, highlighted in Fig. 5.6, we can establish the existence of a permanent jet, the TDS, crossing the region transversally. This is also confirmed in the movie S1 (which shows the evaluation of M with $\tau = 300$ days from the 1st March 2013 until the 1st March 2015). As pointed out in section 5.2.2, higher values of M indicate sea areas where fluid particles move faster. Lower values of M are represented in dark blue. Movie S1 confirms that the intensities of the currents become lower in winter and spring time, which are seasons characterized by the thickest sea ice. The thick ice cover inhibits the sea-air interactions, which yields a decay in the velocity of fluid particles. Therefore function M takes lower values when evaluated over these seasons, and we observe variations in the intensity of these jets throughout a one-year period. Visible also from M in the movie is the main branch of the TDS and other jets coming from the Siberian coast. In particular the movie shows that from December 2013 onwards, the TDS is fed also by a current branch bringing waters from the Laptev Sea. This is a normal circulation feature in the Arctic for a year of positive AO like 2013 (see *http://www.cpc.ncep.noaa.gov/*).

Fig. 5.6 shows the evaluation of M in central Arctic at four specific dates, starting the 15th April 2013 and ending the 15th of January 2015. The second row shows the results for $\tau = 100$ days and the third row for $\tau = 300$ days. The shorter integration period ($\tau = 100$ days) highlights the structure of the jet forming the Transpolar Drift current. At longer integration periods ($\tau = 300$ days) these features dilute, reflecting that their barrier character weakens in time. The first row in Fig. 5.6 shows the salinity concentration for the corresponding dates. We observe a strong correlation between the strong salinity gradients and the Transpolar Drift position, confirming that it acts as a barrier holding freshwater in the Canada Basin. The barrier character of the Transpolar Drift is further examined in the third row of Fig. 5.6. Two particle blobs are placed on both sides of the TDS at the 15th April 2013. Their evolution is displayed in this row through panels a) to d). Panel b) confirms that blobs continue separated at the 15th November 2013, seven months later. Panels c) and d) show that after more than one year, waters at both sides of the Transpolar drift are eventually at the same side. These findings are consistent with the weakening of the jet features displayed by M

at longer integrations periods, and with observations.

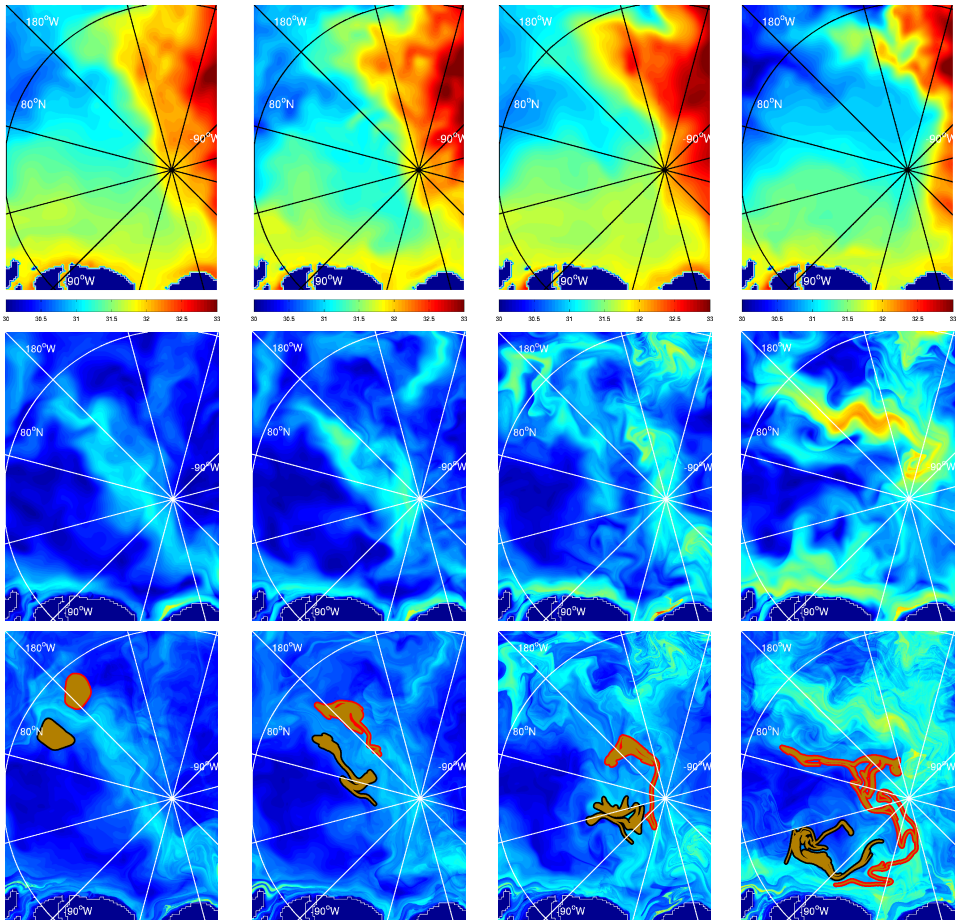

a) 15th Apr 2013 b) 15th Nov 2013 c) 15th Jun 2014 d) 15th Jan 2015

Figure 5.6: The upper row panels represent salinity (in parts per thousand) on different dates running from 15th April 2013 (column a)), 15th November 2013 (column b)), 15th June 2014 (column c)), to 15th January 2015 (column d)). The colorbar varies from 30 to 33 ppt of salt in water. The second and third rows represent function M calculated respectively with $\tau = 100$ and $\tau = 300$ days. The lower row includes two blobs of water particles depicted in brown at both sides of the Transpolar Drift Stream which are advected throughout the panels.

Figure 5.7 shows the evolution of the temperature and salinity averages within each blob for almost two years. The time series exhibit intermittent jumps caused by the Ensemble Kalman Filter assimilation updates, probably related to assimilation of sea ice concentrations, whose increments seem to have zero average. They are restricted both temporally to the Summer 2013

and regionally to the Eastern Transpolar Drift waters. The temperatures follow a weak seasonal cycle of about 0.2 deg, less pronounced in the Eastern Transpolar Drift waters due to the higher ice coverage and thicker ice shelter. The salinities increase during the period January to May 2014 due to brine rejection, then decrease slightly during the following melt season.

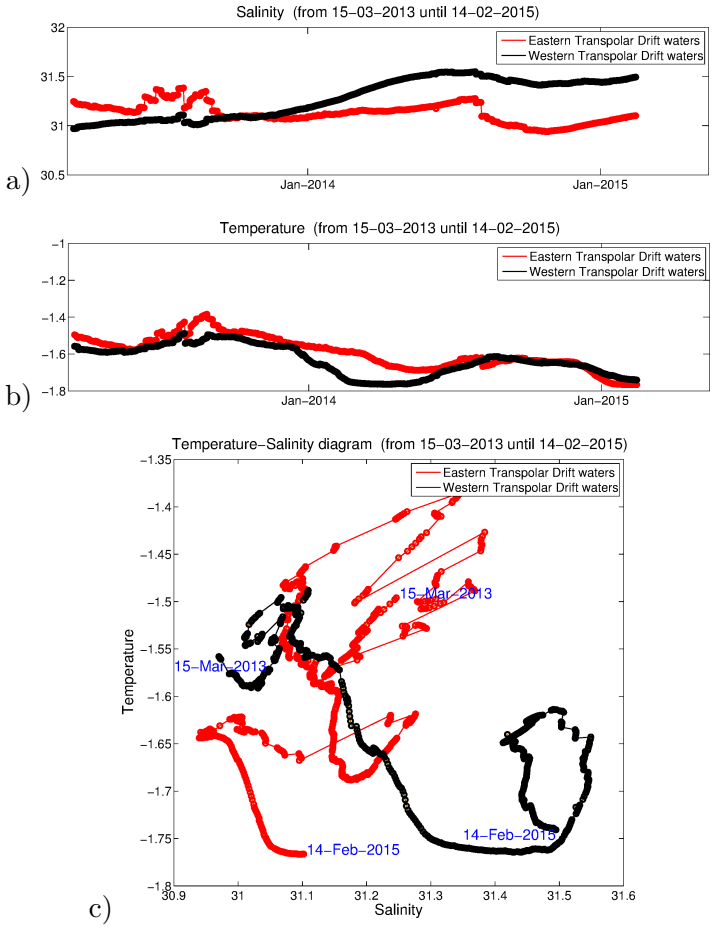

Figure 5.7: Evolution of averaged properties in the blobs placed at both sides of the Transpolar Drift (see Figure 5.6). a) Evolution of the salinity average within each blob; b) evolution of the temperature average within each blob; c) Temperature-Salinity diagram for the time series displayed in a) and b).

After the second summer, the temperatures become the same in both blobs but the salinities keep an offset of about 0.4 psu with Eastern waters fresher than Western waters. The water masses had almost identical properties in the Fall 2013 but differences of ice coverage and mixing with neighbouring water masses, both lateral and vertical, have accentuated their differences. The blobs do not homogenize their salinity since the western waters circulate

clockwise towards the South of the Canada Basin, were more salty waters are found.

Another major feature displayed in Figure 5.5 is the Beaufort Gyre which has been characterised as a wind-driven current which accumulates the largest amount of freshwater in the Arctic Ocean. Figure 5.8 confirms the presence of a salinity anomaly in the Beaufort Sea. Later on dynamical insights into the presence of this anomaly are provided, in particular to the salinity front transversal to the coast of Alaska, that retains Pacific salty waters.

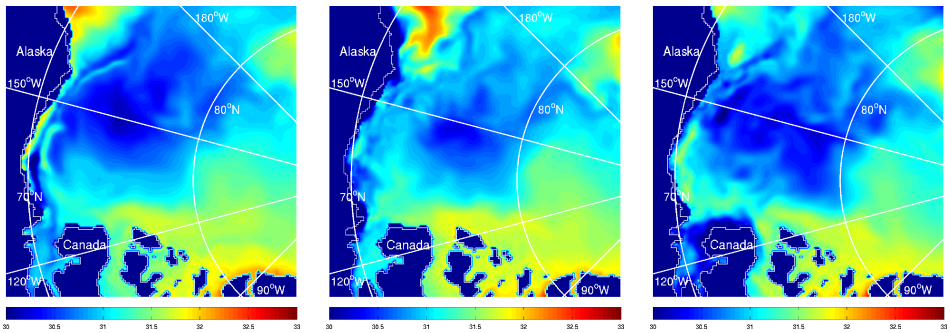

a) 1st April 2013 b) 1st October 2013 c) 1st December 2013

Figure 5.8: Representation of the salinity (in parts per thousand) at 30 m depth for different dates over the Beaufort Sea region. The colorbar varies from 30 to 33 ppt of salt in water.

Figure 5.9 displays function M calculated at 1st April 2013 for $\tau = 300$ days in this area. In this figure intricate lines that correspond to the pattern of the attracting and repelling material lines are emphasized with a white square. Figure 5.10a zooms into these details. A strong greenish feature in the M function along the coast of North America highlights a strong current which oscillates in time (see movie S1), transporting fluid material from Canada towards Alaska in the direction sketched by the magenta arrow. The movie additionally shows that this current finds an opposing current coming from Alaska, both resulting in a bent current preventing direct water flux from the Bering Strait to the Beaufort Sea. This configuration forces the presence of a detachment point, a moving saddle along the coast of North America, which is evident in Fig. 5.11. Fig. 5.11a shows the evaluation of function M at 15th October 2013 and the white square highlights the area in which the aforementioned hyperbolic trajectory is placed. Fig. 5.11b zooms into this region, showing the position of the hyperbolic trajectory with a white dot. Red and purple arrows show respectively the unstable and stable directions with their associated manifolds in black.

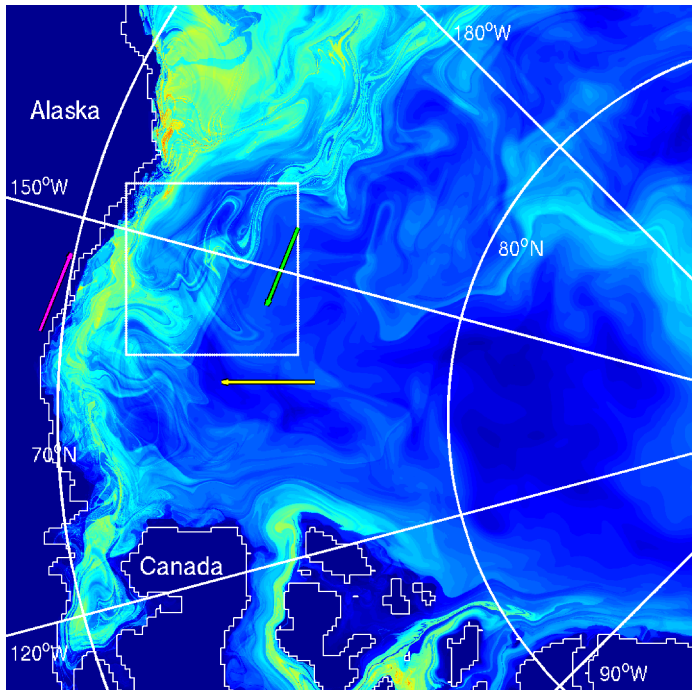

Figure 5.9: Global view of the Lagrangian structures arising over the Beaufort Sea area at 1st April 2013 at 30 m depth, which are identified by the sharp changes in the values of M (evaluated for $\tau = 300$ days). The green, yellow and magenta arrows mark transport directions of the fluid flow meanwhile the white square indicates an area of strong mixing (highlighted in Figure 5.10) whose dynamics is subjected to these transport directions.

Detachment points are special configurations of the hyperbolic trajectory, which are related to the phenomena of flow separation. In the detachment configuration the stable manifold is aligned with the coastline and the unstable manifold is transversal to it. Indeed backwards integrations of particles placed in the neighbourhood of the hyperbolic point at 15th October are displayed in Fig. 5.11d. At 1st October particles were spread along the stable manifold of this hyperbolic trajectory and its alignment with the coast is confirmed. The position of the saddle in this day is marked with the black dot, which corroborates its moving character. Analogously forward integrations of particles placed in the neighbourhood of the hyperbolic point at 15th October are displayed in Fig. 5.11d for the 1st December, confirming that the unstable manifold is transversal to the coast. Strictly speaking the saddle is not on the coast but very close to it, and therefore two branches are recognized for the unstable manifold: one short branch pointing out to the coast and another penetrating towards the Arctic interior. This manifold forms a dynamical barrier that fluid parcels from Pacific waters do not cross. The

barrier character of this feature is confirmed by the evolution of particle blobs at both sides, as visible in Figure 5.12. Figures 5.12a, 5.12b, 5.12c show the evolution of the blobs at selected dates while figures 5.12d) and 5.12e) show the time evolution of the average of temperature and salinity within each blob. These diagrams confirm that the barrier is present for several months and that after a period the waters eventually mix.

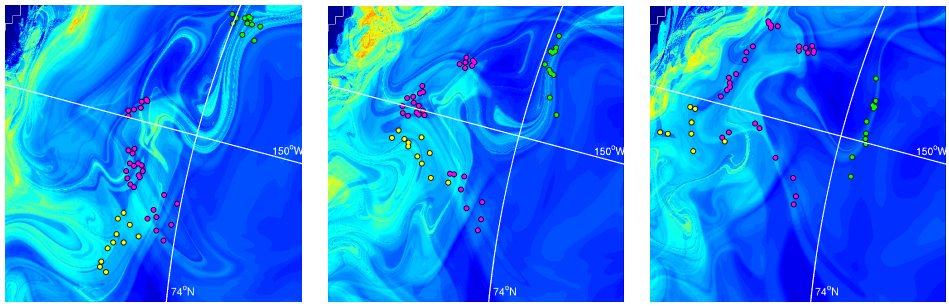

a) 1st April 2013 b) 1st June 2013 c) 1st August 2013

Figure 5.10: Evolution along a 4 months period of sets of water particles located at the Beaufort Sea. These are depicted in different colours according to the arrows denoting directions of the evolution of fluid parcels in Figure 5.9. At the initial date a) these were located at distinct sharp structures generated by function M. The evolution of these particles is depicted over the representation of function M computed with $\tau = 300$ days.

A zoom of the manifold skeleton associated with the moving saddle is visible in Figure 5.10. These pictures show a blow-up of the complex patterns contained within the white box of Figure 5.9. A yellow arrow in Figure 5.9 shows the position of stable manifolds which eventually transport material towards the major current, and the green arrow indicates penetration paths from the current to the Beaufort Sea according to the unstable manifolds. The set of three arrows compose a clockwise motion which we identify with the Beaufort Gyre. The material surfaces just described are time dependent and their time evolution is visible in movie S1. More specifically, Figure 5.10 shows particles coloured green placed over visible unstable manifold features. Their time evolution from the 1st April 2013 to the 15 August 2013 displayed in panels a), b) and c) confirm the motion according to the green arrow in figure 5.9. Yellow particles in figure 5.10 are placed just over visible stable manifold features, and their time evolution in this period is in agreement with the yellow arrow in Figure 5.9. Finally magenta particles in Figure 5.10 are placed over visible stable and unstable manifold intersections which again evolve in agreement with the magenta arrow providing evidence of a clockwise pattern. The movie confirms these findings on the transport routes as defined by the stable and unstable manifolds according to an anticyclonic

(clockwise) gyre. In the transport description provided by function M there is no sign of a big coherent gyre with a diameter of hundreds of kilometers as Fig. 5.5 seems to suggest. The mechanism just described above shows mixing within the Beaufort Sea.

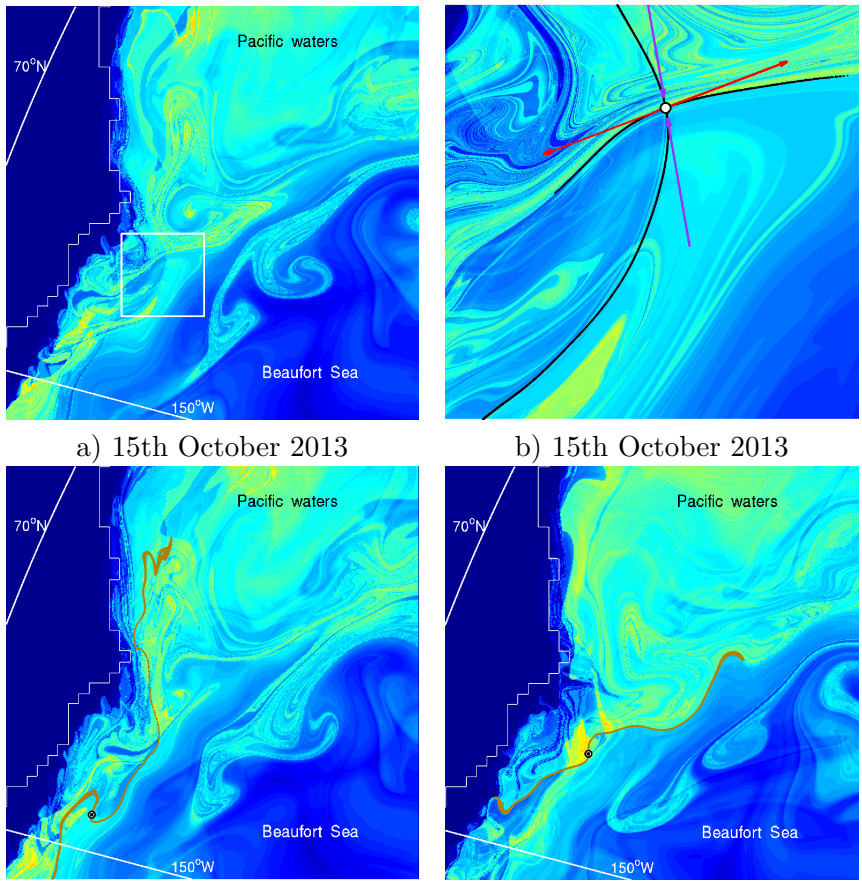

a) 15th October 2013 b) 15th October 2013

c) 1st October 2013 d) 1st December 2013

Figure 5.11: Configuration of a detachment point in the Arctic coastline. a) Evaluation of the function M at 15th October 2013. The white box highlights the neighbourhood of the hyperbolic trajectory; b) zooms into the area bounded by the white box. A white dot marks the position of the hyperbolic trajectory. Red and purple arrows show respectively the unstable and stable directions with their associated manifolds in black; c) backwards integrations of particles placed in the neighbourhood of the hyperbolic point at 15th October showing their position at 1st October; d) forwards integrations of particles placed in the neighbourhood of the hyperbolic point at 15th October showing their position at 1st December. Function M is evaluated with $\tau = 300$ days at every picture and their corresponding dates.

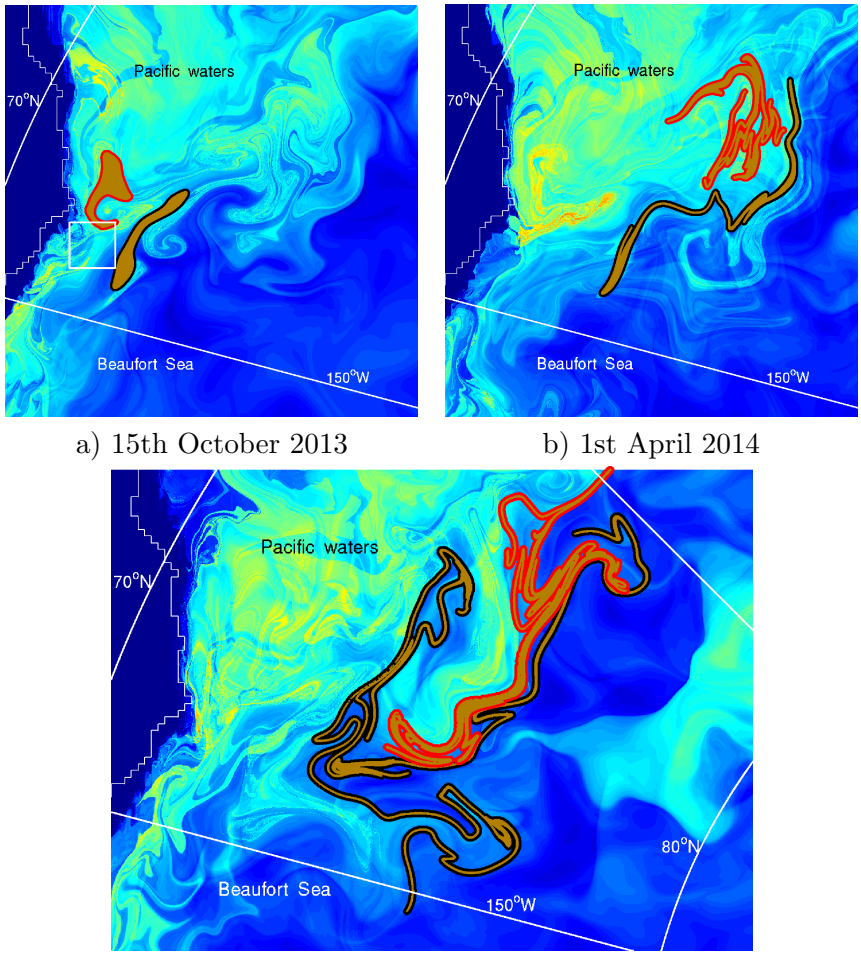

a) 15th October 2013 b) 1st April 2014

c) 1st October 2014

Figure 5.12: Evolution of a same pair of blobs of Pacific and Beaufort water masses at different dates.

Similarly to the previous section where the TDS is analized, the evolution of the water masses in the two blobs is depicted in Figure 5.12. In The Beaufort Sea the data assimilation updates are weaker except for a 0.3 psu increase of the salinities in the Beaufort Sea water blob at 1st October 2013. Pacific waters are initially warmer than Beaufort Sea waters by 1.5 deg (as indicated in Figure 5.13), but rapidly cool down during the fall 2013. During that time, melting and freezing of ice above the Beaufort Sea waters mostly changes its salinity but not its temperature. Freezing of surface water increases the salinity of Pacific waters. From January 2014 onwards both water masses have almost the same properties and remain stable until the end of summer 2014.

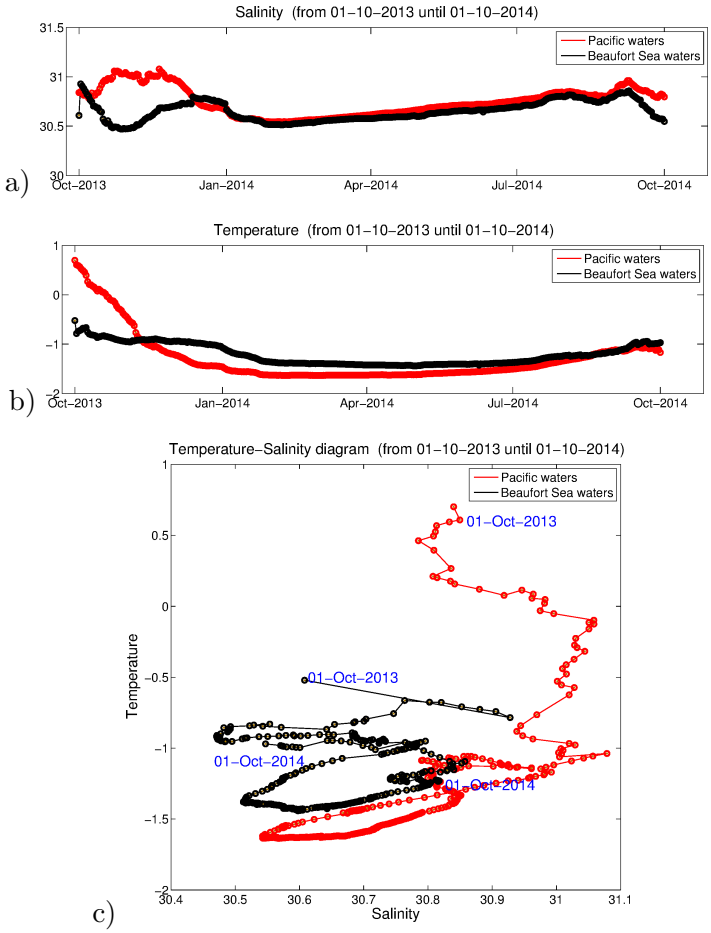

Figure 5.13: Pictures a) and b) represent the evolutions of the salinity and the temperature averages within each blob in Figure 5.12. Picture c) is the Temperature-Salinity diagram for the time series displayed in a) and b).

Finally the presence of a hyperbolic region in a detachment configuration provides a simple skeleton of transport in the Beaufort Gyre, that may provide interesting insights on issues that recently have drawn much attention, such as the case of the impact of oil spills in the Beaufort Sea [WWF, 2014]. These aspects are now under scrutiny, since the increasing reduction of ice cover in the Arctic is making this region more attractive to offshore activities such as oil and gas exploration. In particular, a region which is of potential interest for this type of exploitation is the Canadian coastline. The results discussed in this chapter suggest that spills occurring along this shore, would evolve in time by contracting themselves while approaching the detachment point according to the dynamics imposed by the stable manifold. Once in

the neighborhood of the saddle point, the spill would evolve following the unstable manifold, either by coming back to the coast consistently with one of the unstable branches or by moving far into the Beaufort Sea through the other unstable branch. The moving saddle thus marks the position of a highly dispersive region, which elongates the material of potential accidents pushing it towards the interior of the Arctic, i.e., towards regions of difficult accesses in the winter period, that would make support for oil spill remediation very complicated during several months. A recent article by García-Garrido *et al.* [2016] confirms the usefulness of this dynamical systems perspective to describe real oil-spill events.

Conclusions

This work as a whole provides new contributions and insights into nonautonomous dynamical systems, both from the theoretical point of view and from applications to what is known as the "dynamical systems approach" to geophysical fluid flows. Its conclusions are summarized as follows.

In Chapter 2, the adaptation of the autonomous Conley-Moser conditions (denoted by A1, A2 and A3) to the nonautonomous dynamical systems setting (exposed in Sections 2.2 and 2.2.1) provides a new way in which to formally prove the existence of invariant chaotic sets (in the Devaney sense) generated by sequences of maps. In the same way as for the autonomous conditions A1, A2 and A3, in the nonautonomous setting conditions (A1 + A3) imply that (A1 + A2) are satisfied, but proving the existence of a chaotic invariant set can still be done much more simply by verifying the fulfillment of conditions (A1 + A3) for a sequence of maps rather than (A1 + A2). An illustrative example is the one given by the sequence based on the classical Hénon map in Section 2.3, referred to as the nonautonomous Hénon map. The formal proof of these assumptions A1 and A3, step by step, clarifies the manner in which the chaotic set is built as well as the geometry behind this construction: the geometrical features sufficient for a 2-dimensional sequence of maps to exhibit chaos are basically a combination of (stretching + folding) properties. All this procedure is implemented in the nonautonomous Hénon map as a benchmark example by considering a sequence of maps based in the steady case, plus a small time dependent perturbation between consecutive iterations.

In Chapters 3 and 4, this monograph on nonautonomous dynamical systems moves to the study of the trajectories generated by differential equations influenced by noise, i.e. with random time dependence. This particular kind of dynamics, which certainly involves a key random factor, is referred to as stochastic and is incorporated into the general nonautonomous setting. The analysis is performed by means of a previously reported technique known as the method of Lagrangian descriptors, with the particularity that it needs to be redefined in order to be adapted to this new framework where solutions

display a distinct behaviour and take a different notation as well. The reformulation of phase space notions to the stochastic setting is supported by the correspondence between the simulations of the SLD function MS_p in the context of several stochastic differential equations models. A connection exists between the dynamical structures drawn by singular features and the paths traced by the trajectories generated by such systems. Although these examples only consider an additive noise in their expressions (the multiplicative case is then ignored), the SLD method still provides a satisfactory procedure for displaying the Lagrangian coherent structures underlying the dynamics generated by a stochastic differential equation. Additionally, a discussion is provided on the convenience of computing the mean values of the SLD function MS_p for several experiments in the same set of equations, which eventually may converge to a non-fluctuating output.

Finally, in Chapter 5, Arctic Ocean circulation is examined from a Lagrangian perspective. In this case the Lagrangian tool used is the original Lagrangian descriptor function M. Here, the main target is the exploration of the transport implications of ocean currents at a depth of 30 m (within the Arctic halocline) as regards salinity distribution and, potentially, the transport of other advected quantities. The focus is on a study conducted from March 2013 to March 2015 of two relevant Arctic features: the Transpolar Drift and the Beaufort Gyre. The graphical representations of function M reveal the Transpolar Drift as a jet-like dynamical barrier preventing Atlantic waters from invading the Canada Basin and supporting a strong salinity gradient in the area. The analysis shows that this dynamic feature may hold waters unmixed for periods of up to two years. In addition, the study of the Lagrangian structures in the Beaufort Sea area reveals the presence of a hyperbolic trajectory located near the North American coast in a detachment configuration. The hyperbolic point is a moving saddle with a stable manifold aligned with the coast, and an unstable manifold transversal to it which acts as barrier preventing salty Pacific waters from mixing with Beaufort Sea freshwater. Long term transport analysis confirms that stable and unstable manifolds of this hyperbolic region control clockwise transport in the interior of the Beaufort Gyre.

Conclusiones

Este trabajo aporta nuevas contribuciones en el área de los sistemas dinámicos no autónomos, tanto desde un punto de vista teórico como desde las aplicaciones, en lo que se conoce como "aproximación de los sistemas dinámicos" al transporte en flujos geofísicos. Sus conclusiones se resumen a continuación.

En el capítulo 2 la adaptación de las condiciones de Conley-Moser autónomas (denotadas como A1, A2 y A3) al marco de los sistemas dinámicos no autónomos (expuesta en las secciones 2.2 y 2.2.1) muestran una nueva manera de probar formalmente la existencia de conjuntos invariantes caóticos (en el sentido Devaney) generados por sucesiones de funciones. Tal y como ocurre para las condiciones autónomas A1, A2 y A3, en el marco no autónomo el cumplimiento de las condiciones (A1 + A3) implica que se satisfacen (A1 + A2); sin embargo, a la hora de probar la existencia de un conjunto invariante caótico en un proceso iterativo definido mediante una sucesión de funciones, resulta más sencillo comprobar (A1 + A3) que verificar (A1 + A2). En la sección 2.3 se aplican estas condiciones a una iteración definida mediante el mapa de Hénon no autónomo. La demostración formal de las proposiciones A1 y A3, paso a paso, clarifica la manera en la que se construye el conjunto caótico y la geometría involucrada en dicha construcción. Es decir, se explica que los rasgos geométricos suficientes para que una sucesión de funciones bidimensional presente una dinámica caótica, son básicamente una combinación adecuada de estiramientos y plegamientos. El mapa de Hénon no autónomo se construye como un modelo que implementa estas ideas, y para ello se parte de la función clásica de Hénon a la cual se añade una pequeña perturbación que varía entre iteraciones consecutivas.

En los capítulos 3 y 4 este estudio monográfico sobre sistemas dinámicos no autónomos analiza las trayectorias generadas por ecuaciones diferenciales estocásticas. Es decir, aquellas que modelizan fenómenos influidos por el ruido y que incluyen dependencia temporal aleatoria. Esta clase particular de ecuaciones, en las que ciertamente influye un factor aleatorio, se engloban en el marco no autónomo más general. Dicho análisis se realiza mediante la técnica de los descriptores lagrangianos, estudiada en referencias anteri-

ores. Nuestra contribución consiste en redefinir esta técnica para adaptarla a este nuevo contexto, donde las soluciones y su notación presentan diferencias respecto al caso determinista. La reformulación al ámbito estocástico de las nociones relacionadas con el espacio de fases viene apoyada por la correspondencia entre las distintas simulaciones de la función MS_p (en la cual se basa el método SLD) para varios modelos de ecuaciones diferenciales estocásticas. Existe una conexión entre las estructuras dinámicas dibujadas por rasgos singulares y las órbitas trazadas por las trayectorias a su vez generadas por dichos sistemas. Aunque los ejemplos tratados sólo consideran un ruido aditivo (se ignora el caso multiplicativo), se verifica que el método SLD proporciona un procedimiento satisfactorio para revelar estructuras lagrangianas coherentes, las cuales subyacen a las dinámicas generadas por una ecuación diferencial estocástica. Además se discute acerca de la conveniencia de estimar los valores medios de la función MS_p para varios experimentos y un mismo sistema de ecuaciones. Este proceso de promediado eventualmente convergería a un resultado sin fluctuaciones.

Por último en el capítulo 5 se examina la circulación en el océano Ártico desde una perspectiva lagrangiana. En este caso el análisis se realiza mediante la función M, el descriptor lagrangiano original. Aquí el objetivo principal es la exploración de cuáles son las implicaciones al transporte de las corrientes oceánicas a 30 metros de profundidad (en la haloclina del Ártico); en particular la incidencia respecto a la distribución de salinidad y, potencialmente, de otras cantidades advectadas. El estudio se centra en dos fenómenos relevantes del Ártico, la corriente del *Transpolar Drift* y el giro de Beaufort, en el período comprendido entre marzo de 2013 y marzo de 2015. A partir de la representación gráfica de la función M identificamos la corriente del *Transpolar Drift* como una barrera dinámica que evita que las aguas del Atlántico penetren en la cuenca de Canadá, exhibiendo en consecuencia un intenso gradiente de salinidad en el área. Dicho análisis muestra que las aguas pueden permanecer sin mezclarse durante períodos de hasta 2 años. Más aún, el estudio de las estructuras lagrangianas en el mar de Beaufort revelan la presencia de una trayectoria hiperbólica con una configuración de separación, localizada cerca de la costa de Norteamérica. La trayectoria hiperbólica es un punto de silla "móvil" con una variedad estable alineada con la costa y una variedad inestable transversal a la misma. Esta estructura actúa como barrera que impide la mezcla de las aguas salinas del Pacífico con las aguas dulces del mar de Beaufort. Un análisis del transporte a largo plazo confirma que las variedades estable e inestable de esta región hiperbólica controlan el transporte en sentido horario del interior del giro de Beaufort.

Appendices

Appendix 1. Chaotic saddle of the Hénon map

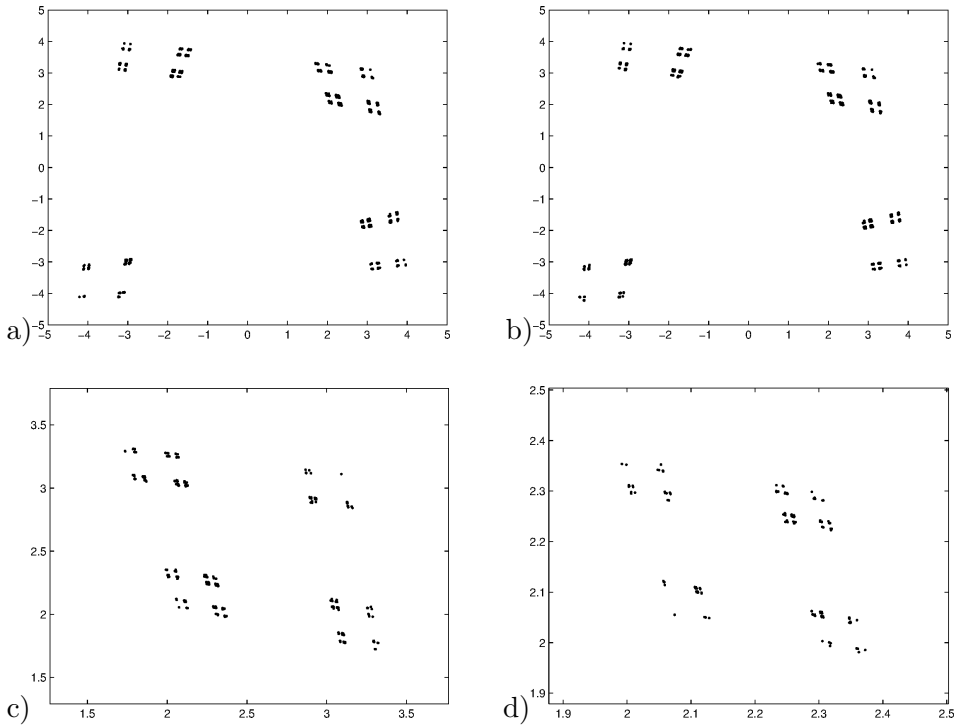

Figure 5.14: Graphical approximations to the invariant chaotic set generated by the nonautonomous Hénon map $H_n(x, y) = (A(n) - y - x^2, x)$ with $A(n) = 9.5 + \epsilon \cdot \cos(n)$, obtained by applying a finite number of iterations centered at $n = 0$. Panel a) represents the chaotic set for $\epsilon = 0$, conforming then the autonomous case. Panel b) represents the chaotic set for the nonautonomous case with $\epsilon = 0.1$. Panels c) and d) display details of the chaotic set in b).

Appendix 2. RDSs for time-dependent SDEs

As mentioned in Section 3.1 just after the introduction of random dynamical systems, this formal definition was only appropriate for SDEs with time-independent coefficients b, σ. Inspired in this Definition 10 given by Duan [2015], the same notion of RDS is developed for a more general context, where at least b or σ do depend explicitly on the time variable t. For this purpose it is necessary to consider a fourth argument for the solution mapping φ, which is the initial time t_0 when φ passes through the initial condition x_0. This has been done in the same way that processes are built from flow mappings in the deterministic differential equations setting.

Definition 16. *Let $\{\theta_t\}_{t\in\mathbb{R}}$ be a measure-preserving dynamical system defined over Ω, and let $\varphi : \mathbb{R}\times\mathbb{R}\times\Omega\times\mathbb{R}^N \to \mathbb{R}^N$ be a measurable mapping such that $(t, t_0, \cdot, x) \mapsto \varphi(t, t_0, \omega, x)$ is continuous for all $\omega \in \Omega$, and the family of functions $\{\varphi(t, t_0, \omega, \cdot) : \mathbb{R}^N \to \mathbb{R}^N\}$ has the cocycle property*

$$\varphi(t_0, t_0, \omega, x) = x \quad \textit{and}$$

$$\varphi(t_2, t_0, \omega, x) = \varphi(t_2, t_1, \theta_{(t_1-t_0)}\omega, \varphi(t_1, t_0, \omega, x))$$

$$\textit{for all} \quad t_0, t_1, t_2 \in \mathbb{R}, \quad x \in \mathbb{R}^N \quad \textit{and} \quad \omega \in \Omega.$$

Then the mapping φ is a random dynamical system with respect to the stochastic differential equation

$$dX_t = b(X_t, t)dt + \sigma(X_t, t)dW_t$$

if $\varphi(t, t_0, \omega, x)$ is a solution of the equation.

Appendix 3. Multiplicative Ergodic Theorem

The next results are taken from the book by Duan [2015]. These are essential in order to understand the hyperbolicity of a given stationary orbit $\tilde{X}(\omega)$ with respect to a random dynamical system φ.

The starting point is the centering φ at $\tilde{X}(\omega)$, therefore achieving a new RDS

$$\widetilde{\varphi}(t, \omega, x) = \varphi(t, \omega, \tilde{X}(\omega) + x) - \tilde{X}(\theta_t\omega).$$

This mapping $\widetilde{\varphi}$ retains the same dynamics as φ, with the difference that the constant value trajectory $X \equiv 0$ is a random fixed point for $\widetilde{\varphi}$. Now $\widetilde{\varphi}$ linearized with respect to the initial condition variable $x \in \mathbb{R}^N$ and evaluated at the initial condition $x = 0$:

$$\Phi(t, \omega) = \frac{\partial}{\partial x}\widetilde{\varphi}(t, \omega, x = 0) = \frac{\partial}{\partial x}\varphi(t, \omega, x = \tilde{X}(\omega))$$

allows to conveniently study whether or not $\tilde{X}(\omega)$ is hyperbolic by applying the following theorem.

Theorem 7 (**Multiplicative ergodic theorem (MET)**). *Let $\Phi(t,\omega)$ be a linear RDS (linear cocycle) in $\mathbb{R}^N$, for $t \in \mathbb{R}$, on a probability space $(\Omega, \mathcal{F}, \mathcal{P})$, over a measurable driving flow θ_t. Assume that the following integrability conditions are satisfied:*

$$\sup_{0\leq t\leq 1} \ln^+ ||\Phi(t,\omega)|| \in L^1(\Omega), \quad \sup_{0\leq t\leq 1} \ln^+ ||\Phi(-t,\omega)|| \in L^1(\Omega), \tag{5.4}$$

where $\ln^+(z) := \max\{\ln(z), 0\}$, denoting the nonnegative part of the natural logarithm. Then there exists an invariant set $\widetilde{\Omega} \in \mathcal{F}$ of full probability measure, such that for every $\omega \in \widetilde{\Omega}$:

(i) the asymptotic geometric mean $\lim_{t\to\pm\infty}[\Phi(t,\omega)^T\Phi(t,\omega)]^{\frac{1}{2t}} = \widetilde{\Phi}$ exists and it is nonnegative definite $N \times N$ matrix.

(ii) the matrix $\widetilde{\Phi}$ has distinct eigenvalues $e^{\lambda_p(\omega)} < \cdots, e^{\lambda_1(\omega)}, \omega \in \widetilde{\Omega}$, with corresponding eigenspaces $E_{p(\omega)}(\omega), \cdots, E_1(\omega)$ of dimensions $d_i(\omega) = \dim E_i(\omega), i = 1, \cdots, p(\omega)$. These eigenspaces are such that $E_1(\omega) \oplus E_2(\omega) \oplus \cdots \oplus E_{p(\omega)}(\omega) = \mathbb{R}^N$. Moreover, p, λ_i and d_i are invariant under the driving flow θ_t in the following sense:

$$p(\theta_t\omega) = p(\omega), \quad \lambda_i(\theta_t\omega) = \lambda_i(\omega) \quad \text{and} \quad d_i(\theta_t\omega) = d_i(\omega)$$

for $i = 1, \cdots, p, t \in \mathbb{R}$ and $\omega \in \widetilde{\Omega}$.

(iii) each $E_i(\omega)$ is invariant for the linear RDS: $\Phi(t,\omega)E_i(\omega) = E_i(\theta_t\omega)$, for all $\omega \in \widetilde{\Omega}$ and all $t \in \mathbb{R}$.

(iv) $\lim_{t\to\pm\infty} 1/t \ln ||\Phi(t,\omega)x|| = \lambda_i$ if and only if $x \in E_i(\omega) - \{0\}$, for all $\omega \in \widetilde{\Omega}$ and $i = 1, \cdots, p$.

Definition 17. *Let $\Phi(t,\omega)$ be a linear RDS in $\mathbb{R}^N$ that satisfies the initial conditions of the MET. The vector subspaces based on the Oseledets spaces*

$$E^s(\omega) = \bigoplus_{\lambda_i<0} E_i(\omega) \quad , \quad E^c(\omega) = \bigoplus_{\lambda_i=0} E_i(\omega) \quad , \quad E^u(\omega) = \bigoplus_{\lambda_i>0} E_i(\omega)$$

are called the stable, center and unstable subspaces of $\Phi(t,\omega)$, respectively. The family of its Lyapunov exponents and their corresponding multiplicities

$$\{\lambda_1, \cdots, \lambda_p; d_1, \cdots, d_p\}$$

is called the Lyapunov spectrum of $\Phi(t,\omega)$. Moreover if all the Lyapunov exponents are nonzero then the linear RDS $\Phi(t,\omega)$ is said to be hyperbolic.

As mentioned before in Section 3.1, the random dynamical system (3.8) associated to the noisy saddle (3.7) satisfies the conditions of the Multiplicative ergodic theorem. This fact and the simplicity of the noisy saddle, allows to compute explicitly the Lyapunov spectrum and the stable and unstable subspaces of the RDS $\Phi(t,\omega)$ linearized over the stationary orbit $\tilde{X}(\omega)$.

Example 3 (**Noisy saddle point**)**.** The random dynamical system φ corresponding to the noisy saddle (3.7) takes the expression

$$\begin{array}{rccc} \varphi: & \mathbb{R}\times\Omega\times\mathbb{R}^2 & \longrightarrow & \mathbb{R}^2 \\ & (t,\omega,(x,y)) & \longmapsto & (\varphi_1(t,\omega,x),\varphi_2(t,\omega,y)) \\ & & & = \left(e^t\left(x+\int_0^t e^{-s}dW_s^1(\omega)\right), e^{-t}\left(y+\int_0^t e^{s}dW_s^2(\omega)\right)\right). \end{array}$$

The Jacobian matrix $D_{(x,y)}\varphi$ does not depend on the third argument, let say the initial condition (x,y),

$$\Phi(t) = D_{(x,y)}\varphi(t,\omega,(x,y)) = \begin{pmatrix} e^t & 0 \\ 0 & e^{-t} \end{pmatrix}.$$

As this linear cocycle is a diagonal matrix, its norm corresponds to the largest element of its diagonal, which is also the largest eigenvalue. In this case

$$||\Phi(t)|| = ||\Phi(-t)|| = \begin{cases} e^t & \text{for } t \geq 0 \\ e^{-t} & \text{for } t < 0 \end{cases} \qquad \text{and}$$

$$\sup_{0\leq t\leq 1} \ln^+ ||\Phi(t)|| = \sup_{0\leq t\leq 1} \ln^+ ||\Phi(-t)|| = \sup_{0\leq t\leq 1} |t| = 1.$$

As any constant function belongs to the space of functions $L^1(\Omega)$ (remember that the probability space Ω has measure equal to 1), the conditions of the MET are satisfied. Now for the asymptotic geometric mean

$$\widetilde{\Phi} = \lim_{t\to\pm\infty} [\Phi(t)^T\Phi(t)]^{\frac{1}{2t}} = \left[\begin{pmatrix} e^t & 0 \\ 0 & e^{-t} \end{pmatrix}\cdot\begin{pmatrix} e^t & 0 \\ 0 & e^{-t} \end{pmatrix}\right]^{\frac{1}{2t}}$$

$$= \begin{pmatrix} e^{2t} & 0 \\ 0 & e^{-2t} \end{pmatrix}^{\frac{1}{2t}} = \begin{pmatrix} e^1 & 0 \\ 0 & e^{-1} \end{pmatrix},$$

its associated eigenvalues are e^1 and e^{-1}, with corresponding eigenspaces respectively

$$\text{span}\{\begin{pmatrix} 1 \\ 0 \end{pmatrix}\} \quad \text{and} \quad \text{span}\{\begin{pmatrix} 0 \\ 1 \end{pmatrix}\}.$$

These two linear subspaces are precisely the unstable $E^u(\omega)$ and the stable $E^s(\omega)$ subspaces of $\Phi(t)$, for which the Lyapunov spectrum is $\{\lambda_1 = 1, \lambda_2 =$

$-1\}$, therefore confirming the hyperbolic nature of the stationary orbit. It results evident that for any other more complex SDE, the computation of the asymptotic geometric mean $\tilde{\Phi}$ would be more tricky; highlighting that this process is not straightforward for most SDEs.

What remains is to establish the relationship between the linear subspaces $E^u(\omega)$, $E^s(\omega)$ and the already mentioned $\mathcal{U}(\omega)$, $\mathcal{S}(\omega)$. This is discussed in Theorem 3.1 from [Mohammed & Scheutzow, 1999], where the local unstable and the local stable manifolds of a stationary orbit $\tilde{X}(\omega)$ are related to the sets of points (in a neighborhood of $\tilde{X}(\omega)$) which are attracted by the stationary orbit in negative or positive time, respectively. In summary this fact presents many similarities with the definition of exponential dichotomy for deterministic dynamical systems. Indeed this exponentially attracting rate over the points of the manifolds $\mathcal{U}(\omega)$, $\mathcal{S}(\omega)$ of the noisy saddle (3.7) is easily observed in Equation (3.13),

$$\begin{aligned}(\overline{x}_t, \overline{y}_t) - (\tilde{x}(\theta_t\omega), \tilde{y}(\theta_t\omega)) &= \varphi(t, \omega, (\overline{x}_0, \overline{y}_0)) - \varphi(t, \omega, (\tilde{x}(\omega), \tilde{y}(\omega))) \\ &= \left(\epsilon_1(\omega)e^t, \epsilon_2(\omega)e^{-t}\right),\end{aligned}$$

regardless the initial distance $(\epsilon_1(\omega), \epsilon_2(\omega))$ of $(\overline{x}_t, \overline{y}_t)$ to the stationary orbit $\tilde{X}(\omega)$. Moreover, as this distance can be arbitrarily large, the dynamics in a neighborhood of $\tilde{X}(\omega)$ are also achieved for the rest of trajectories within the invariant sets $\mathcal{U}(\omega)$, $\mathcal{S}(\omega)$, giving to these a global property. This argument enables to simply refer to $\mathcal{U}(\omega)$ and $\mathcal{S}(\omega)$ as the unstable and stable manifolds of the stationary orbit of the noisy saddle equation (3.7). □

Appendix 4. Computation of function M

The procedure to compute the values of function M from CMEMS data detailed in Chapter 5 is composed by several steps, which are summarized as follows.

- **Step 1.** Data are downloaded from *http://marine.copernicus.eu*, the CMEMS website, and saved in *.nc* format. In order to facilitate their usage, data are stored on a monthly basis.
- **Step 2.** These data comprises the values of salinity, temperature, the horizontal/vertical velocity components u, v, and other parameter values. All them are defined over a squared 2-dimensional grid of nodes with a spatial resolution of 12.5×12.5 km. Moreover these are given at 12 distinct sea levels, varying from 5 to 3000 metres depth in the sea.
- **Step 3.** As mentioned before, the velocity fields components u, v are expressed in Cartesian coordinates, avoiding issues at the North Pole

derived from the computation of trajectories in spherical coordinates. Fluid particle trajectories are evolved in the Cartesian system with the given velocity fields within a fixed sea layer.

- **Step 4.** The previous data files stored in *.nc* format are directly loaded and processed by MATLAB© software. After arranging the different variables of the data into big size matrices, these need to be interpolated when integrating the water particle trajectories. In order to save memory and computer resources, it is implemented an interpolation function of first order (command `Interp1` with option `'pp'`) for the temporal domain (i.e. the time period of integration of trajectories) which generates an object that can be saved into the memory and evaluated at any point of interest at a later time. This is not the case for the space interpolation, which is of second order and directly computed at every integration step by means of command `Interp2`.

- **Step 5.** The dynamical system,

$$\frac{dx}{dt} = u(x, y, t) \quad , \quad \frac{dy}{dt} = v(x, y, t)$$

that advects the water particles, is integrated using a Cash Karp Runge-Kutta scheme [Press *et al.*, 1992] with a time step of 6 hours. All these computations are made by using a matrix formulation of the whole mesh grid of initial conditions, as well as for the intermediate points composing the trajectories. This fact ultimately achieves important computational savings.

- **Step 6.** The values that function M takes over the grid of initial conditions are obtained by approximating the integral in Eq. (4.2) by the sum of the lengths (in the Euclidean space) of the segments composing the already integrated trajectories. These segments are the ones linking the consecutive points (at two successive time steps) obtained at the integration of the trajectories corresponding to each of the initial conditions points.

Bibliography

Aagaard, K. & Carmack, E. C. [1989] "The role of sea ice and other fresh water in the Arctic circulation", *Journal of Geophysical Research*, **94**(C10), 14485-14498.

Alekseev, V. M. [1968a] "Quasirandom dynamical systems, I", *Mathematics of the USSR-Sbornik*, **5**, 73-128.

Alekseev, V. M. [1968b] "Quasirandom dynamical systems, II", *Mathematics of the USSR-Sbornik*, **6**, 505-560.

Alekseev, V. M. [1969] "Quasirandom dynamical systems, III", *Mathematics of the USSR-Sbornik*, **6**, 1-43.

Aref, H. [1984] "Stirring by chaotic advection", *Journal of Fluid Mechanics*, **143**, 1-21.

Arnold, L. [1998] "Random Dynamical Systems", *Springer*.

Aurell, E., Boffetta, G., Crisanti, A., Paladin, G. & Vulpiani, A. [1997] "Predictability in the large: an extension of the concept of Lyapunov exponent", *Journal of Physics A: Mathematical and General*, **30**(1), 1-26.

Balibrea-Iniesta, F., Lopesino, C., Wiggins, S. & Mancho, A. M. [2015] "Chaotic Dynamics in Nonautonomous Maps: Application to the Nonautonomous Hénon Map", *International Journal of Bifurcation and Chaos*, **25**(12), 1550172.

Balibrea-Iniesta, F., Lopesino, C., Wiggins, S. & Mancho, A. M. [2016] "Lagrangian Descriptors for Stochastic Differential Equations: A Tool for Revealing the Phase Portrait of Stochastic Dynamical Systems", *International Journal of Bifurcation and Chaos*, **26**(13), 1630036.

Balibrea-Iniesta, F., Xie, J., García-Garrido, V. J., Bertino, L., Mancho, A. M. & Wiggins, S. [2017] "Lagrangian transport in the Arctic Ocean", *(pre-print)*.

Banisch, R. & Koltai, P. [2017] "Understanding the geometry of transport: Diffusion maps for Lagrangian trajectory data unravel coherent sets", *Chaos*, **27**(3), 035804.

Bettencourt, J. H., López, C., Hernández-García, E., Montes, I., Sudre, J., Dewitte, B., Paulmier, A. & Garçon, V. [2015] "Boundaries of the Peruvian oxygen minimum zone shaped by coherent mesoscale dynamics", *Nature Geoscience*, **8**, 937–940.

Bleck, R. [2002] "An oceanic general circulation model framed in hybrid isopycnic-Cartesian coordinates", *Ocean Modelling*, **4**(1), 55-88.

Boxler, P. [1989] "A stochastic version of center manifold theory", *Probability Theory and Related Fields*, **83**(4), 509-545.

Branicki, M. & Kirwan Jr., A. D. [2010] "Stirring: The Eckart paradigm revisited", *International Journal of Engineering Science*, **48**(11), 1027–1042.

de la Cámara, A., Mechoso, C. R., Ide, K., Walterscheid, R. & Schubert, G. [2010] "Polar night vortex breakdown and large-scale stirring in the southern stratosphere", *Climate Dynamics*, **35**(6), 965-975.

de la Cámara, A., Mancho, A. M., Ide, K., Serrano, E. & Mechoso, C. R. [2012] "Routes of Transport across the Antarctic Polar Vortex in the Southern Spring", *Journal of the Atmospheric Sciences*, **69**(2), 741-752.

de la Cámara, A., Mechoso, C. R., Mancho, A. M., Serrano, E. & Ide, K. [2013] "Isentropic Transport within the Antarctic Polar-Night Vortex: Rossby Wave Breaking Evidence and Lagrangian Structures", *Journal of the Atmospheric Sciences*, **70**(9), 2982-3001.

Cheng, Z., Duan, J. & Wang, L. [2016] "Most probable dynamics of some nonlinear systems under noisy fluctuations", *Communications in Nonlinear Science and Numerical Simulation*, **30**(1-3), 108-114.

Cohen, J., Screen, J. A., Furtado, J. C., Barlow, M., Whittleston, D., Coumou, D., Francis, J., Dethloff, K., Entekhabi, D., Overland, J. & Jones, J. [2014] "Recent Arctic amplification and extreme mid-latitude weather", *Nature Geoscience*, **7**(9), 627-637.

Craven, G. T. & Hernandez, R. [2015] "Lagrangian Descriptors of Thermalized Transition States on Time-Varying Energy Surfaces", *Physical Review Letters*, **115**(14), 148301.

Craven, G. T. & Hernandez, R. [2016] "Deconstructing field-induced ketene isomerization through Lagrangian descriptors", *Physical Chemistry Chemical Physics*, **18**(5), 4008-4018.

Curbelo, J., García-Garrido, V. J., Mechoso, C. R., Mancho, A. M., Wiggins, S. & Niang, C. [2017] "Insights into the three-dimensional Lagrangian geometry of the Antarctic polar vortex", *Nonlinear Processes in Geophysics*, **24**(3), 379-392.

Datta, S. & Bhattacharjee, J. K. [2001] "Effect of stochastic forcing on the Duffing oscillator", *Physics Letters A*, **283**(5-6), 323-326.

Devaney, R. L. [1989] "An Introduction to Chaotic Dynamical Systems", *Addison-Wesley, New York and Reading.*

Devaney, R. L. & Nitecki, Z. [1979] "Shift automorphisms in the Hénon mapping", *Communications in Mathematical Physics*, **67**(2), 137-146.

Duan, J. [2015] "An Introduction to Stochastic Dynamics", *Cambridge University Press.*

García-Garrido, V. J., Mancho, A. M., Wiggins, S. & Mendoza, C. [2015] "A dynamical systems approach to the surface search for debris associated with the disappearance of flight MH370", *Nonlinear Processes in Geophysics*, **22**(6), 701-712.

García-Garrido, V. J., Ramos, A., Mancho, A. M., Coca, J. & Wiggins, S. [2016] "A dynamical systems perspective for a real-time response to a marine oil spill", *Marine Pollution Bulletin*, **112**(1-2), 201-210.

Haller, G. [2001] "Distinguished material surfaces and coherent structures in three-dimensional fluid flows", *Physica D: Nonlinear Phenomena*, **149**(4), 248-277.

Hénon, M. [1976] "A Two-Dimensional Mapping with a Strange Attractor", *Communications in Mathematical Physics*, **50**(1), 69-77.

Holmes, P. J. [1982] "The dynamics of repeated impacts with a sinusoidally vibrating table", *Journal of Sound and Vibration*, **84**(2), 173-189.

Hsieh, M. A., Forgoston, E., Mather, T. W. & Schwartz, I. B. [2012] "Robotic Manifold Tracking of Coherent Structures in Flows", *Robotics, IEEE International Conference on Robotics and Automation*, 4242-4247.

Hunke, E. C. & Dukowicz, J. K. [1997] "An Elastic-Viscous-Plastic Model for Sea Ice Dynamics", *Journal of Physical Oceanography*, **27**(9), 1849 -1867.

Hunt, B. R. & Ott, E. [2015] "Defining chaos", *Chaos*, **25**(0), 097618.

Ide, K., Small, D. & Wiggins, S. [2002] "Distinguished hyperbolic trajectories in time-dependent fluid flows: analytical and computational approach for velocity fields defined as data sets", *Nonlinear Processes in Geophysics*, **9**(3-4), 237-263.

Jones, E. P. [2001] "Circulation in the Arctic Ocean", *Polar Research*, **20**(2), 139-146.

Ju, N., Small, D. & Wiggins, S. [2003] "Existence and Computation of Hyperbolic Trajectories of Aperiodically Time Dependent Vector Fields and Their Approximations", *International Journal of Bifurcation and Chaos*, **13**(6), 1449-1457.

Junginger, A. & Hernandez, R. [2016a] "Lagrangian descriptors in dissipative systems", *Physical Chemistry Chemical Physics*, **18**(44), 30282-30287.

Junginger, A. & Hernandez, R. [2016b] "Uncovering the geometry of barrierless reactions using Lagrangian descriptors", *The Journal of Physical Chemistry B*, **120**(8), 1720-1725.

Katok, A. & Hasselblatt, B. [1995] "Introduction to the Modern Theory of Dynamical Systems", *Cambridge University Press.*

Kloeden, P. E. & Platen, E. [1992] "Numerical Solution of Stochastic Differential Equations", *Stochastic Modelling and Applied Probability*, **23**, *Springer-Verlag Berlin Heidelberg.*

Kloeden, P. E. & Rasmussen, M. [2011] "Nonautonomous Dynamical Systems", *Mathematical Surveys and Monographs*, **176**, *American Mathematical Society.*

Kloeden, P. E., Pötzsche, C. & Rasmussen, M. [2013] "Discrete-Time Nonautonomous Dynamical Systems", *Stability and Bifurcation Theory for Non-Autonomous Differential Equations. Lecture Notes in Mathematics*, **2065**, *Springer, Berlin, Heidelberg.*

Krishfield, R. A., Proshutinsky, A., Tateyama, K., Williams, W. J., Carmack, E. C., McLaughlin, F. A. & Timmermans, M.-L. [2014] "Deterioration of perennial sea ice in the Beaufort Gyre from 2003 to 2012 and its impact on the oceanic freshwater cycle", *Journal of Geophysical Research*, **119**(2), 1271-1305.

Large, W. G., McWilliams, J. C. & Doney, S. C. [1994] "Oceanic vertical mixing: A review and a model with a nonlocal boundary layer parameterization", *Reviews of Geophysics*, **32**(4), 363-403.

Lerman, L. & Silnikov, L. [1992] "Homoclinical structures in nonautonomous systems: Nonautonomous chaos", *Chaos*, **2**(3), 447-454.

Li, T. Y. & Yorke, J. A. [1975] "Period three implies chaos", *The American Mathematical Monthly*, **82**(10), 985-992.

Lopesino, C., Balibrea, F., Wiggins, S. & Mancho, A. M. [2015a] "Lagrangian descriptors for two dimensional, area preserving, autonomous and nonautonomous maps", *Communications in Nonlinear Science and Numerical Simulation*, **27**(1-3), 40-51.

Lopesino, C., Balibrea-Iniesta, F., Wiggins, S. & Mancho, A. M. [2015b] "The Chaotic Saddle in the Lozi Map, Autonomous and Nonautonomous Versions", *International Journal of Bifurcation and Chaos*, **25**(13), 1550184.

Lopesino, C., Balibrea-Iniesta, F., García-Garrido, V. J., Wiggins, S. & Mancho, A. M. [2017] "A Theoretical Framework for Lagrangian Descriptors", *International Journal of Bifurcation and Chaos*, **27**(1), 1730001.

Lorenz, E. N. [1963] "Deterministic Nonperiodic Flow", *Journal of the Atmospheric Sciences*, **20**(2), 130-141.

Lu, K. & Wang, Q. [2010] "Chaos in differential equations driven by a nonautonomous force", *Nonlinearity*, **23**(11), 2935-2975.

Lu, K. & Wang, Q. [2011] "Chaotic behavior in differential equations driven by a Brownian motion", *Journal of Differential Equations*, **251**(10), 2853-2895.

Madrid, J. A. J. & Mancho, A. M. [2009] "Distinguished trajectories in time dependent vector fields", *Chaos*, **19**(1), 013111.

Malhotra, N. & Wiggins, S. [1998] "Geometric Structures, Lobe Dynamics, and Lagrangian Transport in Flows with Aperiodic Time-Dependence, with Applications to Rossby Wave Flow", *Journal of Nonlinear Science*, **8**(4), 401–456.

Mancho, A. M., Small, D., Wiggins, S. & Ide, K. [2003] "Computation of stable and unstable manifolds of hyperbolic trajectories in two-dimensional, aperiodically time-dependent vector fields", *Physica D: Nonlinear Phenomena*, **182**(3-4), 188-222.

Mancho, A. M., Small, D. & Wiggins, S. [2006] "A tutorial on dynamical systems concepts applied to Lagrangian transport in oceanic flows defined as finite time data sets: Theoretical and computational issues", *Physics Reports*, **437**(3-4), 55-124.

Mancho, A. M., Hernández-García, E., Small, D., Wiggins, S. & Fernández, V. [2008] "Lagrangian transport through an ocean front in the North-Western Mediterranean Sea", *Journal of Physical Oceanography*, **38**(6), 1222-1237.

Mancho, A. M., Wiggins, S., Curbelo, J. & Mendoza, C. [2013] "Lagrangian descriptors: A method for revealing phase space structures of general time dependent dynamical systems", *Communications in Nonlinear Science and Numerical Simulation*, **18**(12), 3530-3557.

Mancho, A. M., Curbelo, J., Wiggins, S., García-Garrido, V. J. & Mendoza, C. [2015] "Beautiful Geometries Underlying Ocean Nonlinear Processes", Chapter of the book "A VOYAGE THROUGH SCALES: The Earth System in Space and Time", *European Geophysical Union*, 80-85.

Macdonald R. W., Harner, T. & Fyfe, J. [2005] "Recent climate change in the Arctic and its impact on contaminant pathways and interpretation of temporal trend data", *Science of the Total Environment*, **342**(1-3), 5-86.

Melsom, A., Simonsen, M., Bertino, L., Hackett, B., Waagbø, G. A. & Raj, R. [2017] "Quality information document for Arctic Ocean Physical Analysis and Forecast Product ARCTIC_ANALYSIS_FORECAST_PHYS_002_001_A", *Copernicus Marine Environment Monitoring Service*, *http://marine.copernicus.eu/documents/QUID/CMEMS-ARC-QUID-002-001a.pdf*.

Mendoza, C. & Mancho, A. M. [2010] "The hidden geometry of ocean flows", *Physical Review Letters*, **105**(3), 038501.

Mendoza, C. & Mancho, A. M. [2012] "The Lagrangian description of aperiodic flows: a case study of the Kuroshio Current", *Nonlinear Processes in Geophysics*, **19**(4), 449-472.

Mendoza, C., Mancho, A. M. & Wiggins, S. [2014] "Lagrangian descriptors and the assessment of the predictive capacity of oceanic data sets", *Nonlinear Processes in Geophysics*, **21**(3), 677-689.

Mohammed, S. E. A. & Scheutzow, M. K. R. [1999] "The Stable Manifold Theorem for Stochastic Differential Equations", *Annals of Probability*, **27**(2), 615-652.

Morison, J., Kwok, R., Peralta-Ferriz, C., Alkire, M., Rigor, I., Andersen, R. & Steele, M. [2012] "Changing Arctic Ocean freshwater pathways", *Nature*, **481**(7379), 66–70.

Moser, J. [1973] "Stable and Random Motions in Dynamical Systems", *Annals of Mathematical Studies*, **77**, *Princeton University Press.*

Mysak, L. A. [2001] "Patterns of Arctic Circulation", *Science*, **293**(5533), 1269-1270.

Nese, J. M. [1989] "Quantifying local predictability in phase space", *Physica D: Nonlinear Phenomena*, **35**(1-2), 237-250.

Ottino, J. M. [1989] "The Kinematics of Mixing: Stretching, Chaos, and Transport", *Cambridge University Press.*

d'Ovidio, F., Fernández, V., Hernández-García, E. & López, C. [2004] "Mixing structures in the Mediterranean Sea from finite-size Lyapunov exponents", *Geophysical Research Letters*, **31**(17), L17203.

Poincaré, H. [1914] "Science and method", *Thomas Nelson & Sons: London.*

Press, W. H., Teukolsky, S. A., Vetterling, W. T. & Flannery, B. P. [1992] "Numerical Recipes in C: The Art of Scientific Computing", *Cambridge University Press.*

Rempel, E. L., Chian, A. C.-L., Brandenburg, A., Muñoz, P. R. & Shadden, S. C. [2013] "Coherent structures and the saturation of a nonlinear dynamo", *Journal of Fluid Mechanics*, **729**, 309-329.

Rogerson, A. M., Miller, P. D., Pratt, L. J. & Jones, C. K. R. T. [1999] "Lagrangian Motion and Fluid Exchange in a Barotropic Meandering Jet", *Journal of Physical Oceanography*, **29**(10), 2635-2655.

Sakov, P., Counillon, F., Bertino, L., Lisæter, K. A., Oke, P. R. & Korablev, A. [2012] "TOPAZ4: an ocean-sea ice data assimilation system for the North Atlantic and Arctic", *Ocean Science*, **8**(4), 633-656.

Samelson, R. M. & Wiggins, S. [2006] "Lagrangian Transport in Geophysical Jets and Waves", *Springer.*

Shadden, S. C., Lekien, F. & Marsden, J. E. [2005] "Definition and properties of Lagrangian coherent structures from finite-time Lyapunov exponents in two-dimensional aperiodic flows", *Physica D: Nonlinear Phenomena*, **212**(3-4), 271-304.

Smale, S. [1980] "The Mathematics of Time: Essays on Dynamical Systems, Economic Processes and Related Topics", *Springer-Verlag.*

Stoffer, D. [1988a] "Transversal homoclinic points and hyperbolic sets for non-autonomous maps I", *Zeitschrift für angewandte Mathematik und Physik (ZAMP)*, **39**(4), 518-549.

Stoffer, D. [1988b] "Transversal homoclinic points and hyperbolic sets for non-autonomous maps II", *Zeitschrift für angewandte Mathematik und Physik (ZAMP)*, **39**(6), 783-812.

Sturman, R., Ottino, J. M. & Wiggins, S. [2006] "The Mathematical Foundations of Mixing: The Linked Twist Map as a Paradigm in Applications: Micro to Macro, Fluids to Solids", *Cambridge University Press.*

Tomczak, M. & Godfrey, J. S. [1994] "Regional oceanography: an introduction", Chapter 7, *Permagon, Tarrytown, N.Y.*, **422**.

Wiggins, S. [1992] "Chaotic Transport in Dynamical Systems", *Springer*.

Wiggins, S. [1999] "Chaos in the dynamics generated by sequences of maps, with applications to chaotic advection in flows with aperiodic time dependence", *Zeitschrift für angewandte Mathematik und Physik (ZAMP)*, **50**(4), 585-616.

Wiggins, S. [2003] "Introduction to Applied Nonlinear Dynamical Systems and Chaos", *Springer*.

Wiggins, S. [2005] "The dynamical systems approach to Lagrangian transport in oceanic flows", *Annual Review of Fluid Mechanics*, **37**(1), 295-328.

Wiggins, S. & Mancho, A. M. [2014] "Barriers to transport in aperiodically time-dependent two-dimensional velocity fields: Nekhoroshev's theorem and "Nearly Invariant" tori", *Nonlinear Processes in Geophysics*, **21**(1), 165-185.

Wood, K. R., Overland, J. E., Salo, S. A., Bond, N. A., Williams, W. J. & Dong, X. [2013] "Is there a "new normal" climate in the Beaufort Sea?", *Polar Research*, **32**(1), 19552.

WWF-World Wildlife Fund [2014] "Modeling Oil Spills in the Beaufort Sea", *World Wild Life Foundation Summary Report, http://awsassets.wwf.ca/downloads/wwf_beaufort_sea_oil_spill_modelling_summary_report.pdf*.

Xie, J., Bertino, L., Counillon, F., Lisæter, K. A. & Sakov, P. [2017] "Quality assessment of the TOPAZ4 reanalysis in the Arctic over the period 1991-2013", *Ocean Science*, **13**(1), 123-144.